Surface-Wave Tomography of Western Canada Using a Two-station Approach

by

Taras Andrew Zaporozan

A Thesis submitted to the Faculty of Graduate Studies of

The University of Manitoba

in partial fulfilment of the requirements of the degree of

MASTER OF SCIENCE

Department of Geological Sciences

University of Manitoba

Winnipeg

Abstract

Seismic data from 106 station pair-paths, from the CNSN (Canadian National Seismic Network) and POLARIS (Portable Observatories for Lithospheric Analysis and Research Investigating Seismicity) seismic networks, were used to measure surface waves from earthquake events. Fundamental-mode Rayleigh-wave dispersion curves were generated and inverted to obtain dispersion maps and S-velocity cross-sections.

Results show a clear distinction between the Cordilleran and cratonic lithospheres. The Cordilleran lithopshere shows a low-velocity perturbation with values ranging from -2% to -5%, while the cratonic lithosphere shows a high-velocity perturbation with values ranging from 3% to 9%. The large range in perturbation between the Cordilleran and cratonic lithospheres resolves the Cordilleran/craton boundary, showing that the boundary is present down to 200 km in depth and dips under the cratonic lithosphere. A high-velocity anomaly within the already high velocity cratonic lithosphere is present under Great Slave Lake and is interpreted as preserved Precambrian slab material. Many small high-velocity perturbations, reaching about 4%, are present at depths of 300+ km throughout the survey, and interpreted as being remnants of the Kula or Farallon plates.

Acknowledgements

I would like to start by stating that I owe my most sincere thanks to my advisor Dr. Andrew Frederiksen for providing me the opportunity to further my knowledge in Seismology, while having patience with me over this long journey. I am grateful for Dr. Ian Ferguson's guidance and withstanding the barrage of questions from me through my entire time in the Geological Sciences Department. I would also like to thank Dr. Pascal Audet for agreeing to be my external examiner.

I would like the thank Alexey Bryksin for creating the automation programs and for troubleshooting. To the many, many Geophysics and Geology students with whom I've befriended over the years, thanks.

Funding for this project was provided by NSERC, the Geological Survey of Canada, and DeBeers Canada.

Finally, I would like to thank my family and friends for supporting me throughout this prolonged process.

Contents

List of Tables

List of Figures

Chapter 1

Introduction

1.1 Overview

Precambrian shield and recent orogenic lithosphere exhibit major differences in seismic velocity, electrical resistivity, and geology (to name a few aspects), but the detailed structure of such transitions is not well understood. In North America, the Precambrian shield and platform of the continental interior share a western boundary with a recently active orogenic system. The Mesozoic Cordilleran orogeny of western North America is interpreted to have been formed along the active western margin of Pangea (Johnston and Gutierrez-Alonso, 2010). At this time subsequent blocks were added westward with rocks ranging in age from the Paleozoic to the Mesozoic (Frederiksen et al., 1998). The Cordillera displays folding and thrusting. The Cordillera is bounded by the North American craton to the east and the Pacific active margin of the North American Plate to the west.

Many studies have shown that under young orogens the lithosphere shows low velocity while the thick roots under cratons show high velocities (see e.g. a compilation of Lithoprobe studies given in Clowes et al., 2005; Van der Lee and Frederiksen, 2005; Schaeffer and Lebedev, 2014). The Cordillera/craton transition shows a strong seis-

mic contrast between the young orogen, much of which is still tectonically active, and the stable shield and platform. To gain a better understanding of this structure and the transition between Cordillera and the shield in detail, surface waves are analysed in this thesis to produce a tomographic model of the lithosphere of western Canada. Surface waves are used due to their ability to measure absolute velocity as well as their good depth resolution in the upper mantle.

1.2 Objectives

The objectives of this thesis are to build on the results of previous studies imaging North America, using various methods, and to investigate the Cordillera/craton boundary. This will be done via surface wave tomography using the two-station approach as explained by Meier et al. (2004). A previous study completed by Darbyshire et al. (2007) focused primarily on the area of eastern Canada through western Ontario. Work from the Lake of the Woods region west to Alberta was done by Alexsey Bryksin (Zaporozan et al., 2014). This thesis completes the westward imaging of Canada with overlap into central Canada and northern Canada (as seen in Figure 1.1).

1.3 Outline

To fulfill these objectives, a network of station-pair paths from the Canadian National Seismic Network (CNSN) and Portable Observatories for Lithospheric Analysis and Research Investigating Seismicity (POLARIS) seismic network archives was created to measure differences in surface-wave arrivals from distant earthquakes. These measurements will be used to create dispersion curves. Dispersion curves show the relationship between velocity and period, which can be inverted for depth. Since tele-

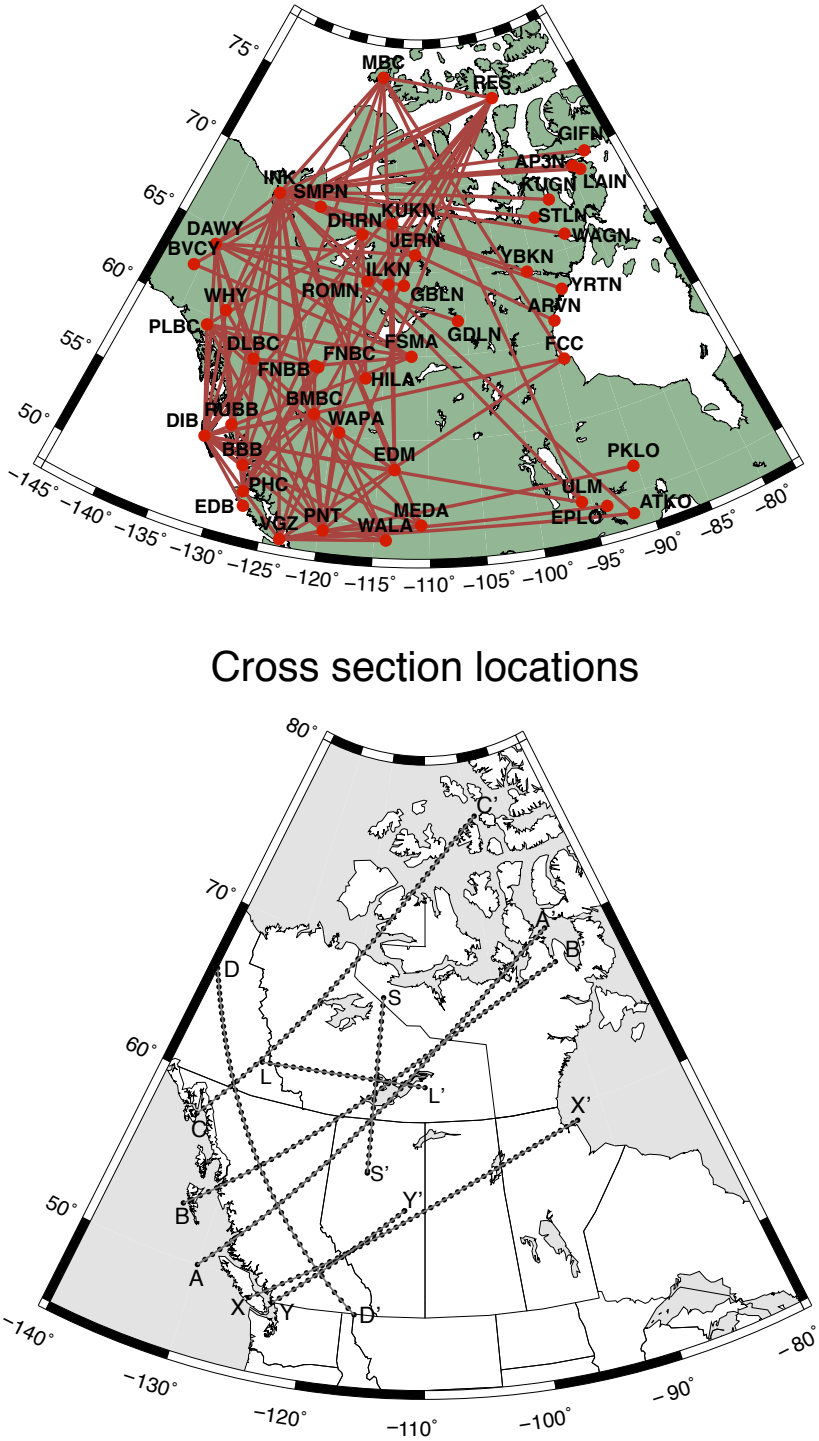

Cross section locations

Figure 1.1: (Top): station coverage area of western and northern Canada. (Bottom): Location of profiles used for creating pseudosections and cross-sections.

seismic tomography near the Cordillera/craton boundary has been previously completed to show the lateral velocity variations (Mercier et al., 2009), surface-wave tomography will compliment those results with more precise depth imaging of the area. Comparing these results with previous models (regional or global) will help to provide a better understanding of the Cordillera/craton transition in the upper mantle.

Chapter 2

Geological background

Western Canada is made up of a number of younger terranes accreted onto a Precambrian craton. The geological architecture of the Cordilleran Orogen in Canada is the product of a variety of tectonic processes acting upon the margin of ancient North America (Gabrielse and Yorath, 1991). The assemblage of the craton occurred primarily in the Archean and Early Proterozoic with younger terranes ranging in age from Early Permian to late Mesozoic-Cenozoic.

2.1 Cratonic terranes

A detailed tectonic model of the general assembly of Laurentia is described by Whitmeyer and Karlstrom (2007) in which they describe the Proterozoic growth of North America. Figure 2.1 shows a map of the boundaries and ages of major tectonic blocks for this model. The Slave, Rae, and Hearne are Archean crustal blocks older than 2.5 Ga (shown in gray in northern North America). The Slave province is a late Archean granite-greenstone terrane and was a foreland for the Thelon orogen to the east and the Wopmay orogen to the west (Hoffman, 1988). At ca. 1.96-1.92 Ga the initiation of the Slave-Rae collisional zone occurred forming the Thelon arc,

resulting from a dextral-oblique collision between Slave and Rae provinces followed by indentation of the Rae by the Slave foreland province (Hoffman, 1988).

The formation and assembly of the Wopmay orogen (coloured in burnt orange in Figure 2.1) occurred from ca. 1.92-1.86 Ga. The orogen lies to the west and southwest of the Slave-Rae collisional zone and evolved on the active western margin of the Slave province. It includes a collage of domains that assembled in Paleoproterozoic time (Clowes et al., 2005) and formed from the accretion of the Hottah terrane, the Great Bear magmatic arc, the Fort Simpson terrane, and the Nahanni domain. Cessation of activity of the Great Bear arc took place at $\sim$ 1.84 Ga (Clowes et al., 2005, Cook et al., 1999).

The next major event of note for the study area is the formation of rift boundaries at the western margin of Laurentia, which are outlined with a red line in Figure 2.1. From its inception, due to rifting, during the Middle Proterozoic to present (Gabrielse and Yorath, 1991; Nelson and Colpron, 2007; Cook et al., 2004) the continental margin moved oceanward, due to offshore sediment progradation, and as a result of convergence and transform-related processes involving the accretion of island arc and oceanic assemblages (Gabrielse and Yorath, 1991). The miogeocline of ancestral North America resided in a passive margin for much of this time.

At 0.78 Ga (estimated), the deposition of the Windermere Supergroup occurred (Whitmeyer and Karlstrom, 2007). The Windermere Supergroup consists of neo-Proteozoic rocks in western North America (from the Mackenzie Mountains south into the United States). They are a stratigraphic succession that contains basal sedimentary and volcanic rocks interpreted to have formed during active faulting (Ross, 1991). During this time sedimentation of coarse clastics of the Windermere Supergroup occurred in an intra-cratonic rift margin (as interpreted by Nelson and Colpron (2007)) that evolved into a passive margin (Ross, 1991).

The formation of the western margin (paleo-Pacific) is believed to have involved

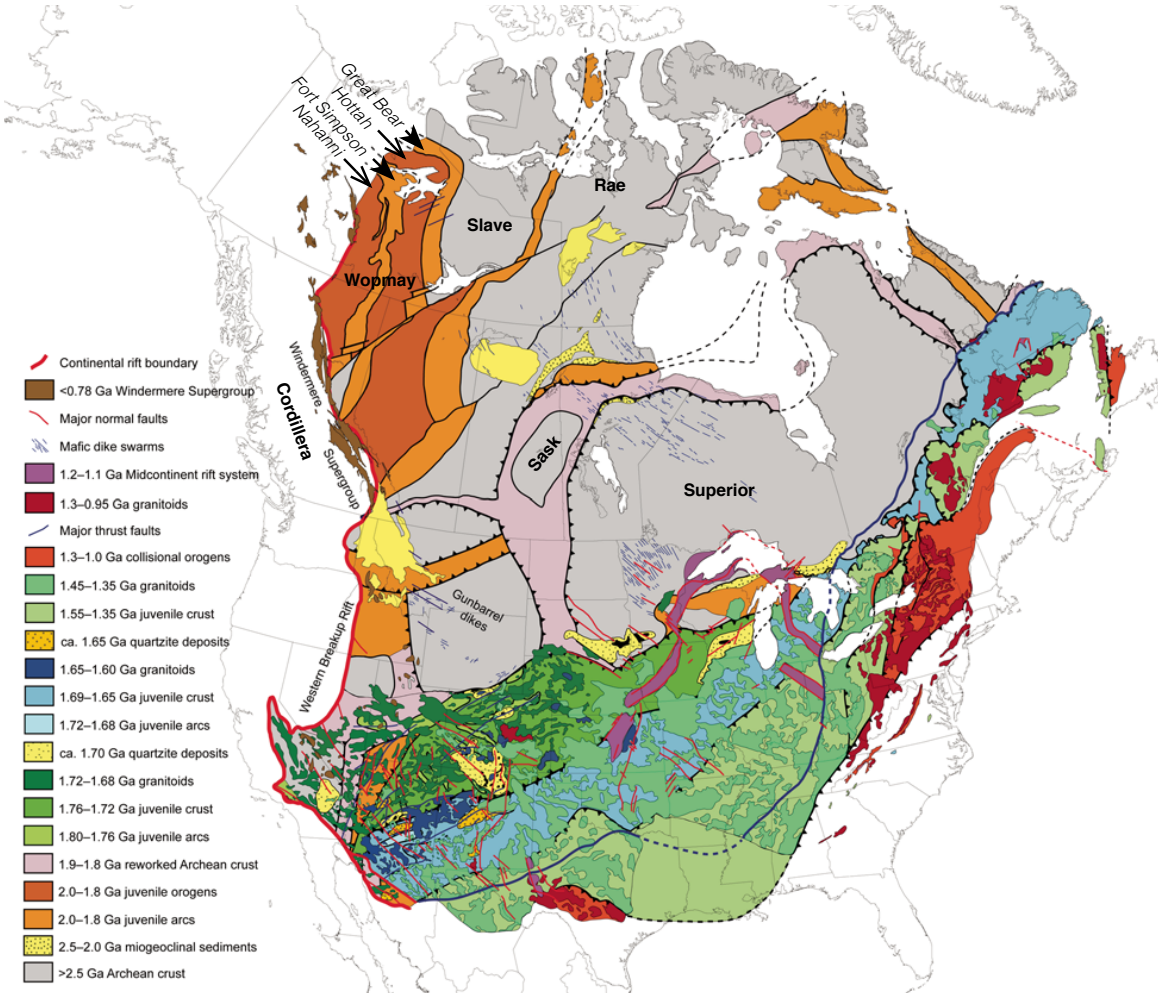

Figure 2.1: Model of the growth of North America after the deposition of the Windermere Supergroup (in brown) (modified from Whitmeyer and Karlstrom, 2007). The bold labels correspond to noted tectonic provinces, while italicized labels are selected geologic terranes of the Wopmay tectonic province. The red line shows rift boundaries along the western margin of Laurentia.

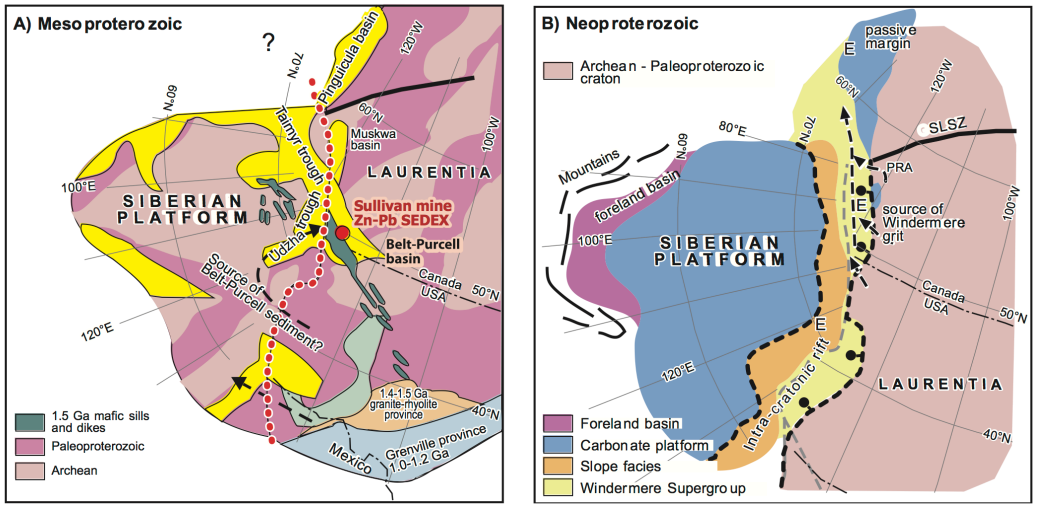

Figure 2.2: (A) Possible Mesoproterozoic reconstruction of Laurentia with Siberia. (B) Neoproterozoic breakup of Rodinia (modified from Colpron et al., 2007).

at least two separate episodes of rifting (Colpron et al., 2002; Nelson and Colpron, 2007). Figure 2.2 (A) shows a reconstruction of Laurentia and Siberia. Figure 2.2 (B), (according to Sears and Price (2000, 2003)) shows the breakup of Rodinia and is believed to have occurred from the Devonian through the Tertiary (Cook et al., 2004). Colpron et al. (2002) determined that the late Neoproterozoic rifting of the southern Cordillera occurred at the same time as passive margin sedimentation in the northern Cordillera. Other authors have constrained rifting and deposition to between ca. 755 Ma (Wingate and Giddings, 2000) and ca. 700 Ma (Powell et al. 1993) with Powell et al. (1993) stating that the two continental masses started to diverge at 725 Ma.

2.2 Cordilleran terranes

Figure 2.3 (A) shows a geologic map of the Cordilleran origin, with terranes assigned to platform or shelf according to Johnston and Gutierrez-Alonso (2010). Much of these terranes overlain basement rocks of Paleoproterozoic age in the northern

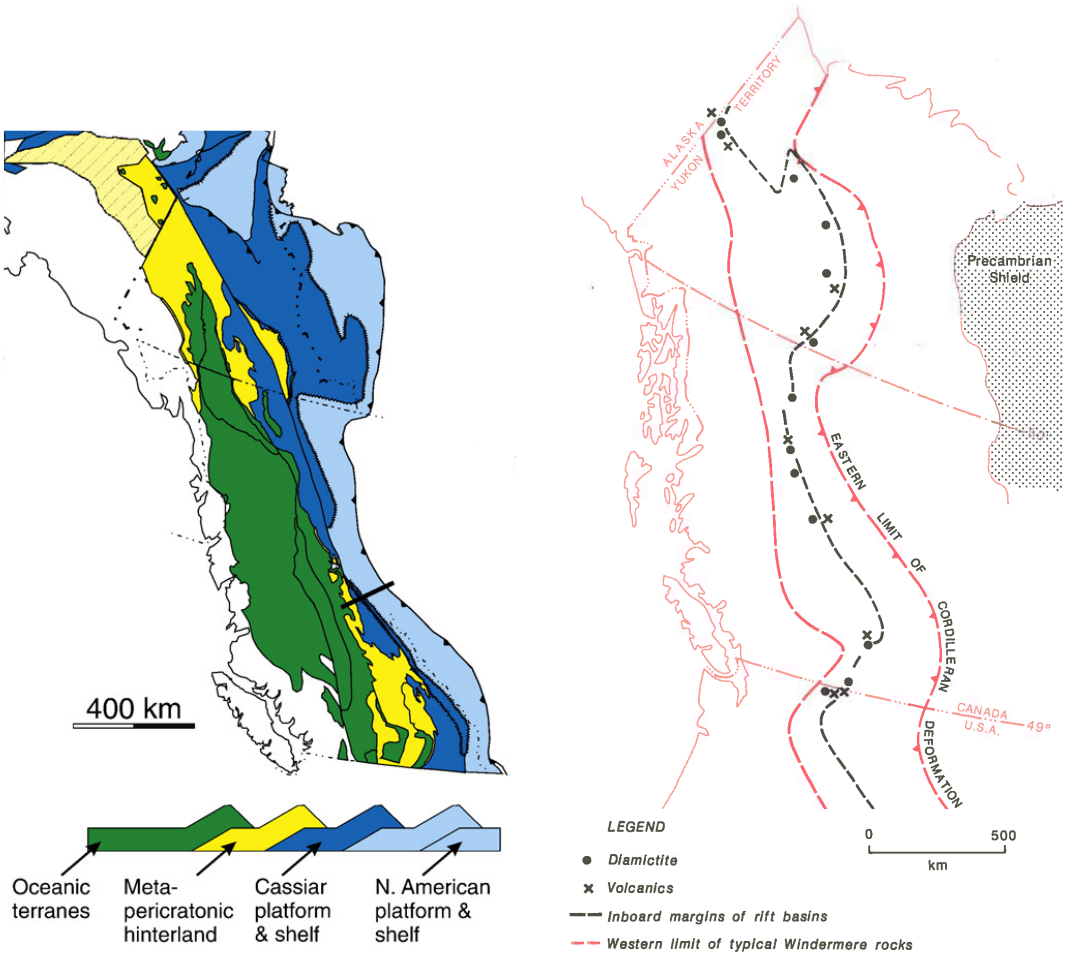

Figure 2.3: (A) Geological map of the Cordillera of western Canada (modified from Johnston and Gutierrez-Alonso, 2010) (B) illustration of the possible extent of the Windermere Supergroup (modified from Gabrielse and Yorath, 1991).

Cordillera (Cook et al., 2012).

Oceanic and island arc assemblages of the central and western Cordillera are comprised of a variety of crustal fragments which form a collage of accreted terranes (Gabrielse and Yorath, 1991). These accreted terranes can be grouped into the Intermontane and Insular superterranes (Figure 2.4) which are made up of smaller terranes that amalgamated, and became incorporated into the continent during the Mesozoic (Gabrielse and Yorath, 1991). Between the accreted superterranes and ancestral North America, the Omineca Belt is comprised of several terranes, some of

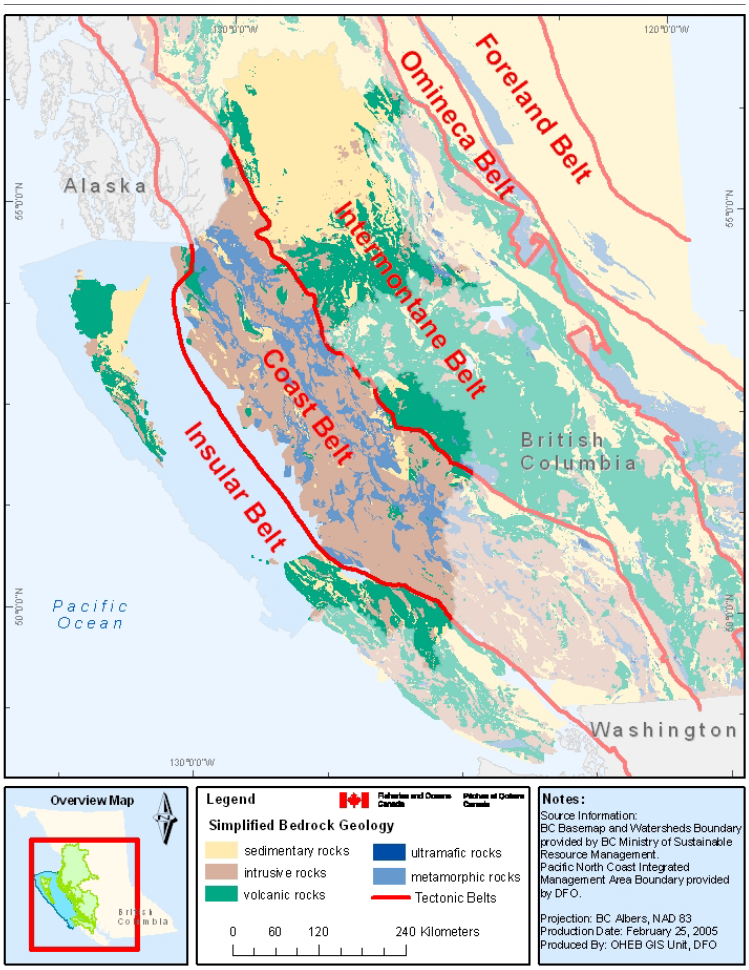

Figure 2.4: Illustration showing the location of the Intermontane and Insular superterranes overlain on a simplified bedrock geology map (Conway and Johannessan, 2007).

which have close continental affinities and others which have been transported long distance and thrust over the continental margin (Gabrielse and Yorath, 1991). The Omineca Belt was a major regional tectonic welt, a raised part of the Earth's crust with a distinct linear development, which underwent intense deformation, regional metamorphism, granitic magmatism, uplift, and erosion (Monger et al., 1982). Monger et al. (1982) regard these processes as a product of Triassic-Jurassic tectonic amalgamation.

In contrast to the Omineca Belt, the Intermontane terranes and the Insular terranes did not show an early relationship with the western margin of North America, even though they were formed between the Precambrian and Triassic (Nelson and Colpron, 2007). During the Middle Jurassic, the Intermontane superterrane began accreting to the North American plate and resulted in the passive-margin sequences being folded (Clowes et al., 2005). Figure 2.5 shows the Intermontane superterrane collage of accreted terranes of the Cordillera and displaced continental margin rocks to the west of the Tintina Fault. The Coast Belt is a rugged high-relief region bound by Late Cretaceous-Tertiary strike-slip faults or a marked change in relief and lithology in the east and between Vancouver and Queen Charlotte islands and the mainland in the west. The plutonic, relatively mafic, rocks underlie three-quarters of the Coast Belt with variably metamorphosed sedimentary and volcanic rocks underlying the remainder (Monger, 1989).

2.3 Faults

The Denali, Queen Charlotte, and Tintina faults are three major faults located in western Canada (Figure 2.5). The Queen Charlotte fault stretches from southern British Columbia to southern Alaska. The Denali fault branches off the Queen Charlotte fault and extends northward into western Alaska. The Tintina fault stretches from western Alaska to southern British Columbia, over 2000 km. In the south it becomes part of the Rocky Mountain trench (Ledo et al., 2002).

The Tintina fault is a major-crustal strike-slip fault with total offsets estimated to range from greater than 900 km (Gabrielse, 1985), to 450 km (Tempelman-Kluit, 1979; Dover, 1994). Roddick (1967) claims that older metamorphic rocks are best matched if a 420 km dextral displacement is assumed. This right-lateral motion is confirmed by Dover (1994) for all strike-slip motion in east-central Alaska. Saltus

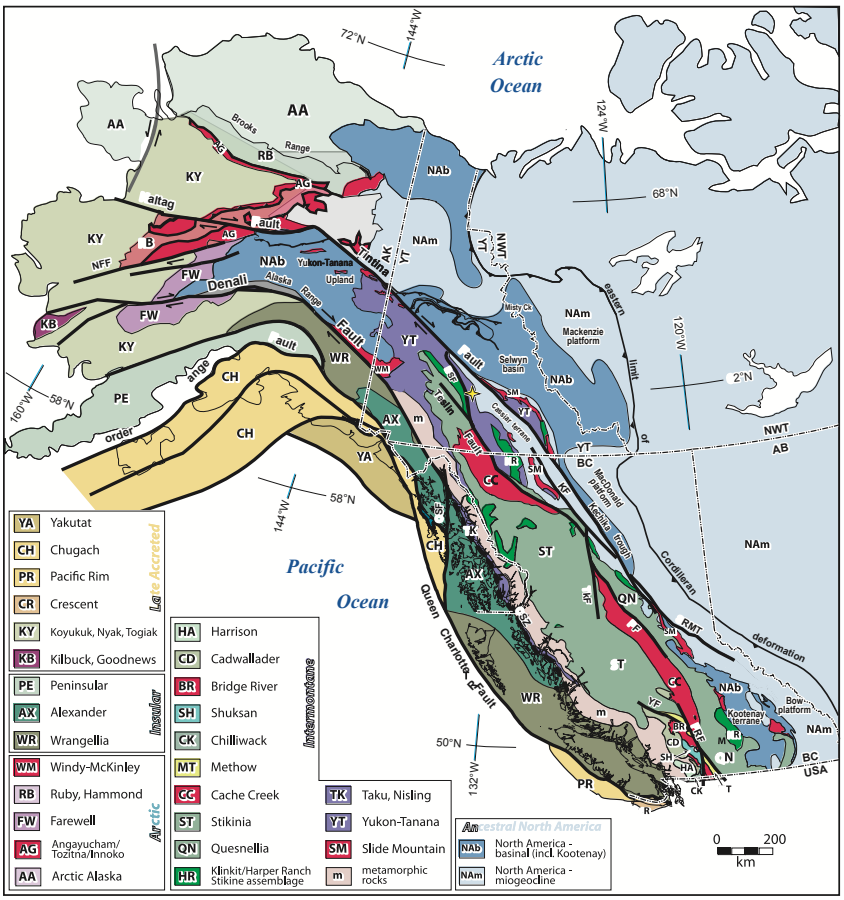

Figure 2.5: Terranes of the Canadian and Alaskan Cordillera (Nelson and Colpron, 2007).

(2007) subjected the Tintina fault system to a 490 km shift resulting in some interesting geological alignments such as, for example, the matching features of the Inconnu thrust fault and the coincidence of eclogite and blueschist occurrences trending from the town of Eagle to near Fairbanks. The start of movement is believed to date from the middle Cretaceous (Gabrielse, 1985) or the Late Cretaceous (Roddick, 1967; Tempelman-Kluit, 1979) to the Eocene or Oligocene (Gabrielse, 1985; Gabrielse et al., 2006) or Early Tertiary (Tempelman-Kluit, 1979). Dating of the Tintina fault system is controversial due to different ages determined for different parts of the fault. Cenozoic deformation of the southern Cordillera complicates attempts to trace the

fault south (Gabrielse, 1985) and the fault being parallel to ancient facies boundaries and structural trends (Roddick, 1967). Across the Southern Rocky Mountain Trench changes in traverse, thickness, and facies are not subjected to right-lateral strike-slip motion until near the north end (54°15'N) of the southern trench (McMechan, 2000).

Chapter 3

Background geophysics

Many geophysical methods have been used to image the Cordilleran and craton crust and mantle and its lithosphere and asthenosphere. Controlled source seismic reflection and refraction surveys have imaged the crust and uppermost mantle, with teleseismic surveys reaching greater depths. Using these data, the crust and mantle are imaged on regional, continental, and global scales (as discussed in section 3.1). Magnetotelluric (section 3.2) and thermal (section 3.3) surveys have provided constraints on a similar range of depths which allows for multidisciplinary analysis of the lithosphere beneath the survey area.

3.1 Seismic models

3.1.1 Global and continental models

Many continental and global models show a distinct velocity perturbation difference between the Cordillera in the west and the craton in the east. From a continental perspective, Van der Lee and Frederiksen (2005) and Bedle and van der Lee (2009) produced models NA04 and NA07 focusing on North America (Figures 3.1 and 3.2 respectively). These models were obtained using one-station analysis and partitioned

waveform inversion as described by Nolet (1990). Both models image velocity perturbations and show a velocity contrast between the Cordillera and the platform and shield.

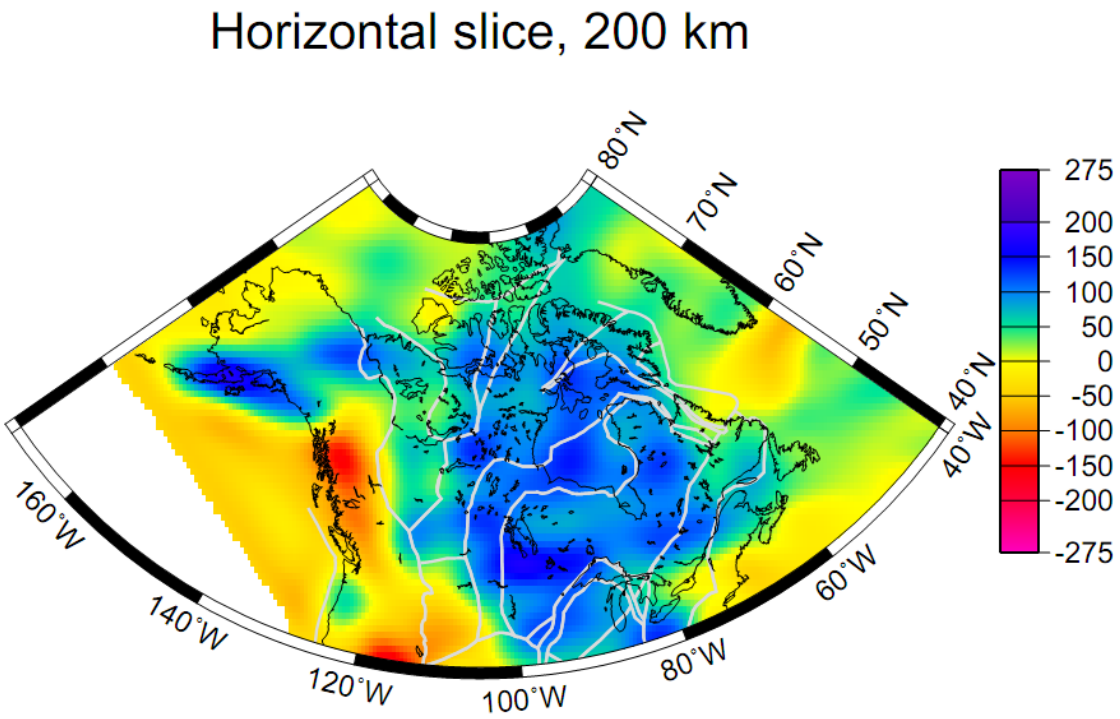

Figure 3.1: Horizontal slice of NA04 model at a depth of 200 km (van der Lee and Frederiksen, 2005). White lines indicate major geological provinces. Velocity is in m/s difference of S velocity from the MC 35 base model.

The lithospheric boundary within the NA04 model generally follows the geological boundary of the Cordillera except in three areas. Just south of 50°N, a higher velocity feature crosses into the Cordillera with velocity differences up to 100 m/s. Further north, 59°N, the 0 m/s velocity difference contour crosses into the craton where it follows the boundary north and turns and caps off the northern Cordillera at about 65°N. Velocity differences in the north range from 50-100 m/s. Within the Cordillera a large low velocity area beneath the Cordillera (shown in red) has velocity differences down to -200 m/s.

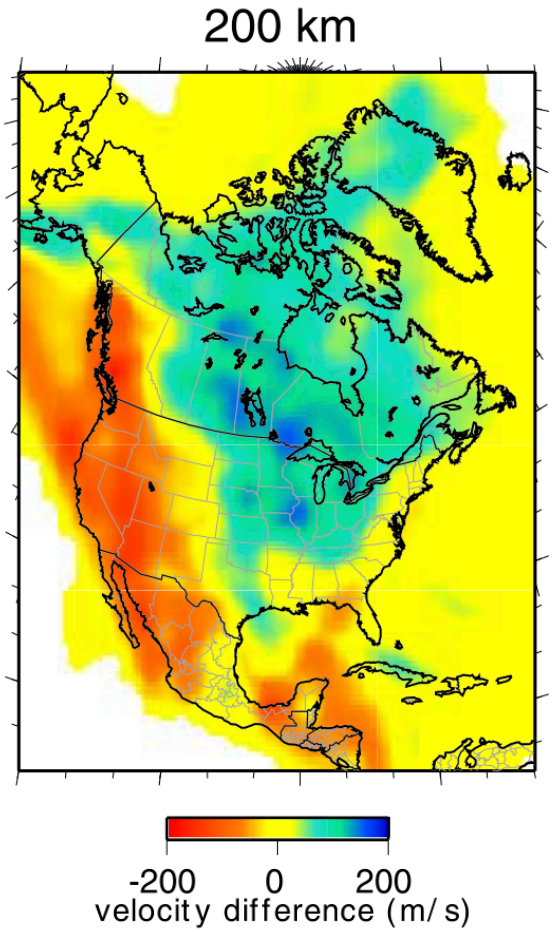

Figure 3.2: Horizontal slice of the NA07 model at a depth of 200 km (Bedle and van der Lee, 2009).

The NA07 model shows less contrast in velocity differences. The entire western half of the Cordillera shows differences ranging from -100 to -200 m/s. To the north and east of this slow area is a thick gradual increase in velocity difference showing a broader boundary than seen in NA04.

Comparing the NA04 and NA07 models, mantle velocities are similar at a depth of 200 km with a value around -200 m/s in the Cordillera. Looking more closely it is possible to see differences in the area of the -200 m/s perturbation. In the Bedle and van der Lee model the Canadian Cordillera is almost entirely contoured

as approximately -200 m/s, but for the NA04 model, van der Lee and Frederiksen (2005) show a weakening in velocity perturbation to approximately -100 m/s in the south part of the Canadian Cordillera. The east/west smearing that is seen in both NA04 and NA07 models is a result of dominant east-west seismic paths due to the concentration of seismicity along the west coast, and can be reduced by means of the two-station approach.

Figure 3.3 shows multiple slices of the Bedle and van der Lee (2009) NA07 model. At increasing depth the negative velocity perturbation below the Cordillera decreases from -500 m/s at 90 km depth to 0 m/s variation at 250 km depth, possibly representing the base of the lithosphere. The shield velocity perturbation has a positive velocity perturbation of >150 m/s over a large area and increases to 300 m/s moving further into the shield at a depth of 90 km.

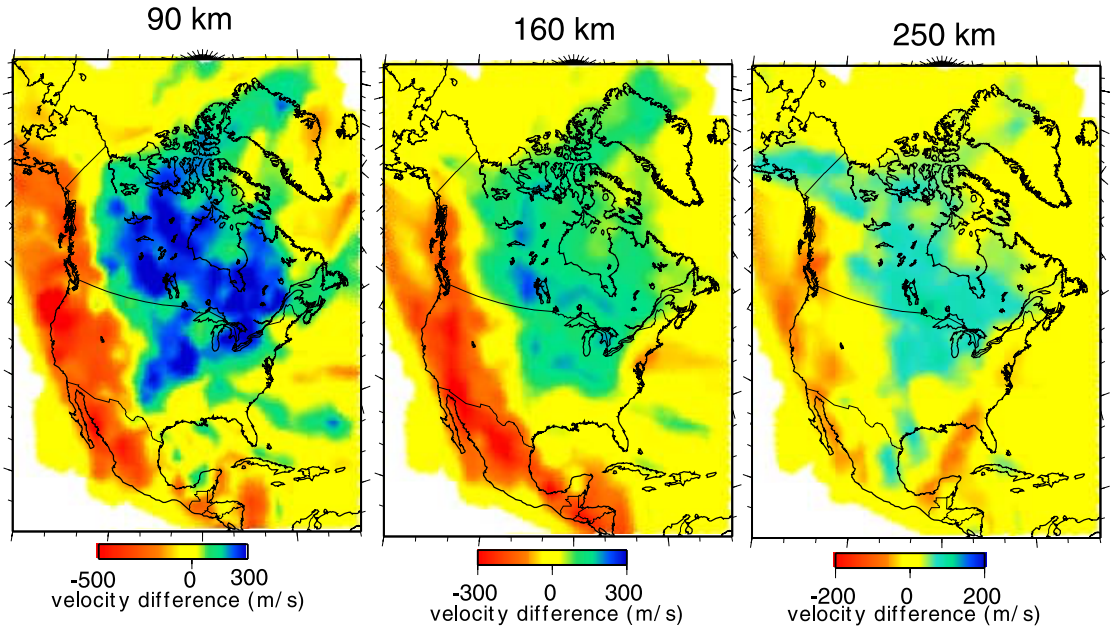

Figure 3.3: $\overline{\text{NA07}}$ model of North American S velocity variations. This model was calculated from the average of 20 tomographic models using various regularization, weighting, flattening, and damping parameters including a random set of 4000 waveforms drawn from a larger database (Bedle and van der Lee, 2009).

All three NA models show a potential boundary between a Cordillera and cratonic lithosphere (Figures 3.1 and 3.2) at 200 km depth. Figure 3.3 shows a varying boundary at different depths with the 0 velocity difference contact being almost entirely west of the geologically determined Cordilleran boundary at 90 km. At a depth of 160 km this 0 velocity difference expands eastward creating a more gradual contact. At 250 km the 0 velocity difference appears truncated in the north and expands further eastward.

Figure 3.4 shows a model (SL2013NA) for North America (Schaeffer and Lebedev, 2014) from global and USArray data which shows the positive velocity craton separated from the Cordillera by a boundary corresponding to the Rocky Mountain Trench in Canada. Figure 3.5 shows a side-by-side comparison between models. SL2013NA shows a greater extent of the slower perturbations throughout the Cordillera. Both slow and fast perturbations follow the Rocky Mountain Trench much more closely than in NA04 and NA07 models with the 0% variation (white in the plot) remaining entirely to the west or south of the Rocky Mountain Trench in Canada. The slow velocity perturbation within the Cordillera, as seen in NA04 and NA07 models as red regions, is more resolved in SL2013NA with perturbations of -6% striking NNE/SSW and SSE/NNW.

With an emphasis on imaging plate fragments at greater depths, Sigloch et al. (2008) studied finite-frequency body-wave tomography on a large scale to image a connection between the remnants of the Farallon plate (Juan de Fuca plate and shallower pieces) with pieces located along the east coast of North America.

3.1.2 Regional teleseismic models

A teleseismic tomographic survey of the Cordillera was done by Mercier et al. (2009) analyzing the mantle under the Cordillera using the travel times of P and S-

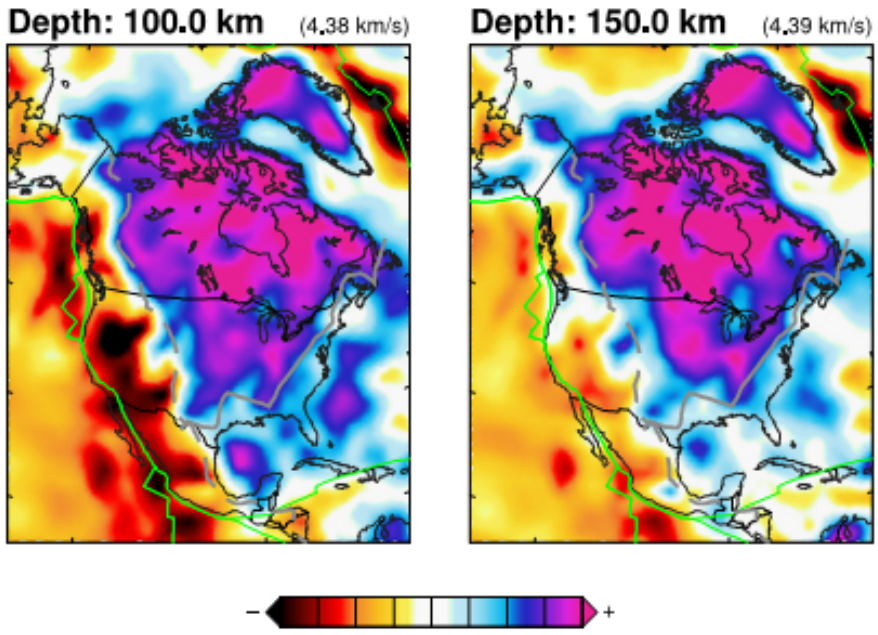

Figure 3.4: SL2013NA model of North America imaging continental velocity variations (Schaeffer and Lebedev, 2014). The dashed line in the figure indicates the Rocky Mountain Trench.

waves. The use of teleseismic body waves means that the incident ray paths are near vertical, which provides very good lateral resolution but poor vertical resolution. This poor resolution results in vertical smearing and insensitivity to very-long wavelength structures. The images in Figure 3.6 show horizontal slices at 100 and 200 km depth. At depths of 100 km and 200 km there is a well-defined transition between the eastern portion of the study area, which contains a faster anomaly, and the western portion, which contains a slower anomaly. The sharp transition in the south is roughly along the Cordilleran deformation front (in some areas following the Tintina fault), while in the north its position is less clear but also appears to coincide with the deformation front for both depth slices of the model, similarly to what is seen in $\overline{\text{NA07}}$ (Figure 3.3). The horizontal resolution of Mercier et al. (2009) provides a sharper contrast of the Cordillera/craton boundary, helping to image this transition better than was

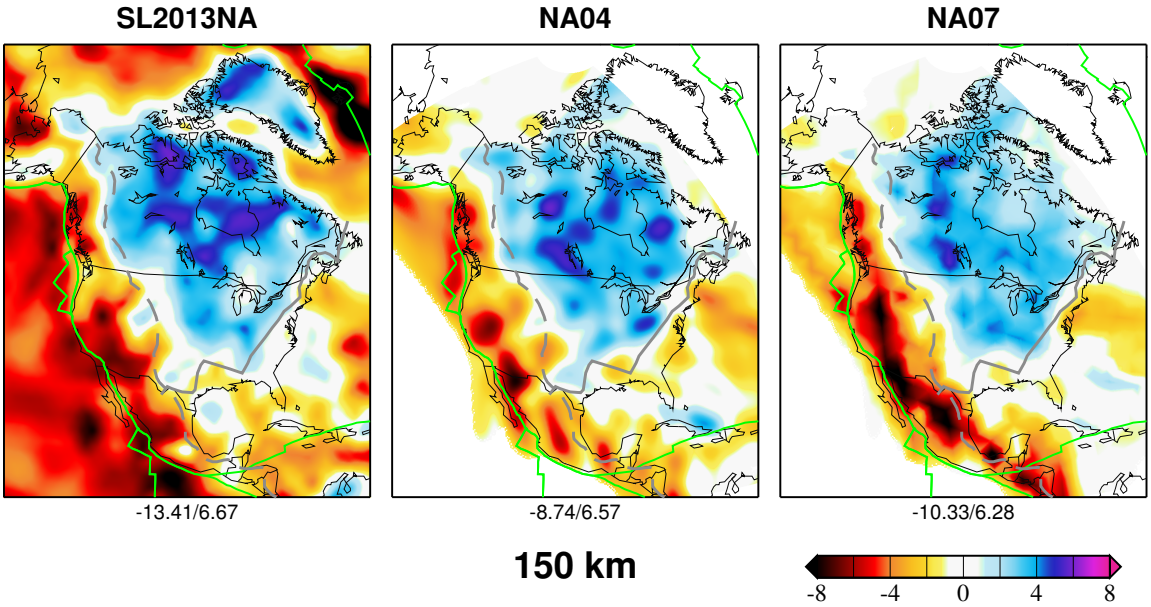

Figure 3.5: Model comparisons between SL2013NA (Schaeffer and Lebedev, 2014), NA04 (Van der Lee and Frederiksen, 2005), and NA07 (Bedle and van der Lee, 2009) models. Perturbations are plotted with respect to percent difference from the mean average velocity of NA07.

achieved using surface-wave tomography.

A more focused survey was done across the Southern Rocky Mountain Trench and the eastern limit of the Cordilleran deformation (Bao et al., 2014; Bao and Eaton, 2015) using surface waves. The survey area contains rocks of Archean, Paleoproterozoic, and Phanerozoic ages. Figure 3.7 shows two-dimensional dispersion curve maps (Bao and Eaton, 2015) showing a sharp contrast between slower velocities in the Cordillera (3.8 km/s at a period of 50s to 4.2 km/s at a period of 150 s) and faster velocities in the craton (4.0 km/s at a period of 50s to 4.3 km/s at a period of 150 s). With increasing period, this contrast decreases, showing a less defined velocity perturbation contrast at greater periods.

Inversion of these 2-D dispersion maps (Figure 3.8) by Bao and Eaton (2015) shows -4% to -6% Cordilleran velocity perturbations, compared to the AK135 global reference model, at depths of 55 km and 105 km. At these depths the cratonic

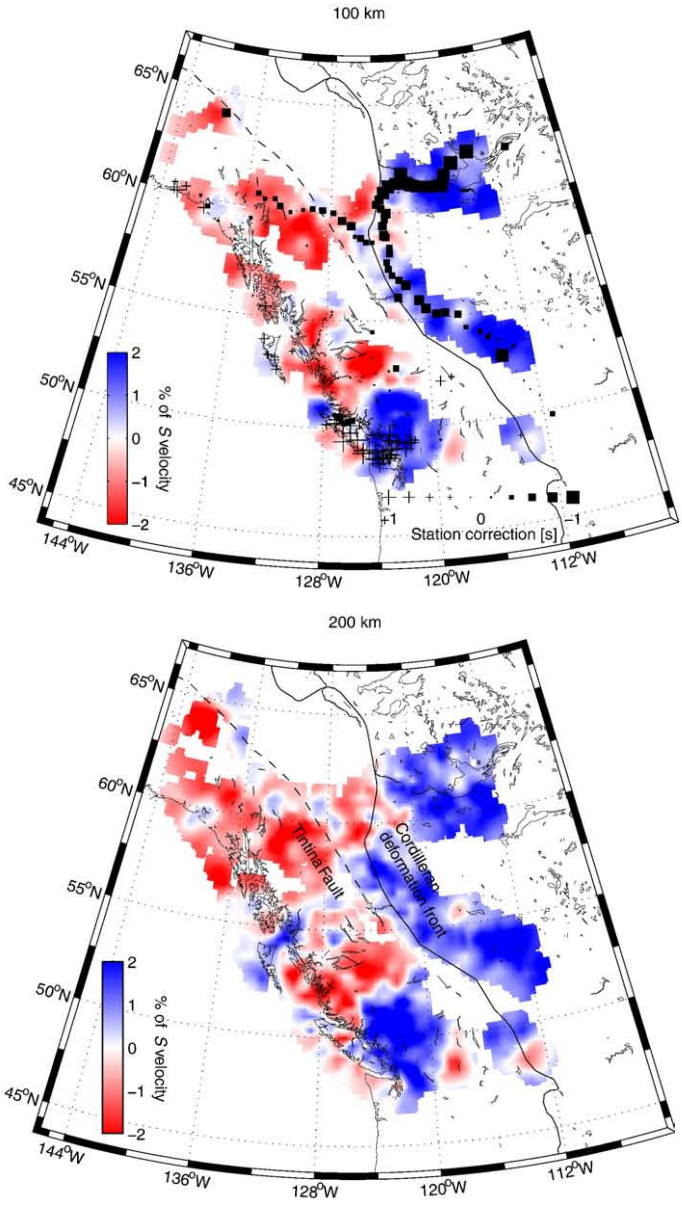

Figure 3.6: Horizontal slice of the S-wave model at 100 km (top) and 200 km (bottom) depths (Mercier et al., 2009).

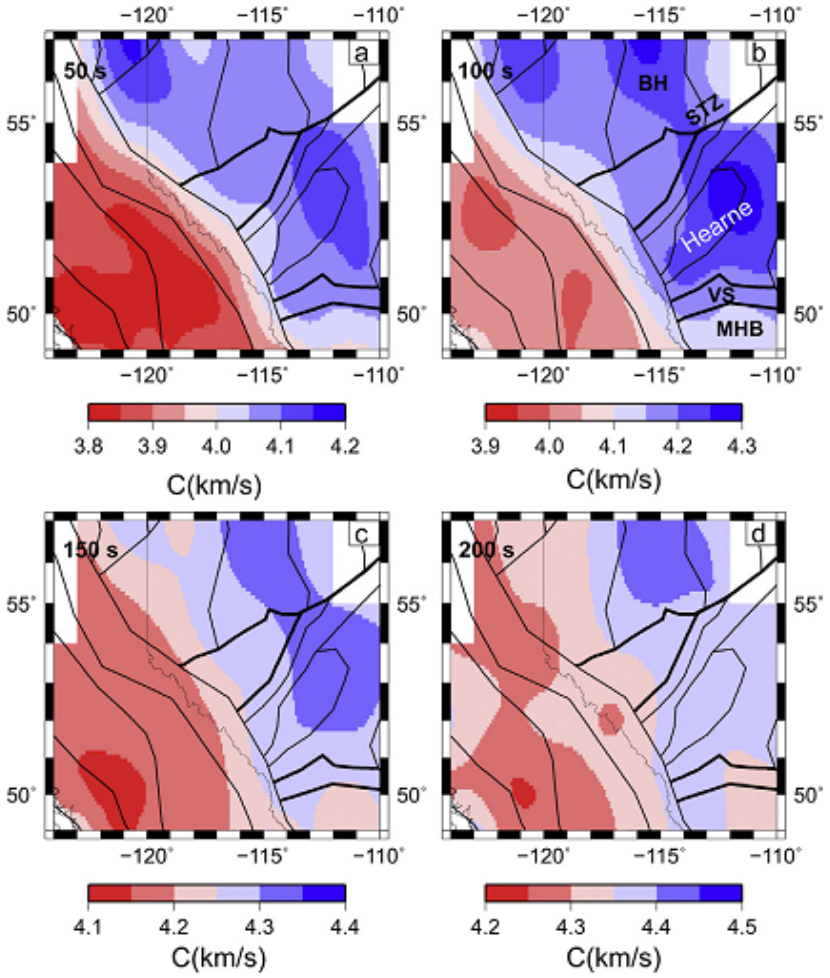

Figure 3.7: Two-dimensional phase-velocity maps (Bao and Eaton, 2015).

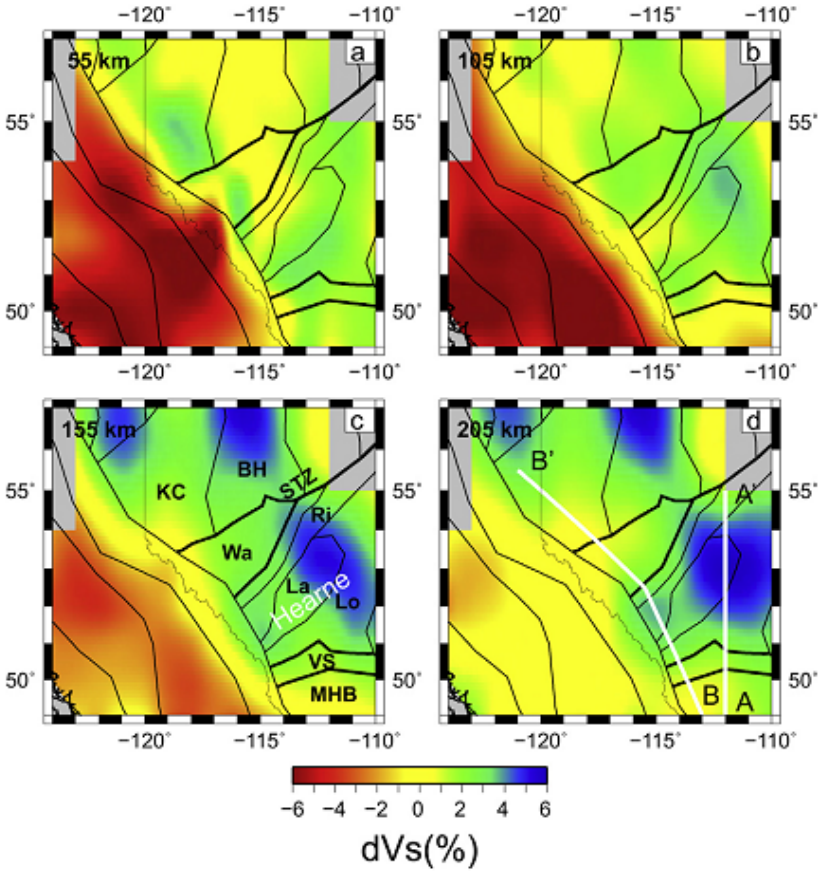

Figure 3.8: Relative shear velocity compared to the global reference model AK135 (Bao and Eaton, 2015).

velocity is greater than 0%, approaching 2%. At 155 and 205 km depth the Cordillera velocity perturbations trend towards a velocity difference of 0%. Craton velocity perturbations, however, are almost entirely 2% throughout the imaged area with areas of higher velocity perturbation (4 - 6%). The sharpest contrast between the Cordillera and craton appears at 105 km with perturbation velocities of -4% and 2%, respectively.

Figure 3.9 (Bao et al., 2014) shows a velocity perturbation map of the survey area at a depth of 105 km. This figure shows a sharp contrast between the Cordillera and craton perturbations. Cordilleran perturbations are less than -2% while craton

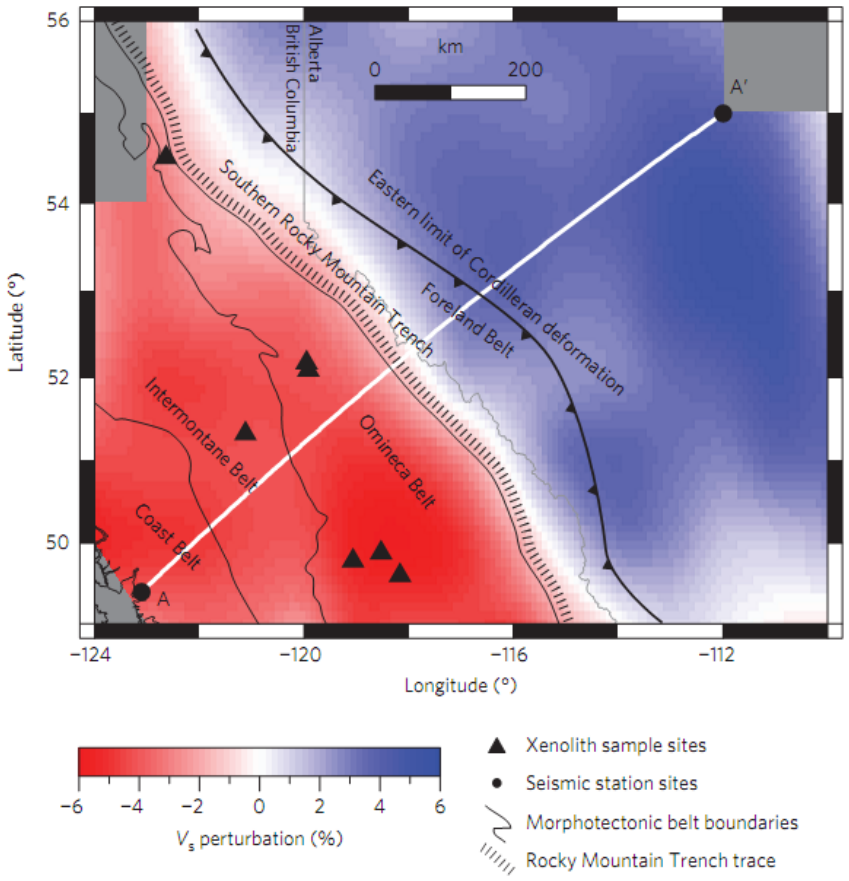

Figure 3.9: Vs velocity perturbation map of survey area at a depth of 105 km (Bao et al., 2014).

perturbations are greater than 2%. It is interesting to note how closely this contrasting Crodillera/craton line follows the southern Rocky Mountain Trench south of 55° latitude. Farther north the 0% perturbation line starts to follow the eastern limit of the Cordilleran deformation.

3.1.3 Seismic reflection and refraction

The LITHOPROBE program provided numerous sets of seismic reflection and refraction data (Burianyk and Kanasewich, (1997); Cook et al., (1999); Cook et al., (2004); Clowes et al., (2005); Hammer and Clowes, (2004); Hammer et al., (2010))

allowing for large scale study of western Canada. These studies found the Moho to be at around 35 km depth throughout the area. The interpreted lithospheric thickness is not uniform, with depths to the base in the west of the Cordillera ranging from 50 km (Clowes et al., 2005) to 100 km (Hammer et al., 2010) with increasing distance eastward. For the southern Canadian Cordillera, specifically the 1990 Southern Cordillera Refraction Experiment of LITHOPROBE's Southern Cordillera Transect, Burianyk and Kanasewich (1997) identify a low velocity zone (P wave velocity equaling 7.8 - 8.0 km/s) at a depth of about 50 km continuing to about 58 to 62 km from seismic refraction. The low velocity zone is interpreted as the asthenosphere with the base of the lithosphere being at 50 km, in agreement with results from Jones et al. (2005) in being much less than 100 km.

Hammer et al. (2010) summarize results from numerous refraction and reflection studies imaging the subduction of the Juan de Fuca lithospheric mantle under the Cordillera at the Cascadian subduction zone. Moho depths in the Cordilleran Orogen are calculated to be 35 km throughout with complex geology to the west due to the subduction zone. The base of the lithospheric mantle is interpreted as $\sim$ 50 km which coincides with estimates by Burianyk and Kanasewich (1997).

Deep reflection data from Lithoprobe's Slave-Northern Cordillera Lithospheric Evolution (SNORCLE) project in the Canadian Cordillera (Cook et al., 1999), along transect 1 (Figure 3.10 top), shows a mantle reflector dipping eastward beneath the Great Bear arc. Where this reflector flattens out into the lower crust, it merges with a west-dipping crustal reflection delineating a lithosperic-scale wedge formed as a result of Proterozoic plate convergence between the Slave craton and the Fort Simpson terrane (Cook et al., 1999).

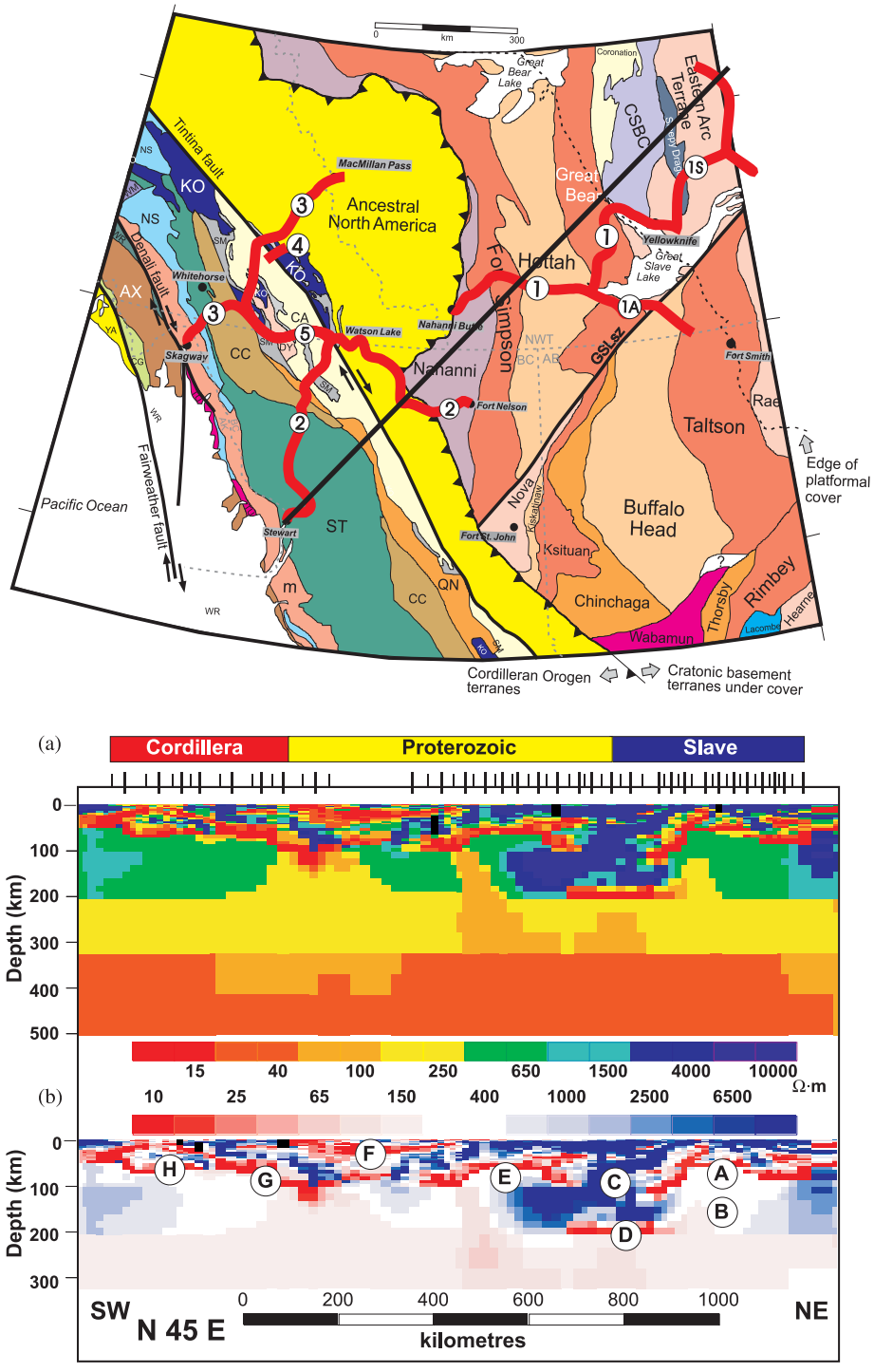

Figure 3.10: Top: Tectonic map of northwestern Canada showing the locations of SNORCLE transects and the profile of the regional magnetotelluric model. Bottom: Cross-section of a regional magnetotelluric model using a continuous colour scale (a) and a colour scale highlighting low-resistivity and high-resistivity features (b) created from SNORCLE transects 1, 1A, 1S, 2, 3, 4, and 5 in northwestern Canada (Jones et al., 2005).

3.2 Magnetotellurics

3.2.1 Northern Canada

Magnetotelluric (MT) data from the Lithoprobe SNORCLE transects 1, 1A, 1S, 2, 3, 4, and 5 were acquired over 14 surveys (from 1996 until 2000) using broadband and long-period MT instruments. A general objective of these studies was the imaging of the electrical resistivity structure of the crust and upper mantle (Jones et al., 2005). The cumulative result of the surveys identified, as interpreted by Jones et al. (2005), was the detection of eight significant features present in the crust and upper mantle (Figure 3.10 bottom) labeled A through H.

Results from Jones et al. (2005) show an upper mantle conductor beneath the centre of the Slave craton. Previous papers (Jones, et al., 2001; Jones et al., 2003) have identified this conductor, naming it the Central Slave Mantle Conductor (CSMC). The CSMC (Feature A) has a starting depth of approximately 80 - 100 km with a thickness of 20-30 km (Jones et al., 2003). Imaging of feature B, below, was hindered by the attenuating effects of the CSMC itself, but long-wavelength MT was able to poorly define the electrical asthenosphere at a depth of about 210 km (Jones et al., 2003).

Feature C is located in the southwestern Slave Province and has a highly resistive lithosphere that extends tens of kilometres to the southwest into the Wopmay orogen (Jones et al., 2005). Results from Spratt et al. (2009) show two, high resistivity, cratonic roots beneath the Slave province and the MacKenzie platform with depths reaching 200 km. The depth of these roots are consistent with Feature C for the base of the lithosphere. The separation of cratonic roots may be due to increased resolution, but possible evidence of this may be seen in Jones et al. (2005) centred on the Slave/Proterozoic boundary. Deep beneath Feature C is a highly conductive feature (D). The depth of this feature, interpreted as the asthenosphere, is suggested

to be 250 - 260 km ± 35 km (Jones et al., 2003).

High conductivity in the mantle at a depth of about 80 km is identified as Feature E and lies beneath the Wopmay orogen. Feature F lies beneath the transitional area between the Wopmay orogen and the Cordillera. This highly conductive layer is crustal and is more conductive than anywhere else along the profile (Jones et al., 2005). Differences between transects 2 and 3 show that northern Ancestral North America (transect 3) shows a conductive layer near surface (5 km) while transect 2 identifies the same conductive feature at a depth at 20 km (Jones et al., 2005). Feature G is identified as a northeast-dipping conducting layer of Cordillera origin starting mid-crust and dipping deep into the lithosphere. Feature H in the southwest of the profile is interpreted as a thin electrical lithosphere. Using previous results from Jones et al. (2001; 2003) along with their work, Jones et al. (2005) also conclude that the depth of the top of asthenosphere varies along the transect; a depth of around 190 km for the central Slave craton, 260 km for the southwest Slave Province, and $<<$ 100 km in the Alexander Terrane.

3.2.2 Southern Canada

Previous magnetotelluric studies have been completed crossing the Insular, Coastal, and Intermontane belts (Soyer and Unsworth, 2006) and far as the Omineca belt and into the Foreland (Rippe et al., 2013). In both studies the Juan de Fuca plate is interpreted as a dipping high resistivity zone in the southwest portion of both profiles with a depth of less that 60 km in the Insular belt increasing to 150 km in the Intermontane belt. To the northeast a higher resistivity, isolated, feature is present at approximately 50 km depth under the Intermontane belt (Soyer and Unsworth, 2006) but in Rippe et al. (2013) this feature is connected to a larger high resistivity feature that extends into the craton. The low resistivity of the back-arc at

depths of less than 50 km suggest a shallow asthenosphere in comparison with the lithosphere-asthenosphere boundary in the craton (at a depth of 200 km).

Water released from the subducting slab and mantle melts can explain the low resistivities found beneath the volcanic arc. In the back-arc upper mantle increased water content, down to a depth of 150 km, and melt fractions up to 1.5%, at less than 135 km depth, are required to explain the observed resisitivities in Rippe et al. (2013). Rippe et al. (2013) further state that the quantity of aqueous fluids and partial melt will lower the viscosity of the upper mantle which can explain the observed heat flow from geodynamic models.

3.3 Thermal measurements and models

Many different factors control the S velocity of the upper mantle, including compositional variations, anisotropy, water content, partial melt, and temperature (Hyndman et al., 2009). To relate seismic velocity to upper mantle temperature, Hyndman et al. (2009) used laboratory-based mineral elastic properties as a function of temperature, pressure, and composition. Figure 3.11 (left) shows a map of the calculated temperature at a depth of 100 km beneath western Canada using Vs tomography from the NA04 model. Figure 3.11 (right) shows the relationship between S-wave velocity and temperature for several compositions; for the Hyndman et al. (2009) study the Tecton was used for the Cordillera and Proton for the craton (modeled after Griffin et al., 2003).

Figure 3.11 shows a slice of the gridded temperature result for western Canada. Using this grid, cells were tabulated for their occurrence in either the Cordillera, craton, or volcanic arc area, creating a histogram seen in Figure 3.12. Temperature values of the Cordillera range from 1100 to 1300°C with the volcanic arc having a more consistent temperature over 1300°C for depths greater than 100 km and 1000°C

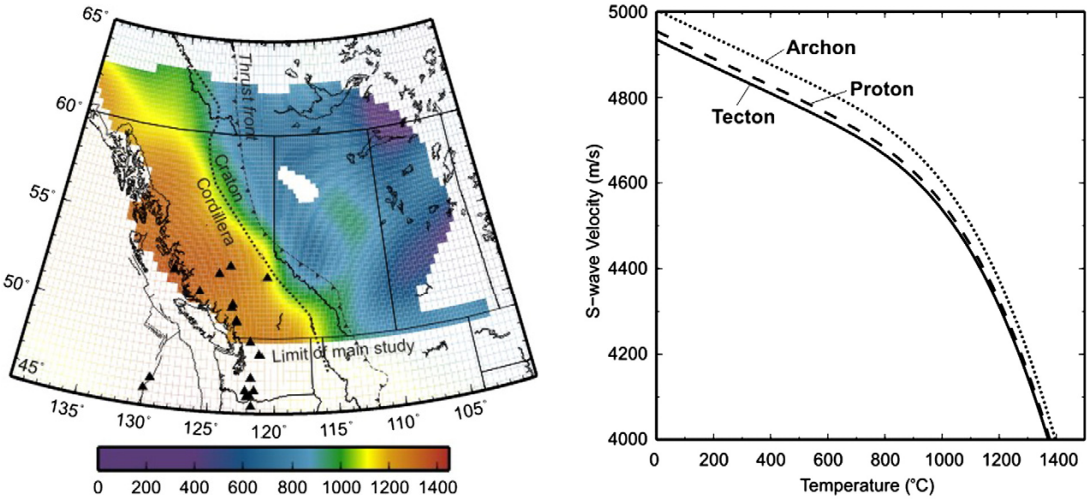

Figure 3.11: Temperature (°C) of the Cordillera and craton at a depth of 100 km (left) and the Tecton, Proton, and Archon relationships between S-wave velocity and temperature (right) (Hyndman et al., 2009).

at a depth of 60 km. The craton maintains a temperature of 800°C at depths of 60-120 km, below which it increases to 1200°C at 200 km depth. Cordillera and craton temperatures differ at depths less than 200 km with craton temperatures being up to 400°C colder. An extrapolated line based on deeper temperatures matches other xenolith and crustal temperature estimates (Hyndman et al., 2009) and shows that the upper mantle beneath the craton is hotter than xenolith estimates would predict.

The results from Hyndman et al., (2009) (Figure 3.13), when compared to other constraints, such as thermal models, show agreement between the measured slope, determined by the histogram, and previous results from the area (MacKenzie and Canil, (1998); Saruwatari et al., (2001); Currie and Hyndman, (2006)). Hyndman et al., (2009) locate the base of the thermal lithosphere of the Cordillera at a depth of 60 km, while the cratonic thermal base was inferred to be at 200 to 250 km depth. At these points the Cordillera and craton geotherms match the trend of the mantle adiabat. Craton measurements in Figures 3.12 and 3.13 show higher recorded

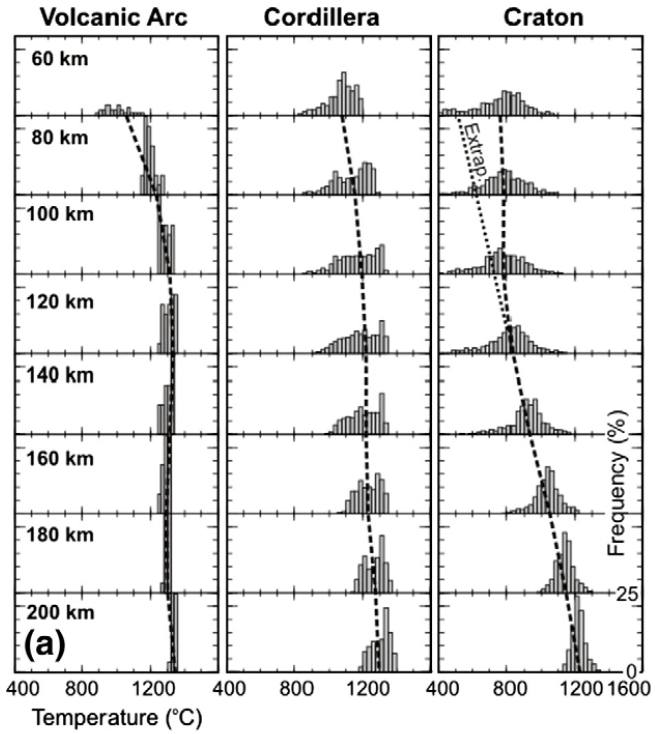

Figure 3.12: Histogram of the study area showing selected average values of the temperature (°C) at increasing depth based on the frequency of cell occurrence within the survey grid (Hyndman et al., 2009). The dashed line joins the mean values at each depth.

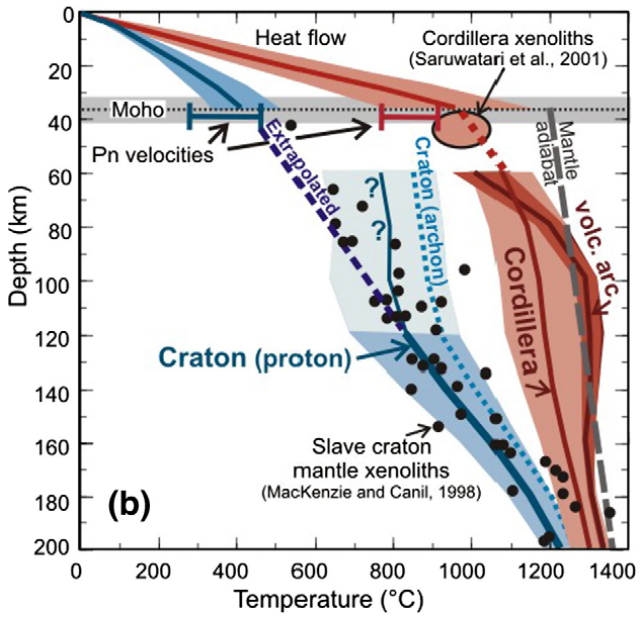

Figure 3.13: Temperature-depth plot from Vs for Volcanic Arc, Cordillera and craton compared to other constraints (Hyndman et al., 2009).

temperatures than those extrapolated from xenolith and crustal T-Z estimates. It is believed that these higher values are due to smoothing of the uppermost mantle S velocity (Hyndman et al., 2009).

TempModel1 and TempModel2 are two models produced by the inversion of observed surface heat flow values along a representative cross-section from Cordillera to craton (Hardebol et al., 2013) (Figure 3.14). TempModel1 was the reference model while TempModel2 omitted the assumption of laterally uniform layer properties (Hardebol et al., 2013). High surface heat flow observations cause difficulties for TempModel1. Instead, TempModel2 does not assume laterally uniform layer properties but allows for lateral variations in heat production, only for the Cordillera interior. These models show a shallow base of the Cordilleran thermal lithosphere at 50-60 km and a deep base of the cratonic thermal lithosphere of 175-200 km. This change in lithospheric depth occurs over a lateral distance of less than 200 km.

At a depth of 100 km within the Cordilleran thermal asthenosphere, the cratonic lithosphere temperature was modelled as approximately 1000°C corresponding to a temperature difference of 300°C. The area between the Rocky Mountain Trench and the Cordilleran Deformation Front has a difference in thermal lithosphere between the two models. In TempModel1the thickness goes from 60 km to 175 km, while in TempModel2 it goes from 80 km down to 200 km. Thermal calculations done by Hyndman et al. (2009) agree with the TempModels in locating the Cordillera/craton boundary at the Rocky Mountain Trench.

3.4 Geophysical observations of the Cordillera / craton boundary

Vp and Vs wave results from Mercier et al., (2009) show that the upper mantle beneath the Cordillera and craton shows a strong velocity contrast at the location of the Cordilleran Deformation Front, with total velocity contrast between the two of 4%. These results were seen at depths of 100 km through 300 km. Vs perturbation results from Bao and Eaton, (2015) and Bao et al., (2014) show clear distinction between Cordillera and craton with the boundary at the Southern Rocky Mountain Trench. Near seismic station SLEB (near Revelstoke, British Columbia), Miller and Eaton (2010) observed an overlapping of the Cordilleran mantle on top of the cratonic lithosphere.

Temperature models (TempModel 1 and 2) from Hardebol et al., (2013) show a sharp contrast between the thin Cordilleran thermal lithosphere and thicker cratonic thermal lithosphere. Hyndman et al., (2009) also show a sharp temperature change of 300°C, extending 200 km across the Cordilleran/craton boundary.

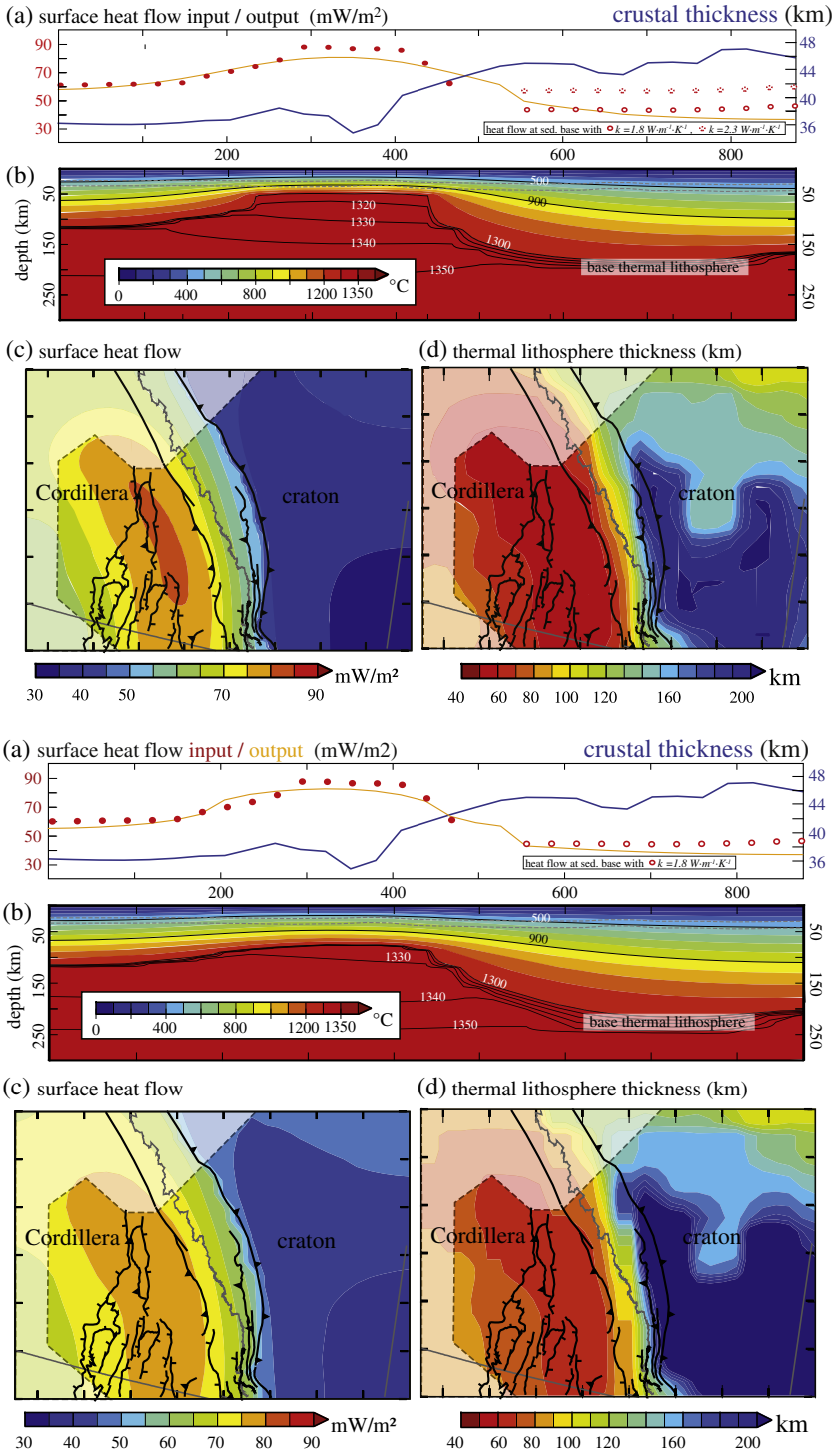

Figure 3.14: TempModel1 (top) and TempModel2 (bottom) showing base lithospheric calculations using surface heat flow observations (Hardebol et al., 2013).

Chapter 4

Approach

To study the Cordillera/craton boundary in the lithosphere, geophysical methods that are sensitive to lithospheric structure should be used. Earthquake seismology is one of the few methods which is able to image the lithospheric mantle. The following sections explain the process behind the method being used.

4.1 Seismic velocity

Jordan (1978) examined heat flow data and seismic data to find that continental lithospheric thickness is variable, with the lithospheric beneath the unstable western United States of America being thin ($<$ 100 km) but reaching depths over 400 km under stable shields and platforms. His model of thick basalt-depleted continental tectosphere, which is consistent with seismic observations, is as follows: The easiest way for lithosphere to have increased speed is by cooling it. At these depths, however, cold lithosphere below the craton should detach and be recycled in the mantle. This is not the case, as moving crustal plates above are not sheared from the cooler lithosphere below. Jordan (1988) proposed the isopycnic hypothesis, which states that the cooling lithosphere beneath cratons must undergo a geochemical change, due to

basalt depletion from garnet lherzolite, to maintain a buoyancy similar to that of the surrounding rock.

4.2 Surface-wave dispersion curves

Since the base of the lithosphere is at depths of up to 200 km or greater, the two main options of waves for imaging it in aseismic regions are teleseismic body and surface waves. It is therefore necessary to choose between using body waves and surface waves according to what best suits the focus of the study. Body waves have good lateral resolution and poor depth sensitivity, while surface waves have good depth sensitivity but will average structure laterally. Figure 4.1 shows a structural resolution test by Frederiksen et al. (2013) showing this good lateral resolution and poor depth sensitivity of body waves. But lateral resolution is also dependent on neighbouring heterogeinity of velocities. Looking at the map view recovered model in Figure 4.1, the centre of the fast velocity feature fades to a background velocity. This result shows a weakness of using body waves for heterogeneous velocities, in that it is only useful for determining boundaries between features with different seismic properties, but cannot measure absolute velocity. An additional weakness is the downward smearing of lithospheric features. This smearing is a problem for the present project due to the focus being on the imaging of the Cordilleran/craton boundary at depth.

Surface-wave velocities vary depending on period, with larger periods being sensitive to greater depths (Stein and Wysession, 2003), a property which is useful for studying earth structure. The use of surface wave tomography is an accurate way to measure the velocity of the lithosphere since it gives absolute velocity measurements unlike teleseismic body-wave tomography which provide relative velocity measurements. This is because a surface-wave seismogram can measure a broad depth range

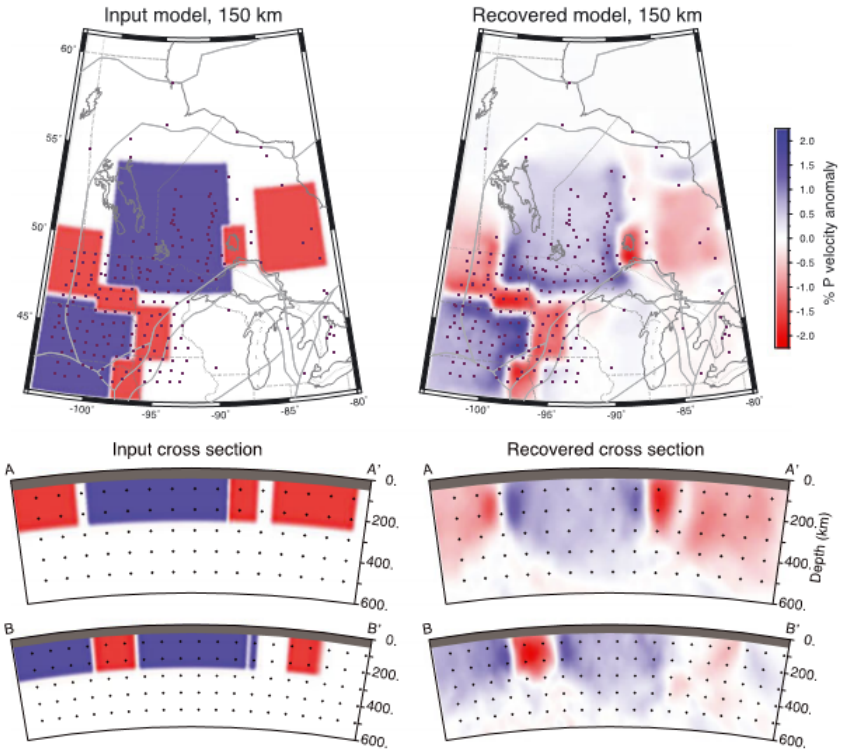

Figure 4.1: Structural resolution test, completed by Frederiksen et al., (2013), showing the degree of lateral and downward smearing of lithospheric features as imaged by teleseismic (body) waves. The left side shows the input model from map view, and two cross sections. The right side shows the recovered model of the map view and two cross sectional views.

without any along-ray averaging resulting in very good depth resolution. Both body waves and surface waves have a negative side effect of either vertical and lateral model smearing, respectively. To measure features at depth vertical smearing causes a loss in resolution.

4.3 Two-station method

There are many measurement methods available for surface-wave tomography, divided into array, one-, and two-station methods. Information can be gained from

group and phase velocity measurements or waveform fitting from one-station, two-station, and array methods. For the purpose of my research I will only be describing the one- and two-station methods, since the array method requires dense seismometer coverage, and so is not viable given the sparse distribution of stations in Canada. The one-station partitioned waveform method approach involves using a single station to record the incoming surface wave for analysis (Nolet, 1990). The method used by Nolet (1990) involves fitting the waveform with a synthetic and therefore recovering a model of velocity versus depth, averaged along the source receiver path. This averaging limits the lateral resolution, particularly if the target region lacks good seismicity distribution, and requires that a volume include both sources and receivers for modelling at the tomography stage.

To minimize this averaging effect, the two-station method can be used (Gomberg et al., 1988; Meier et al., 2004; Darbyshire et al., 2007). The two-station method involves two stations situated within a project area, for which events lying on a great-circle path that includes both stations are examined (Figure 4.2). As a surface wave passes the first station it is recorded. It then continues along this path and propagates to the second station, and a dispersion curve is derived by comparing the two recorded seismograms. The use of the two-station method cancels out the phase effects of the earthquake source function as well as the common path of the station pairs (Darbyshire et al., 2007). One caveat to this method is that the ray path must lie on or close to great circle, including the two stations, within a reasonable deviation (5°, as used by Darbyshire et al., 2007).

The results from the one-station partitioned waveform and two-station methods show that both the dispersion curve and partitioned waveform methods can be used to measure velocity as a function of depth, due to the frequency/depth relationship for surface waves. The theory behind the Rayleigh wave dispersion analysis method has been described in detail by many authors (Gomberg et al., 1988; Saunders et al.,

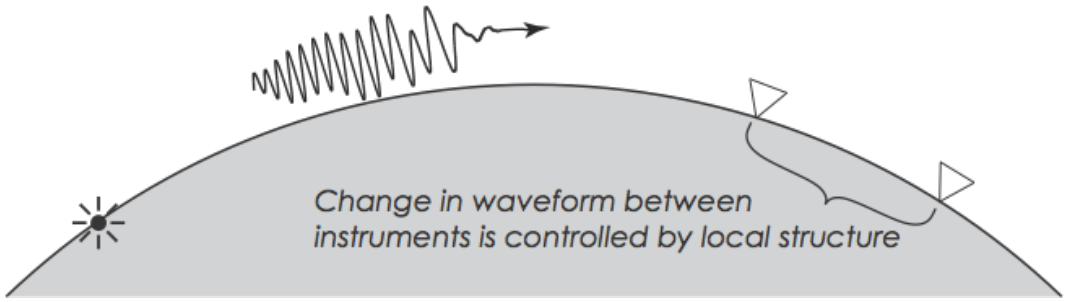

Figure 4.2: Diagram of the two-station approach with the star as the source, the wavy line as the surface wave and inverted triangles as the stations.

1998; Darbyshire et al., 2004) and can be read in detail there.

To properly calculate phase velocity between both stations it is important to be able to identify the same peaks in both recorded measurements. Due to the nature of seismic waves this is troublesome because the phase may differ by a factor of $2n\pi$ radians where n is an integer. This factor can greatly change the velocity measured. To approach this problem a comparison of the waveform, compared to the fundamental mode phase velocity, is done at low frequency, at which 2π radians corresponds to an unrealistically large velocity change. Then a smooth dispersion curve is assumed. The number of phase velocity curves measured, per path, varies based on numerous factors such as times of observation, location of earthquake with respect to station pair paths along the great circle trace, or malfunction of instruments during data collection.

Phase velocity determination of the fundamental Rayleigh mode was based on the Meier method (Meier et al., 2004). The phase velocity dispersion curves were calculated from vertical component seismograms using the multiple-filter technique, in which a set of Gaussian filters were applied to create bandpass-filtered time signals. The Meier method uses cross-correllograms for determining phase velocities between

stations. A more complete description of the process of waveform selection for dispersion curve measurements is discussed in section 5.3 of the next chapter. For each two-station pair these curves were averaged over all events and include error bars representing the standard deviation of the single dispersion curves.

4.4 Dispersion curve to depth inversion strategy

Linear inversion, using code created by Alexey Bryksin, created a dispersion map (via tomography) of the survey area using all averaged dispersion curves. The inversion program is used to produce dispersion maps of the survey area at determined periods. These tomographic images display 2-D distribution of phase velocity across the entire survey area, where coverage is sufficient.

In order to relate these maps to a real world model the results are required to be dependent on depth rather than dependent on period. To do so, depth inversion is required to create models of S velocity with respect to depth. Various 2-D models were inverted since 3-D modeling was considered to be beyond the scope of this project. This was done firstly, by selecting numerous profiles located on and through points of interest identified in the dispersion maps. These profiles were then broken up into 50 km intervals (due to the length of the profiles), and numerous 1-D inversion were carried out for each interval. These inversions were done using an iterative approach to invert the S-wave velocity and then update the P-wave velocity using a fixed Poisson's ratio of the initial model with a new density. The density was calculated from the updated P-wave velocity using the Nafe-Drake relation (Herrmann, 2013). The numerous 1-D inversions were then plotted side by side sequentially to provide a velocity model of the subsurface.

Chapter 5

Data and methods

5.1 Instrumentation

Canada is instrumented by the Canadian National Seismic Network (CNSN) operated by the Geological Survey of Canada. The network consists of 314 seismic broadband stations as of June 11, 2015, as listed on Natural Resources Canada's Earthquakes Canada website[1]. The Portable Observatories for Lithospheric Analysis and Research Investigating Seismicity (POLARIS) network adds more stations to be used in western and northern Canada. For this project, I selected stations located primarily in western Canada using the POLARIS and CNSN networks. Seismic stations in this area range in date of deployment from 1990 until the present. The number of stations in service is not consistent, over time, since some stations were deployed for temporary experiments while others are permanent installations.

[1] http://www.earthquakescanada.nrcan.gc.ca/stndon/data_avail.php

5.2 Event selection, data acquisition and preprocessing

The United States Geological Survey's Preliminary Determination of Epicenters (PDE) catalogue was used to populate event lists[2]. To select events likely to have a good signal to noise ratio, two criteria were used: firstly, earthquakes with magnitude 6 or greater. This is to ensure that the energy given off by the event is sufficient for long-distance recording and analysis. A list of events with magnitudes greater than 6 was saved into a Matlab MAT-file named quakes.mat containing 2128 earthquakes. This event list spans 23 years, from 1990 until May 2013.

The select_pairs_gui.m Matlab script is an interactive script that allows selection of station pairs through a graphical user interface. When two stations are selected the script will search the instrument list and the event list and apply the second criterion: station-pair paths must lie within 5° of the same great circle trace as the source. The reason behind this requirement is the assumption that the change in waveform between two stations is controlled by the structure along the great-circle path between the two. The larger the angle between stations, the less accurate this assumption is. The final station-pair paths chosen are shown in Figure 5.1.

The script ftp_request.m was used to request data from the CNSN server[3]. This process is email based, whereby an email is sent to an AutoDRM server hosted at the Geological Survey of Canada. When a reply email indicates that the data is ready, the data is downloaded in the SEED format and then converted to the SAC format using a shell script (preprocess.sh). This conversion is necessary for constructing dispersion curves for each station pair path using the technique described by in Meier et al. (2004). The Meier et al. program was modified by Alexey Bryksin to be automated

[2]http://earthquake.usgs.gov/data/pde.php
[3]ftp://seismo.NRCan.gc.ca

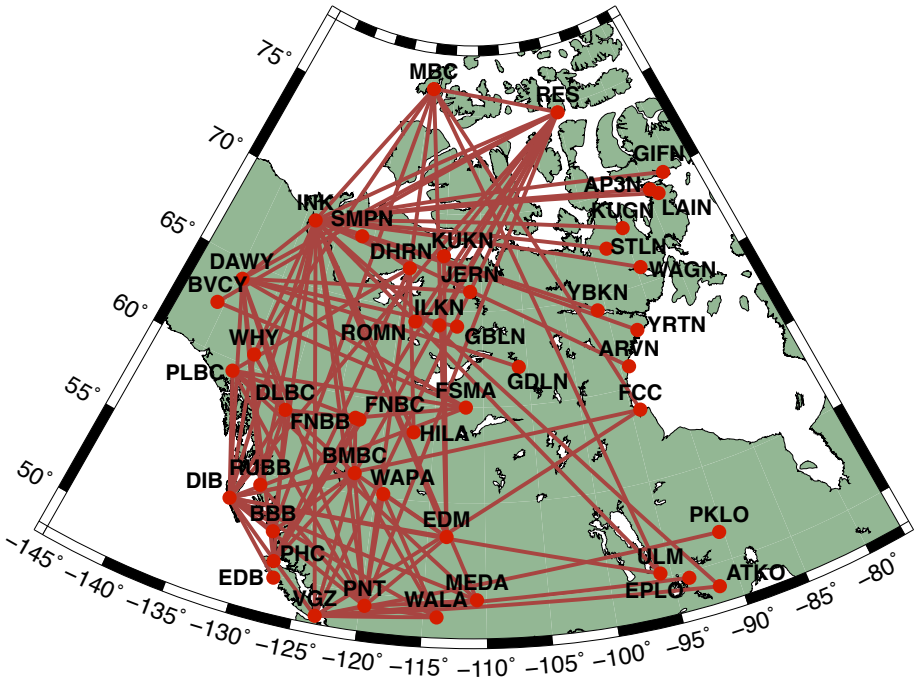

Figure 5.1: Chosen station-pair paths for the western Canada study area.

for use with this data source.

5.3 Dispersion curve measurement

Upon executing pvtmy_2013.m in MATLAB an interactive window appears as shown in Figure 5.2. The waveforms of the two stations and the cross-correlation function have an automatically determined group travel time for the fundamental Rayleigh mode represented by a solid white line. In order to obtain an acceptable measurement, both stations and their cross-correlation must have a realistic pattern for amplitude and group travel time. The upper right plot in Figure 5.2 has solid lines indicating the array of possible phase velocity curves determined from the phase of the cross-correlation function. The dashed line shows the phase velocity of the fundamental Rayleigh mode for an initial model. The reason for the multiple blue

lines is due to the phase unwrapping problem. As phase is an angle, a phase of ϕ is indistinguishable from $\phi + 2\pi$; thus, each phase measurement corresponds to a series of possible phase velocities. When selecting a blue line, it is best to do so at low frequency since factors of $\pm 2n\pi$ are much more different than at high frequency and it is likely that only one value will be realistic. Higher frequencies are then measured by assuming that the dispersion curve is smooth.

5.4 Quality control

Once all dispersion curves are selected, it is important to double-check these curves to ensure they are all reasonable and consistent. In this case a reasonable range was chosen to be $\pm 5\%$. Quality control of the dispersion curves consists of identifying curves that lie outside of a $\pm 5\%$ range around the average curve and either editing their data file or deleting the entire curve (Figure 5.3). Two curves were deleted entirely due to a large portion of their measurements being outside this area and twenty-nine curves were edited. These edits simply involved deleting velocity information for each corresponding period outside the $\pm 5\%$ area. The goal was to delete as little information so as possible to keep a large amount of useable data. This is the reason why, at periods ranging from 50-70 seconds, there are some stray dispersion curves leaving the $\pm 5\%$ range. The only way to fix this issue was to delete the entire dispersion curve, which was deemed less helpful. Figure 5.4 shows the final set of dispersion curves after editing.

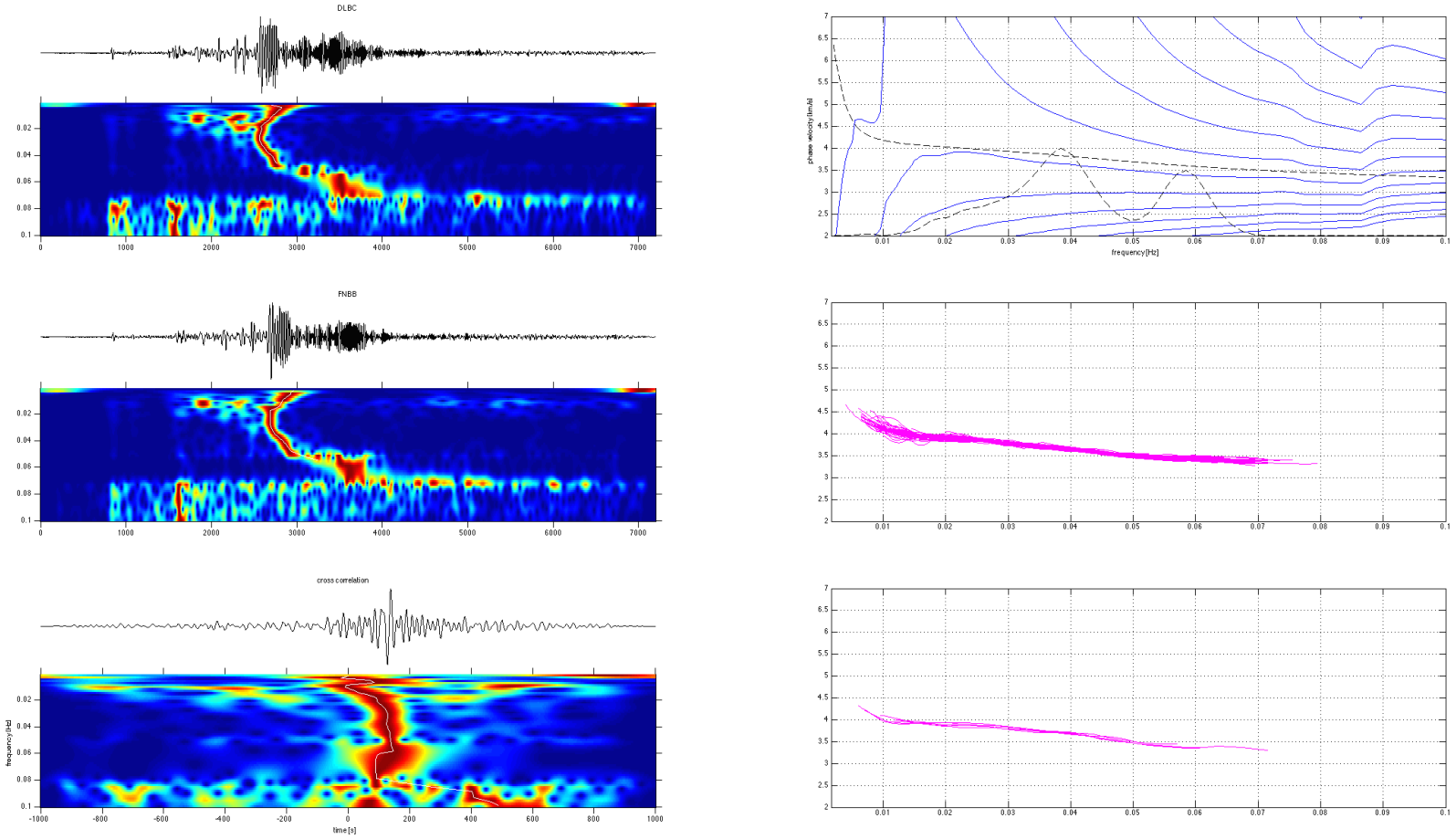

Figure 5.2: Determination of the phase velocity using a two-station method as developed by Meier et al., 2004 for stations DLBC and FNBB. On the left are waveforms of the two stations with amplitude as a function of time (s) and frequency (Hz) as well as the cross-correlation of the two stations on the bottom. On the right top is a representation of the array of possible curves calculated from the cross-correlation. The first dashed line represents the fundamental Rayleigh mode for the initial model, while the second is the amplitude normalized spectrum of the cross-correlation function. The remaining plots are previously selected phase velocity curves sorted by direction of propagation.

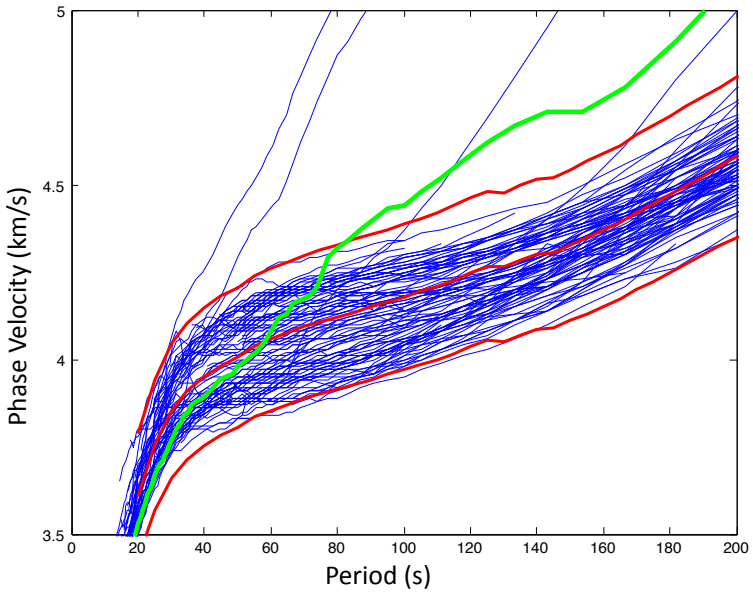

Figure 5.3: All dispersion curves plotted for quality control. Red lines indicate mean dispersion curve measurement (center) and ±5% range measurement (top and bottom). The green line is a highlighted dispersion curve for quality control.

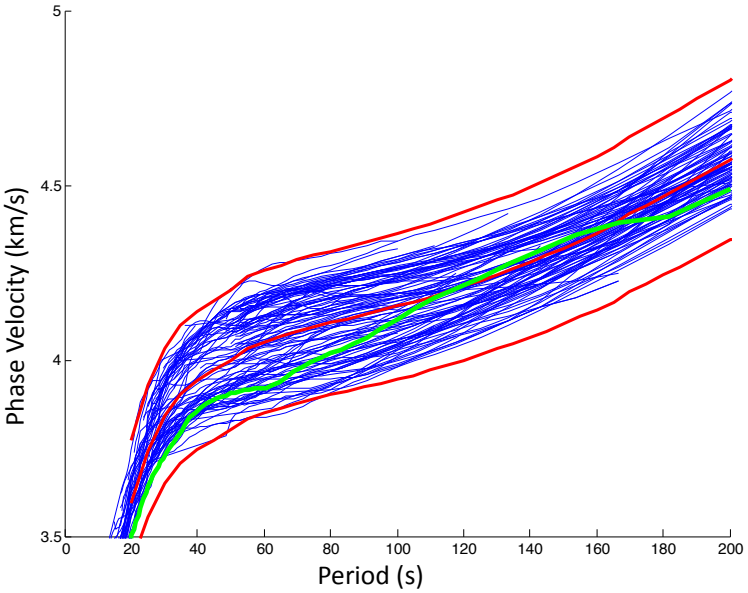

Figure 5.4: Edited path analyzed dispersion curves.

5.5 Dispersion mapping

5.5.1 Map of individual dispersion curves

Now that all of the dispersion curves have been selected and edited for quality, they may be plotted in map view showing their respective velocities at various fixed periods. Figure 5.5 shows an example of a map view plot for a period of 40 seconds. Velocity-shaded paths are plotted to examine the spatial pattern of velocity variations of the area. Blank spaces are due to a lack of station coverage between stations or at this period. These areas show the need for the required dense coverage in regard to station pairs. These maps were then input to a tomographic inversion to create tomographic images at various periods. Discussion of this work and other maps is presented in Chapter 6.

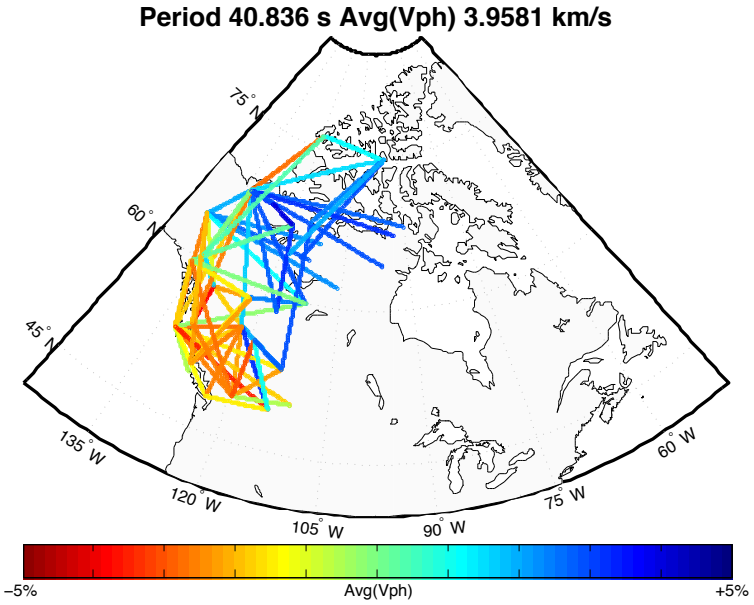

Figure 5.5: Visualization of individual path velocities on a map with a fixed period of 40 seconds. Velocity is given as a percentage variation from the average value at this period.

5.5.2 Model cell coverage and inversion

Velocity-shaded path maps obtained through tomographic inversion provide a map view of the velocity of the lithosphere at various periods, averaged along 2-station paths. The averaging was removed through tomographic inversion to map how the phase velocity varies laterally in the study area. The construction of these velocity maps is done assuming the dispersion curves from the previous section represent averages along the great-circle path. The study area was split into a cell grid with width 2° (longitude) and height 1° (latitude) as seen in Figure 5.6. The coverage pattern is much denser west of 100° due to station availability, and to increase the coverage of the Cordillera/craton boundary. Most paths east of 100° are part of longer station pair paths that contribute to denser coverage in the west.

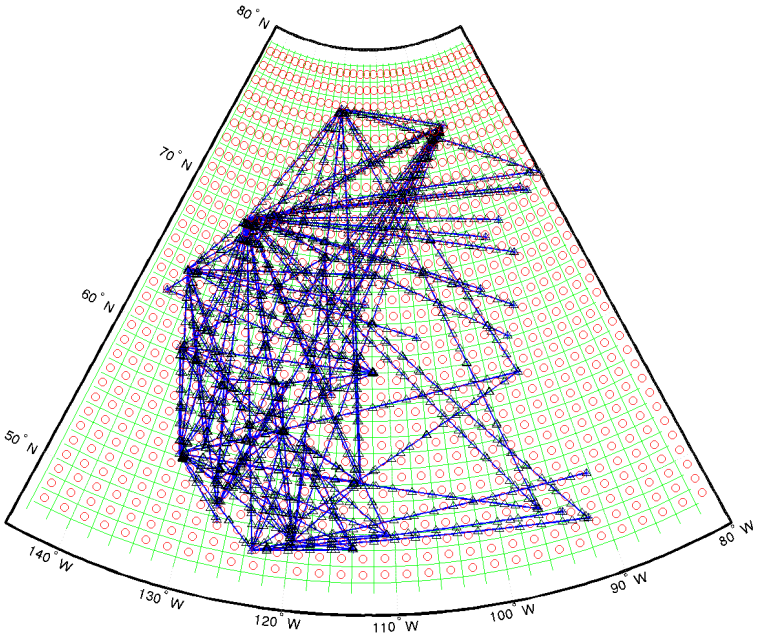

Figure 5.6: Cell grid with width 2° (longitude) and height 1° (latitude). Circles correspond to each individual cell. Blue lines show paths along the great circle trace between pairs of stations with blue triangles indicating that the waveform was traveled into a cell.

Following discretization a check is done to see if each cell is active, meaning that at least one path crosses through the cell, in which case its coordinates are stored for inversion. Once the checks are completed, information about velocities and errors are taken from each station pair path and centralized into one file for inversion.

Inversion of the dispersion curves was done using a 2-D tomographic approach for each period. Using the ray-theory approximation, the seismic phase velocity, at a given frequency, is dependent on only the average phase velocity along the travel path between each station pair. Before we can continue two modifications must be made. First, we change the velocity variable to slowness (the reciprocal of the velocity). Second, we must assume that the ray path is independent of surface wave velocity. By doing so we assume that our starting assumption of a great-circle ray path is valid. The travel-time path integral is then:

$$\overline{s} = \frac{1}{L} \int_{\Gamma} s \mathrm{d}l \tag{5.1}$$

where s is the slowness, Γ is the ray path, and L is the total path length. For a two-dimensional area the ray passing through active cells are assumed to be along the great-circle. The average slowness within a cell (i) is

$$\overline{s} = \frac{l_i s_i}{L} \tag{5.2}$$

Since the entire ray lies within active cells, the average slowness for the jth ray will be

$$\overline{s}_j = \sum_{i=1}^{N} \frac{l_{ji} s_i}{L_j} = \sum_{i=1}^{N} A_{ji} s_i \tag{5.3}$$

which is essentially matrix-vector multiplication where the matrix A_{ji} contains the lengths of appropriate ray segments. For the case of tomography, we assume

that we have a constant-velocity base model, and so we expect the rays to be great circles as per the requirements of the two-station method. These rays will remain approximately straight as long as the velocity variations are a small percentage of the base-model velocity.

Smoothing is the most common form of regularization for ray-based tomography. The rays are narrow and will produce narrow, along-ray, anomalies if damping regularization is used, while smoothing can be used to favour long-wavelength anomalies. Smoothing therefore simplifies the model as much as the data will allow which will lead to more interpretable results. To balance the model roughness and misfit a trade-off curve was created (Figure 5.7) to determine the optimal smoothing weight for inversion. The purpose of the trade-off curve is to find the choice of model parameters that results in the lowest model roughness with a reasonable model misfit. This choice is subjective but is generally a point located along the bend of the curve as seen in Figure 5.7. From the trade-off curve, the smoothing weight was chosen as 5,000,000 km^2. Flattening and damping weights were set to one millionth the smoothing rate where flattening has a unit of km and damping is unitless.

With these parameters set, the inversions were performed for periods of 30 to 160 seconds at intervals of 10 seconds. The tomographic image for a period of 30 seconds is shown in Figure 5.8. The results of inversion for all periods will be presented in Chapter 6.

5.6 Pseudosections

The tomographic images explained in the previous section were used to create psuedosections. Pseudosections are plots of phase velocity, with horizontal position along one axis and a depth proxy (period, in this case) along the other axis. Pseudosections were created along eight profiles. This was done by dividing each profile into

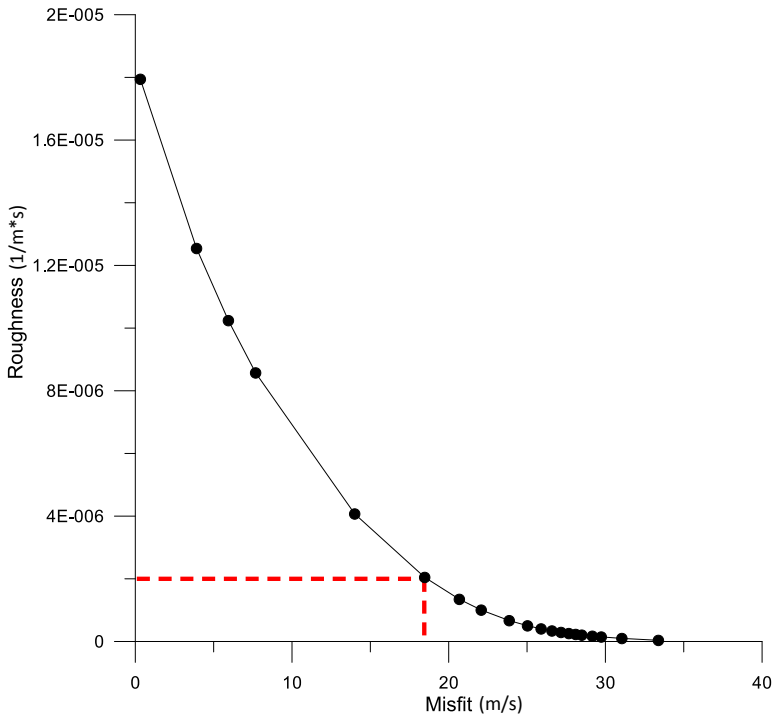

Figure 5.7: Trade off curve used for selecting the optimal model smoothing weight. Dotted red line indicates the model roughness chosen (2×10^{-6}) giving a misfit of about 18.5.

individual 1-D columns with a spacing of 50 km. The resulting velocity and period data was sampled from the tomographic images. The start and end locations of the profiles are listed in table 5.1. The profiles are plotted in Figure 5.9.

The profiles were chosen to examine various interesting features discovered from the velocity maps. Profiles 1 -3 were chosen to examine the Cordillera/craton boundary, crossing the boundary at different places, to sample the boundary in different locations. Profile 4 was chosen to image along the Tintina fault. Profiles 5 (east/west) and 6 (north/south) bisect a velocity anomaly in the area around the Great Slave Lake. Profiles 7 and 8 allow comparison of the results from this thesis and those of Bao *et al.*, (2014) and Miller and Eaton (2010), respectively. The Profile 4 pseudosection is shown in Figure 5.10.

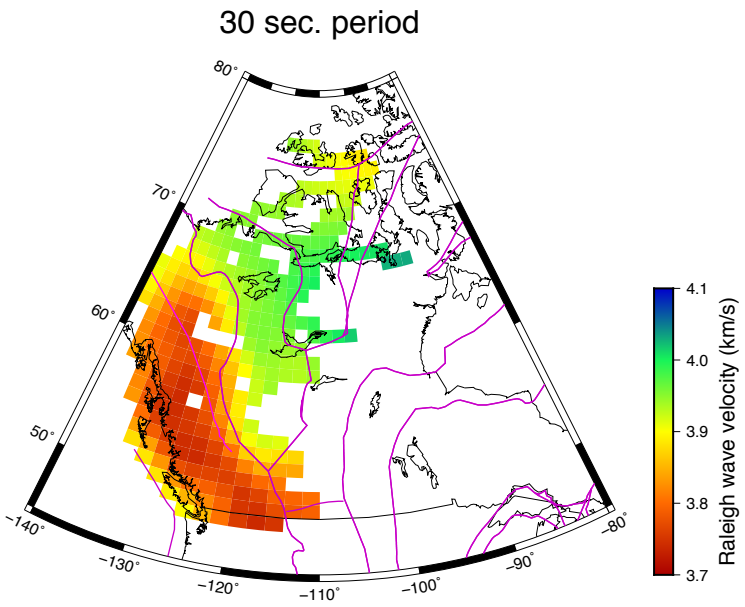

Figure 5.8: Tomographic image of western Canada at a period of 30 seconds. Lines in purple are major tectonic boundaries of Canada and the approximate location of the Tintina fault in British Columbia. Cells left as white are not sampled by paths.

5.7 Depth inversion for cross-sections

A Matlab script was created to organize the period and velocity data from the pseudosections into a format that can be read by SURF96. SURF96 is part of a suite of computer programs used in seismology for inversion of surface waves, receiver functions, and crustal structure (Herrmann, 2013). It is used for the inversion of surface waves using dispersion curves to obtain models of velocity with respect to depth instead of proxy depths measured in period. In addition to the data file, SURF96 requires a set of parameters stored in a file called sobs.d. The variance selected was based on the observed standard deviation of the fundamental mode Rayleigh wave phase velocity. The data were inverted for S-velocity with a fixed Poisson ratio and determination of density from P-velocity. This inversion technique iteratively determines the S-wave velocity and then updates the P-wave velocity using

Table 5.1: Profiles selected to create pseudosections and cross-sections

	Start		End		Profile Notes
Profile	Lat.	Long.	Lat.	Long.	
1 (A-A')	49°N	-127°W	58°N	-98°W	Southern Canadian Cordilleran
2 (B-B')	53°N	-133°W	68°N	-90°W	Mid Canadian Cordilleran
3 (C-C')	58°N	-135°W	75°N	-98°W	Northern Canadian Cordilleran
4 (D-D')	66°N	-140°W	49°N	-116°W	Along Tintina fault
5 (L-L')	62°N	-130°W	62°N	-110°W	Bisecting Slave Lake east / west
6 (S-S')	67°N	-116°W	57°N	-116°W	Bisecting Slave Lake north / south
7 (X-X')	49°N	-125°W	59°N	-93°W	Modeled after Miller and Eaton, 2010
8 (Y-Y')	49°N	-123°W	55°N	-112°W	Modeled after Bao *et al.*, 2014

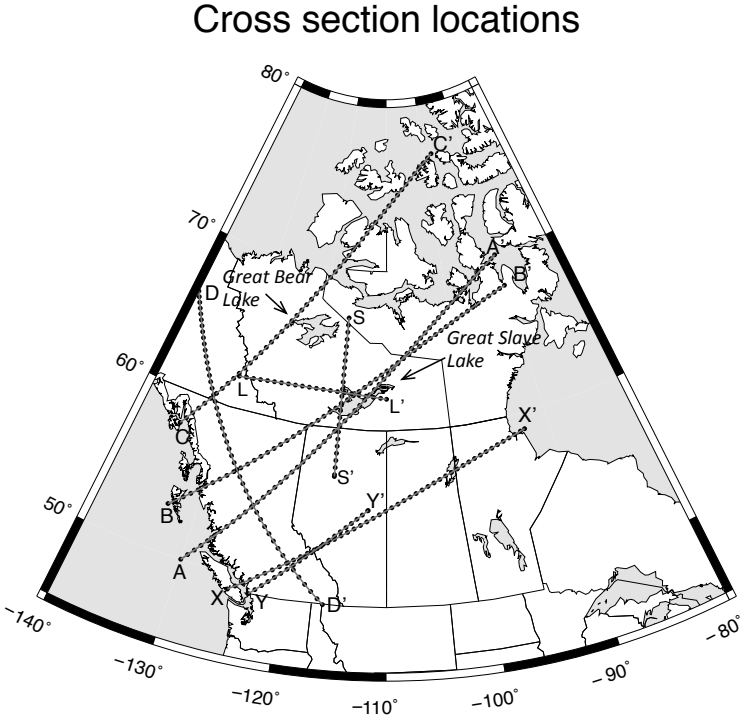

Figure 5.9: Locations of profiles used for pseudosections and cross-sections listed in Table 5.1.

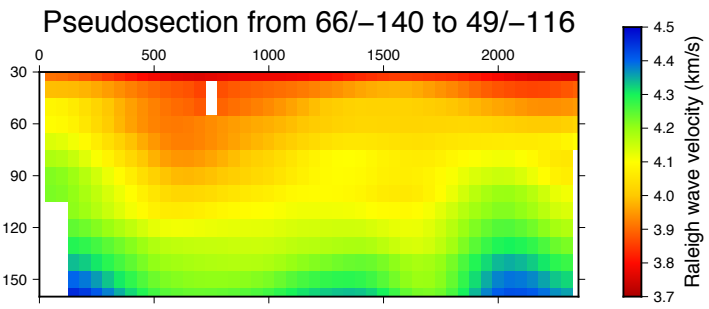

Figure 5.10: Pseudosection for profile 66/-140 to 49/-116. The horizontal axis of the plot is kilometres where 0 km is the starting point of the profile and the vertical axis is the period. Blanks in the plot are due to no data for the cell.

the same Vp/Vs ratio as in the starting model.

The first initial model was based on the approach of Darbyshire et al. (2004) in having seven layers: upper crust, lower crust, top mantle, mantle lithosphere, asthenosphere, deep upper mantle, and a half-space below the 410 km discontinuity, all with velocities based on the constraints of Shapiro et al. (1997). These layers were adjustable in depth, but generated a non-realistic representation of the mantle, in comparison to reference models such as IASP91. As they are more unstable in inversion a twenty-two-layer model was instead used with a fixed thickness for all layers. This parameterization provided a smoothly varying model, which is expected for the mantle. The model is shown in Figure 5.11 and the list of velocity and thickness values in Table 5.2.

The initial model uses P and S velocities from IASP91 (Kennett and Engdahl, 1991) with mantle layer thicknesses of either 15, 20 or 25 km. Layer thickness were chosen to coincide with IASP91 transitions. Five total iterations were completed for each profile alternating between velocity only or depth only being inverted (for the 7-layer model only). Fixing one of the parameters (either depth or velocity) eliminates a depth/velocity trade-off, making the inversion more linear.

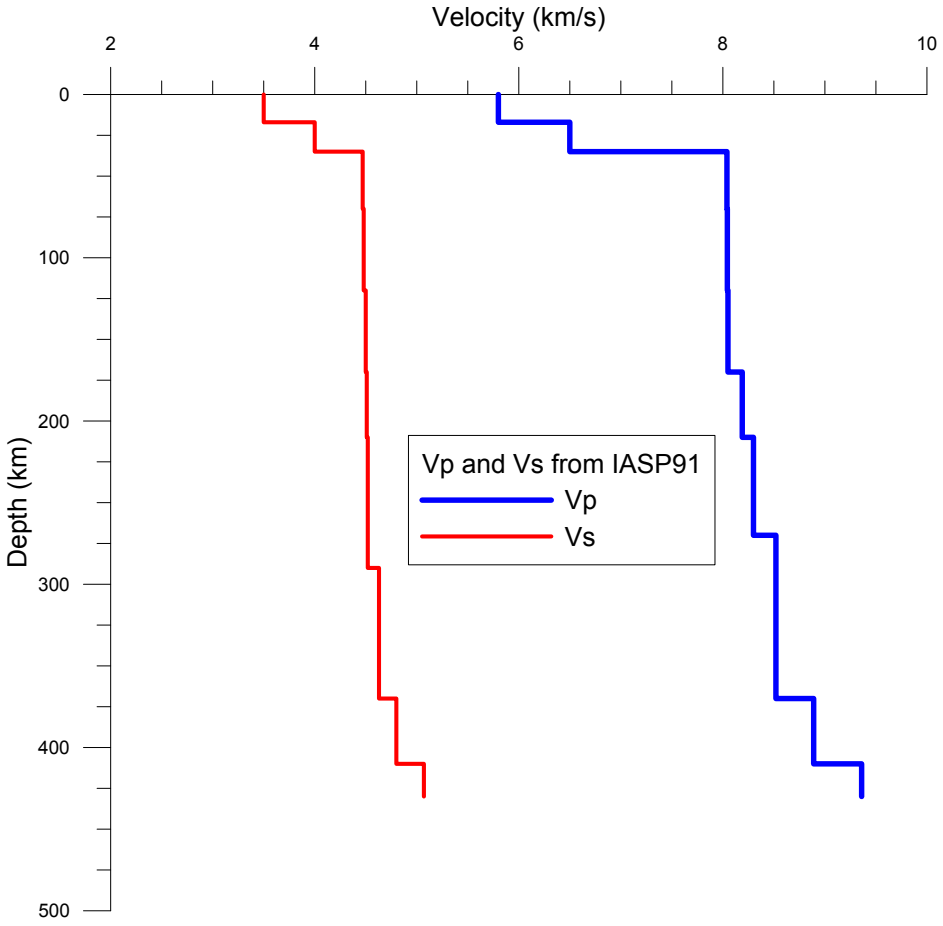

Figure 5.11: Plot of Vp and Vs versus depth used for the twenty-two layer model. These velocities, and transition zone depths, were based on IASP91 (Kennett and Engdalh, 1991). Numerical values used are shown in Table 5.2.

Table 5.2: Initial model used for all inversions

Layer Thickness (km)	Vp (km/s)	Vs (km/s)
17.0	5.800	3.50
18.0	6.500	4.00
20.0	8.040	4.47
15.0	8.040	4.47
25.0	8.044	4.48
25.0	8.044	4.48
15.0	8.050	4.50
20.0	8.050	4.50
15.0	8.050	4.50
20.0	8.190	4.51
20.0	8.190	4.51
20.0	8.300	4.52
20.0	8.300	4.52
20.0	8.300	4.52
20.0	8.520	4.63
20.0	8.520	4.63
20.0	8.520	4.63
20.0	8.520	4.63
20.0	8.520	4.63
20.0	8.890	4.80
20.0	8.890	4.80
0.0	9.360	5.07

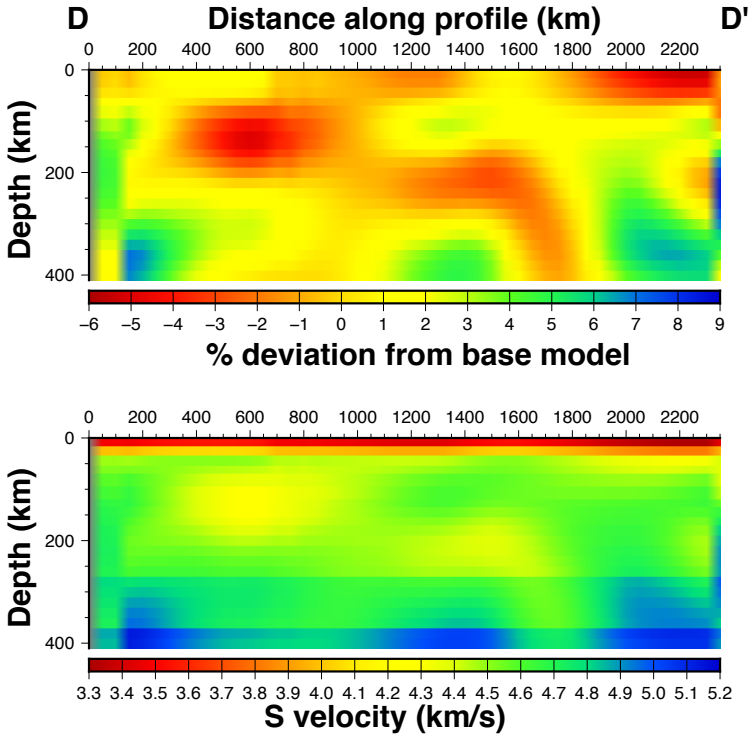

Figure 5.12: Cross-section of profile 4 (D-D') inverted from the pseudosection in figure 5.10. The top plot of the figure plots the velocity variation relative to the base model while the bottom plot shows the absolute S-wave velocity.

The values in Table 5.2 are the base model used as the starting model for each inversion for every profile pseudosection. Figure 5.12 is a cross-section, inverted from the pseudosection data of profile 4. The vertical axis corresponds to depth in kilometres and the horizontal axis corresponds to distance along profile from the starting location. The cross-sections created were not re-interpolated. The smoothness of the cross-sections is as a result of the data.

Chapter 6

Dispersion Curves

6.1 General discussion

From dispersion analysis, I obtained dispersion curves for 106 two-station paths. These two-station paths were split into three geographic groups based on the end-point locations: Cordilleran, platform/cratonic, and combined. The Cordilleran and platform/craton paths lie within the respective areas and the combined paths have one end station in each area. This division allows the ability to examine velocity differences at depth between paths solely in the Cordillera and solely outside of the Cordillera. The reason for this split is that I expect a change in velocity across the Cordillera/craton boundary. The combined group will not be used for east and west comparison since the ray paths sample both regions and will average out differences between them.

Figure 6.1 shows dispersion curve plots for the Cordilleran and cratonic groups. At short periods, the cratonic dispersion curves increase in velocity more than the Cordilleran dispersion curves. In the period range from 25 seconds to 30 seconds the Cordilleran curves have an approximately constant velocity of 3.80 km/s and then the velocity gradually increases with increasing period. At 200 seconds the velocity

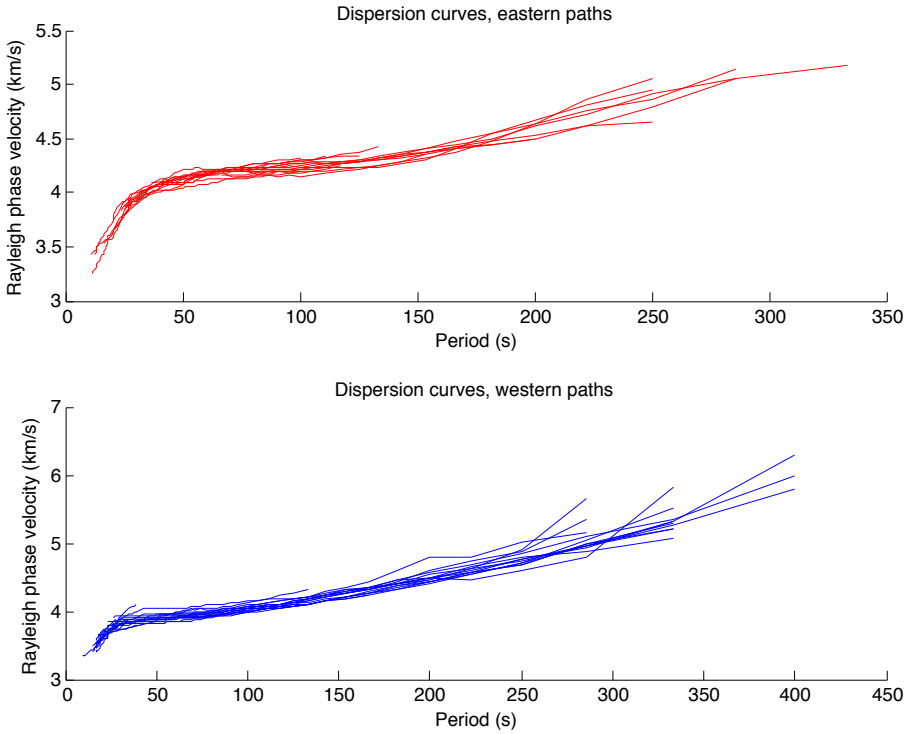

Figure 6.1: (Top): Measured phase velocities versus period for cratonic paths. (Bottom): Measured phase velocities versus period for the Cordilleran paths.

is 4.5 km/s. At periods of 250, 300, and 350 seconds multiple curves deviate greatly, possibly due to increasing error in the readings.

For the craton the velocity is 4.0 km/s at a period of 30 seconds. A plateau of constant velocity extends from at 80 seconds to 140 seconds, and the velocity starts to increase. It reaches a value of 4.5 km/s at 200 seconds. At 175 seconds, the dispersion curves start to diverge, but not as strongly as for the Cordilleran curves.

Figure 6.2 shows the dispersion curves for the DIB-PNT station pair, which is an example of an entirely Cordilleran pair. The start of the DIB-PNT dispersion curve begins at a velocity of about 3.6 km/s and a period of 18 seconds. With increasing period the velocity increases until 40 seconds where the velocity hits a plateau of about 3.85 km/s and maintains this velocity for a period range of about 20 seconds. At 60

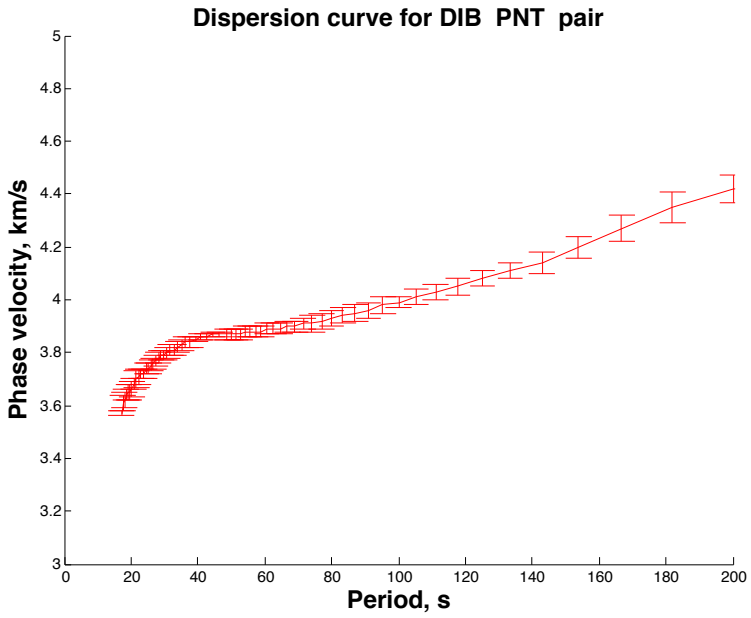

Figure 6.2: Dispersion curve for the DIB-PNT station pair.

seconds the increase in velocity is linear with increasing period. Velocity increases to 4.4 km/s at a period of 200 seconds. At later periods there is an increase in error as seen by the growing size of the error bars, which were calculated using the uncorrected sample standard deviation of the phase velocities of individual events.

The DHRN-HILA dispersion curve (Figure 6.3) is an example of an entirely cratonic pair. It has a velocity of 3.7 km/s at a period of 20 seconds and sharply increases to 4.0 km/s at a period of 35 seconds. At 60 seconds the velocity is about 4.2 km/s and increases at a lower rate. The dispersion curve increases to a velocity of 4.35 km/s at a period of 160 seconds. Error is greatest in the 50-70 second range. Comparison of the examples show that the Cordilleran pair is slower at shorter periods than the cratonic pair. At increasing period, the cratonic pair reaches a final velocity at a shorter period than the Cordilleran pair, with both pairs having the same final velocity.

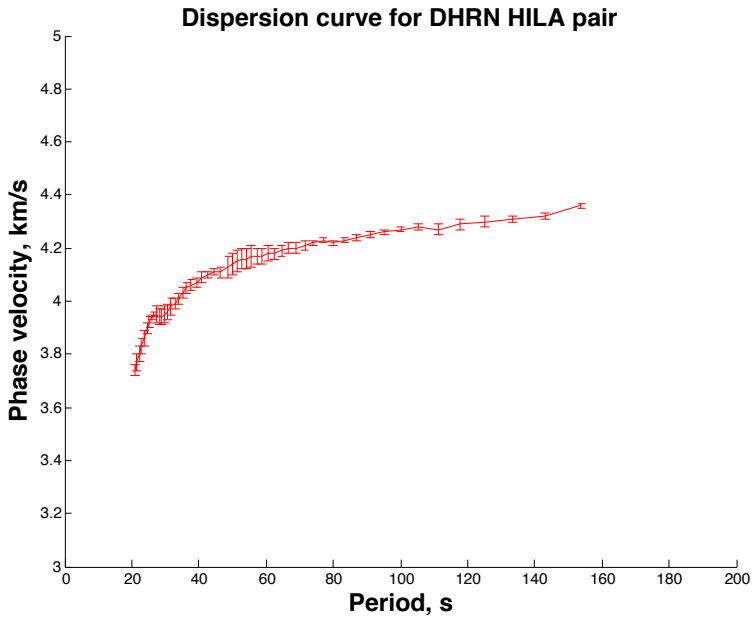

Figure 6.3: Dispersion curve for the DHRN-HILA station pair.

6.2 Average dispersion curves east and west of the Cordilleran Deformation Front

Figure 6.4 shows the arithmetic averages of all dispersion curves entirely on each side of the Cordilleran Deformation Front. From 20-25 seconds, the velocities of both areas are equal to within the error and increase at approximately the same rate. At 40 seconds, the cratonic and Cordilleran curves diverge, with Cordilleran velocities flattening out at 3.88 km/s at around 40 seconds and the cratonic velocities flattening out at 4.18 km/s at around 65 seconds. At periods longer than 65 seconds the Cordilleran velocities increase more than the cratonic velocities, with increasing period. At periods over 150 seconds overlapping of some craton and Cordillera dispersion curves is seen. The separation of the mean values of both phase velocities is greater than the estimated standard error of 0.015 km/s (based on 16 station paths

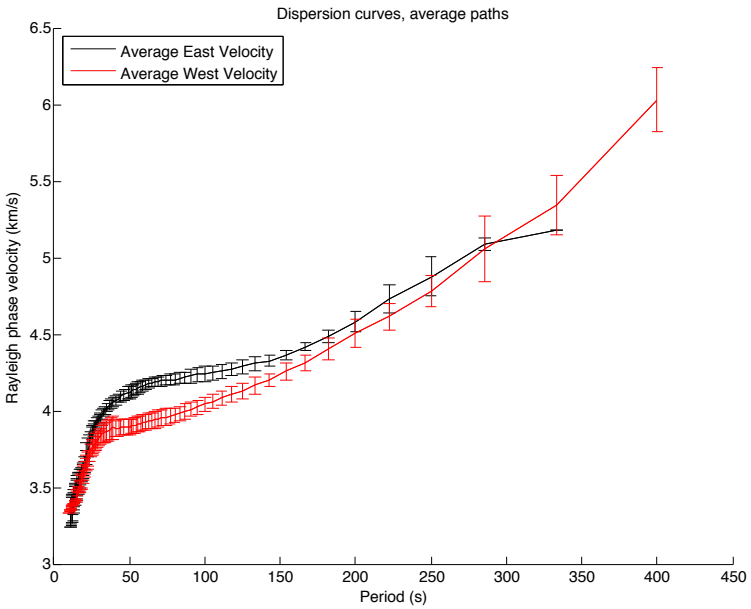

Figure 6.4: Average velocity dispersion curves to the craton and Cordillera.

with a standard deviation of approximately 0.05 km/s) indicating a resolved velocity difference of this period range of 150 to 250 seconds. Error for both cratonic and Cordilleran paths ranges from 2-9% with most values being 6-7% in the craton and 5% in the Cordillera. These errors are the standard deviation of the set of path dispersion curves. Models obtained by inverting the craton and Cordillera average curves will be shown and explained in Chapter 8.

Figure 6.5 shows the difference in velocities between cratonic and Cordilleran phase velocity curves. At a period of 20 seconds, a sharp increase in velocity difference starts at about 50 m/s and is greater than the standard deviation. It reaches its maximum of 248 m/s at a period of about 65 seconds. After this period the velocity difference decreases. The smoothness of the graph is a result of the overestimation of the error explained earlier.

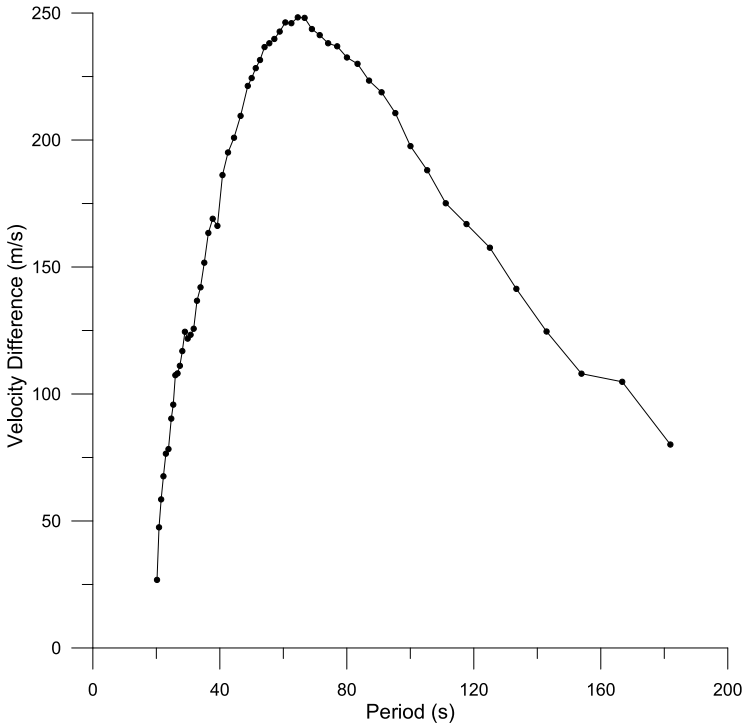

Figure 6.5: Velocity difference between average velocity dispersion curves in the craton and Cordillera. Periods have been edited to range from 20 to 182 seconds to highlight the difference in velocity which is greater than error. Velocity difference is greater than error from 25 seconds until 166 seconds.

Chapter 7

Velocity maps

7.1 Path velocity maps

The individual two-station pair paths shown and discussed in the previous chapter are now used to create shaded maps of path velocities as explained in Chapter 5. These path velocity maps show phase velocities at a single period for all paths, in map view, and thus show velocity and coverage in the survey area. A total of 8 maps were produced with periods of 40, 50, 60, 71, 80, 100, 125, and 142 seconds. These periods were chosen to show a good range of periods (and therefore depths) across the span of measured dispersion curves.

At a period of 40 seconds (Figure 7.1) a divide between slow and fast velocity is evident, with a large proportion of orange and red lines (corresponding to -2 to -4 % relative to the average of all paths) in the southwest and light and dark blue (corresponding to +2 to +5 %) in the northeast of the study area. The poor coverage is due to 40 seconds being a relatively short period for which many of the longer paths are lost, as short periods are harder to measure on longer paths.

At 50 seconds (Figure 7.2) there is an increase in coverage provided by longer paths to the north of 60°N latitude. Paths with endpoint locations in the northwest

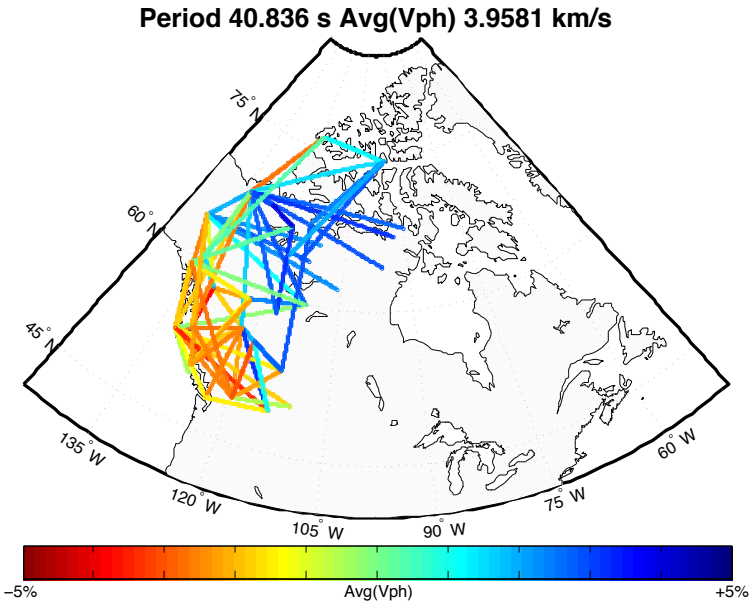

Figure 7.1: Visualization of individual path velocities on a map for a period of 40 seconds. Colour indicates deviation from the average velocity at this period, in percent.

and southwest further confirm the slow southwest velocity values of -2 to -4%. The new coverage to the north further confirms the faster velocities of +2 to +5%, relative to the average.

The change in coverage from 50 to 60 seconds is the greatest, since nearly all 105 station-pair paths are accounted for in Figure 7.3. At this period, station-pairs of greater distance are more prominent and increasingly show a fast velocity to the east. Many long distance paths start from station VGZ in the Cordillera, showing an increase in velocity in the centre of the Cordillera (due to an increase in cratonic velocity sampled for any Cordillera/craton paths) thereby moving the slowest velocity paths primarily to the west. Most of these paths cross through both the Cordillera and the platform/craton which causes an averaging of velocity.

The results for periods of 71 (Figure 7.4) and 80 (Figure 7.5) seconds are very similar. Both show a decreasing velocity percentage moving from the centre of the

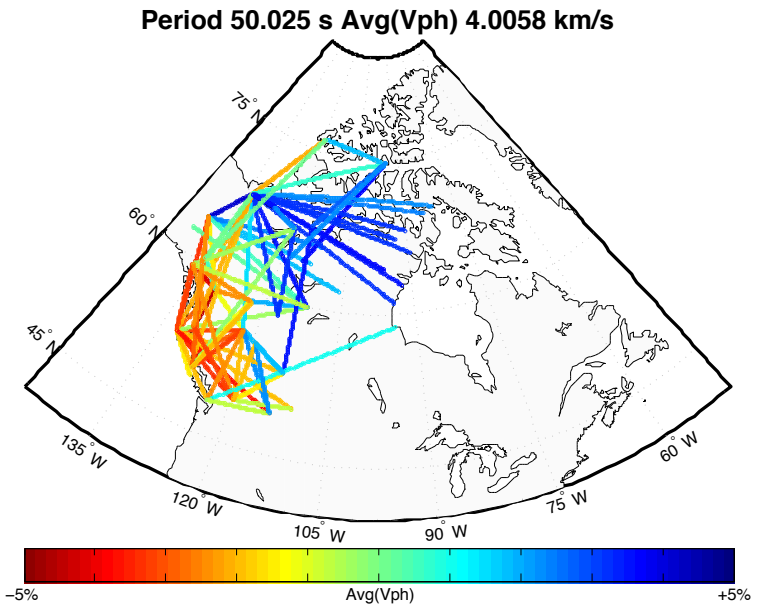

Figure 7.2: Visualization of individual path velocities on a map for a period of 50 seconds.

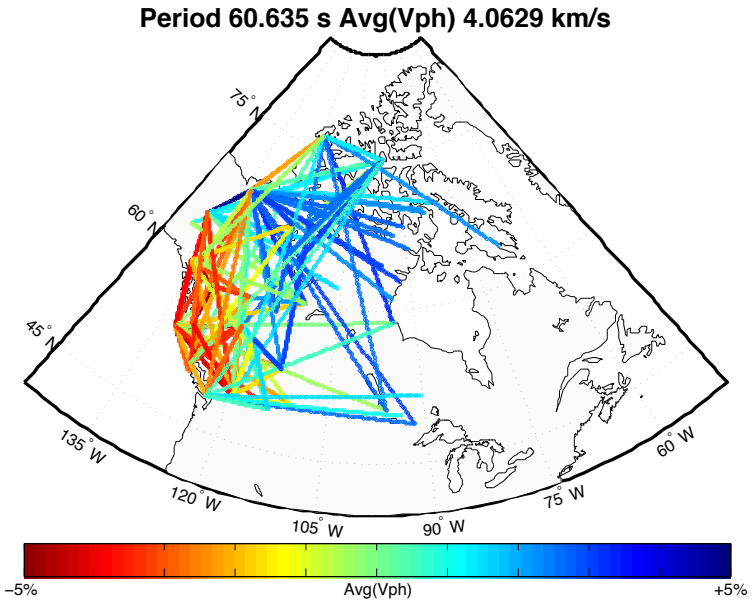

Figure 7.3: Visualization of individual path velocities on a map for a period of 60 seconds.

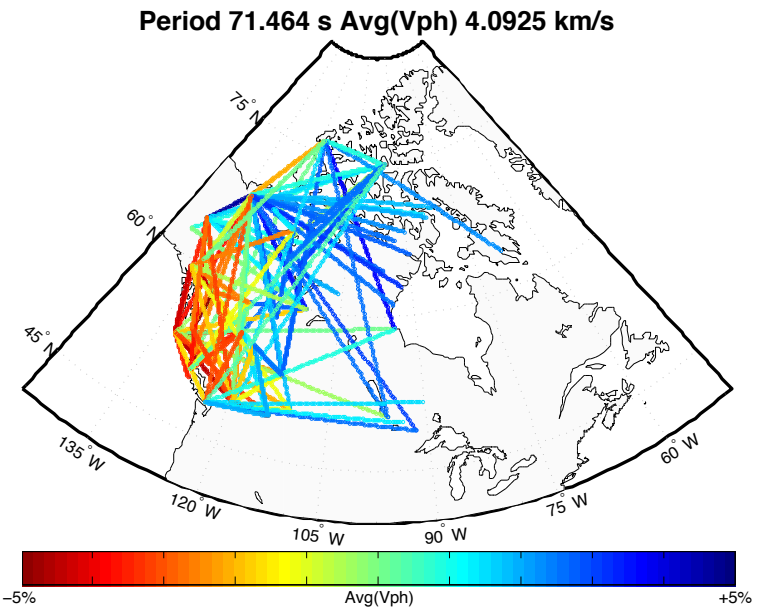

Figure 7.4: Visualization of individual path velocities on a map for a period of 71 seconds.

continental Cordillera all the way to the western edge of the study area. These decreases are in the range of 1-2% depending on location of the path. In the north and station paths strictly in the platform/craton the velocity perturbation remains positive and large, at 5%.

At 100 seconds (Figure 7.6) some slower western areas appear to show an increase in velocity, by 1-2%, but this may be due to higher velocity structures being sampled, to the north and east of the slower western velocities. Longer paths located to the north and east do not change noticeably.

At 125 (Figure 7.7) and 142 (Figure 7.8) seconds the velocity perturbation decreases towards 0%. Velocities trend towards this 0% in the west and middle of the study area while velocity paths along the edges of coverage tend to stay at the extremes of the range. Long path velocities decrease towards 0% more slowly.

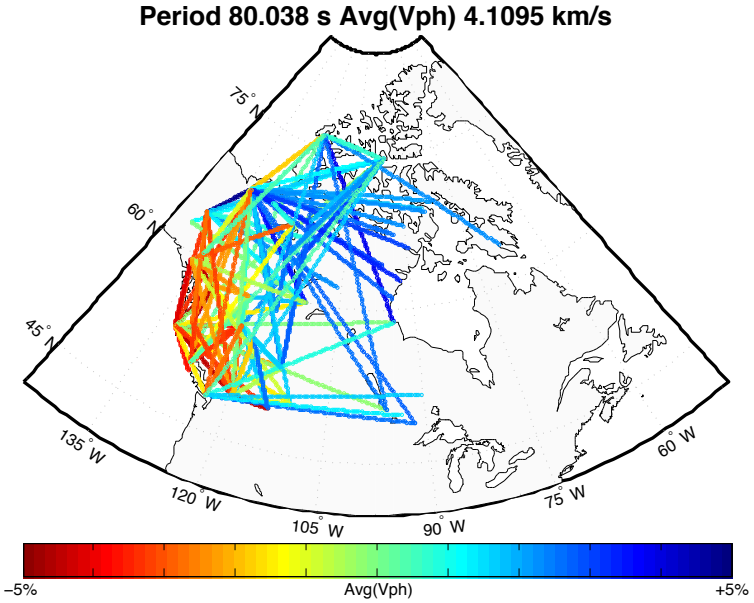

Figure 7.5: Visualization of individual path velocities on a map for a period of 80 seconds.

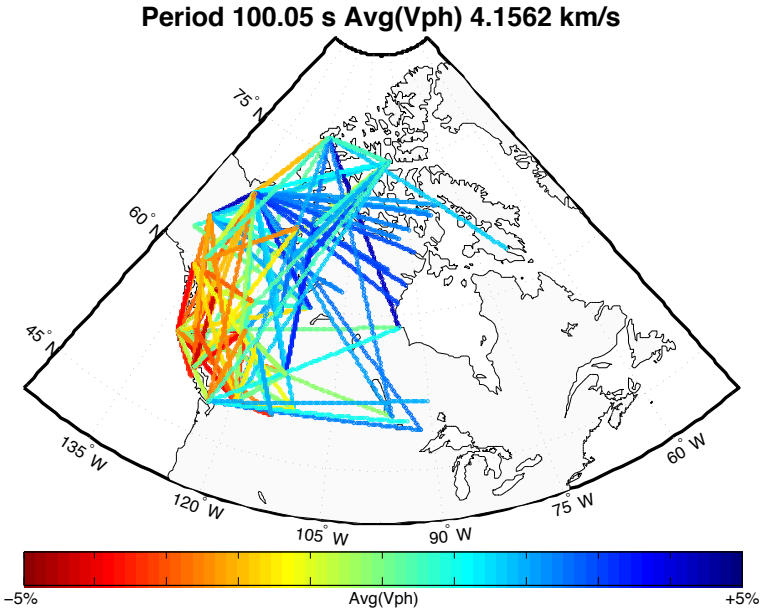

Figure 7.6: Visualization of individual path velocities on a map for a period of 100 seconds.

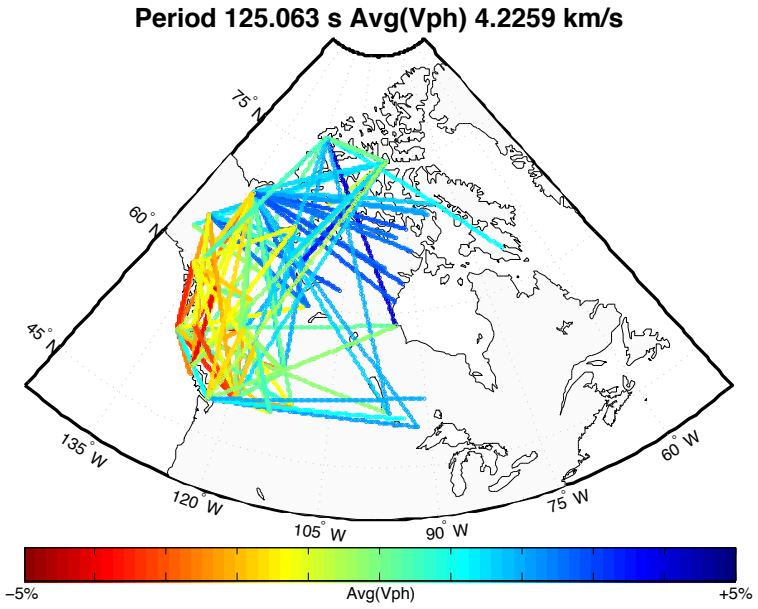

Figure 7.7: Visualization of individual path velocities on a map for a period of 125 seconds.

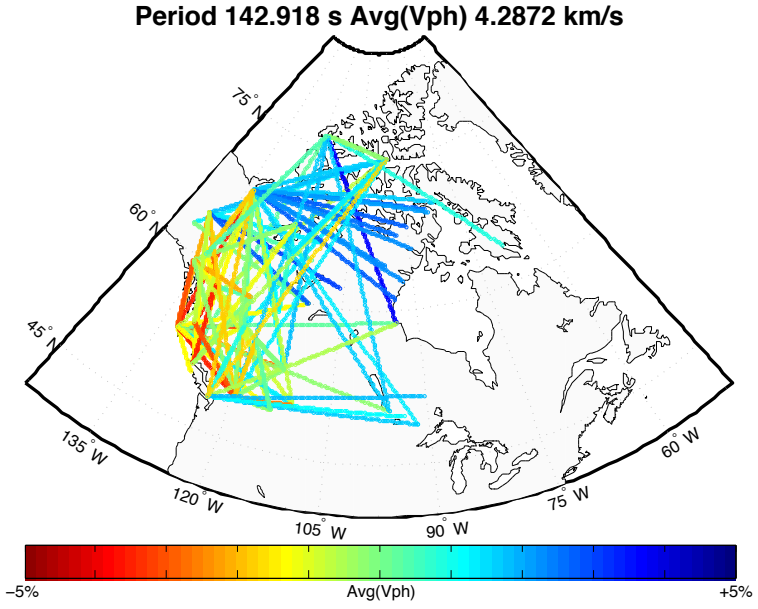

Figure 7.8: Visualization of individual path velocities on a map for a period of 142 seconds.

7.2 Tomographic images

Using the dispersion curves and the tomographic inversion method described in Chapter 5.2, tomographic maps were created. These tomographic images fill in the areas surrounding the paths in the path velocity maps and, more importantly, undo the path averaging that occurs along every path. These maps were plotted using the Generic Mapping Tools (GMT) software (Wessel et al., 2013). Major tectonic boundaries were also plotted to aid in relating velocity and geological features visually. These tectonic boundaries were taken from Hoffman (1988) and Ashton et al. (2009).

Map coverage at 30 seconds (Figure 7.9) is limited, as explained in section 7.1. Low velocities (3.7-3.8 km/s) are primarily located within the Cordillera with some seen in the southern Hearne. In the northern Cordillera, velocities are slightly higher at 3.8-3.9 km/s. In the Wopmay and Slave, velocities are, on average, 4.0 km/s. At 40 seconds, the overall Cordilleran velocity increases by 100 - 200 m/s with the middle of the continental Cordillera staying at 3.7 km/s. The edge of the slower velocities appears to line up with the Tintina fault more closely than at 30 seconds. Centred approximately on Great Bear Lake is a higher velocity zone that is 100 m/s faster than the same area at a period of 30 seconds.

For the 50 second period there is an overall increase in velocities of about 100 m/s (Figure 7.10). The low-velocity zone, in the north, extends across the Tintina fault to the northeast, but still maintains the same approximate boundary in the south. At this period, the low velocity boundary begins to follow the Cordilleran deformation front which is approximately parallel to the Tintina fault in the south but extends northeast in the north. Much of the Wopmay, Slave, Taltson, and Thelon provinces correspond to velocities of about 4.2 km/s. Coverage has increased in comparison to shorter periods but increases even more at 60 seconds. The Cordilleran margin of the low velocities no longer follows the Tintina fault but now appear to match the

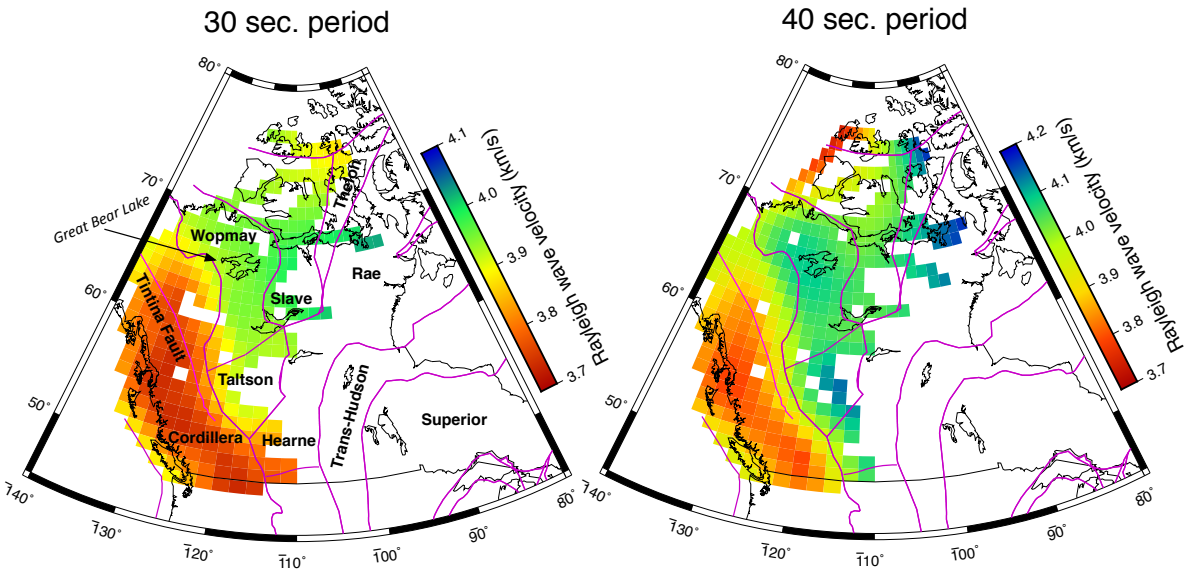

Figure 7.9: Tomographic image of western Canada at periods of 30 and 40 seconds. Lines in purple are of major tectonic boundaries of Canada and the approximate location of the Tintina fault in British Columbia. Unsampled grid cells are shown in white.

Cordilleran deformation front to the south. In the north the margin of the low velocities is still closely similar to the boundary at 60 seconds period. Velocities throughout the Wopmay, Slave, Taltson, Thelon, and parts of the Rae/Hearne provinces are 4.2 km/s with velocities of 4.1 km/s near the Cordilleran boundary. Parts of the Trans-Hudson and Superior provinces show slightly slower (4.15 km/s) and faster (4.4 km/s) velocities compared to the rest of the continental craton, respectively.

The low velocity zone at a period of 70 seconds has relatively the same spatial extent as 60 seconds, with a velocity of 3.8 km/s in the middle with slightly increasing velocities on the edges of the zone (Figure 7.11). Generally, the entire continental craton has a velocity of 4.2 km/s, which is a slight increase relative to the results of 60 seconds period. However, centred around Great Slave Lake, there is an anomalous 100 m/s increase in velocity. At a period of 80 seconds, the Cordilleran velocity is 3.9 - 4.0 km/s in the low-velocity area and 4.1 km/s along the Cordilleran deformation

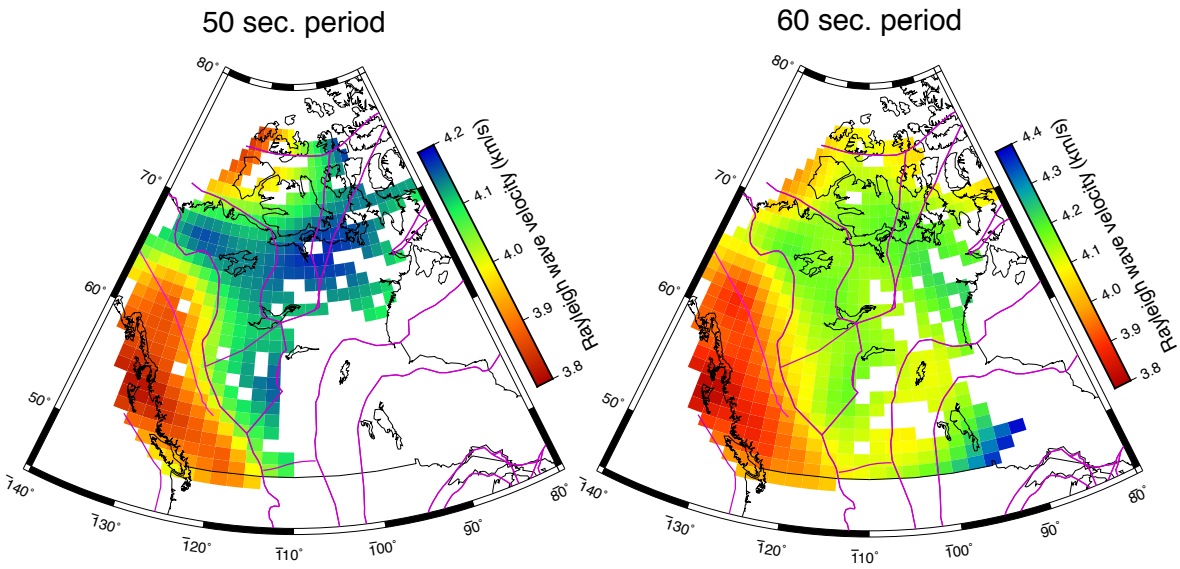

Figure 7.10: Tomographic image of western Canada at periods of 50 and 60 seconds.

front. From the Cordilleran deformation front into the craton the velocity remains in the range of 4.1 - 4.15 km/s, not including the Great Slave Lake anomaly and any results near the edge of coverage (velocities near 4.5 km/s). The high velocity anomaly centred around Great Slave Lake is still present and remains 100 m/s faster than the rest of the surrounding craton.

With an increase in period to 90 seconds (Figure 7.12), the majority of the Cordillera has a velocity of 4.0 km/s with areas of 4.15 km/s near the boundary and large areas closer to 3.9 km/s. In the southwest of the Taltson province, low velocity readings previously seen only in the Cordillera, begin to extend into the southern Taltson. The craton, as a whole, is approximately the same velocity as at 80 seconds (4.15 - 4.2 km/s) as is the Great Slave Lake anomaly (4.3 km/s). The average velocity of the Cordilleran low-velocity area increases by approximately 100 m/s to 4.0 km/s with the increased period.

Low velocities in the southern Canadian Cordillera extend into the Talston to a greater degree starting at 100 seconds. The low-velocity area present in the Taltson

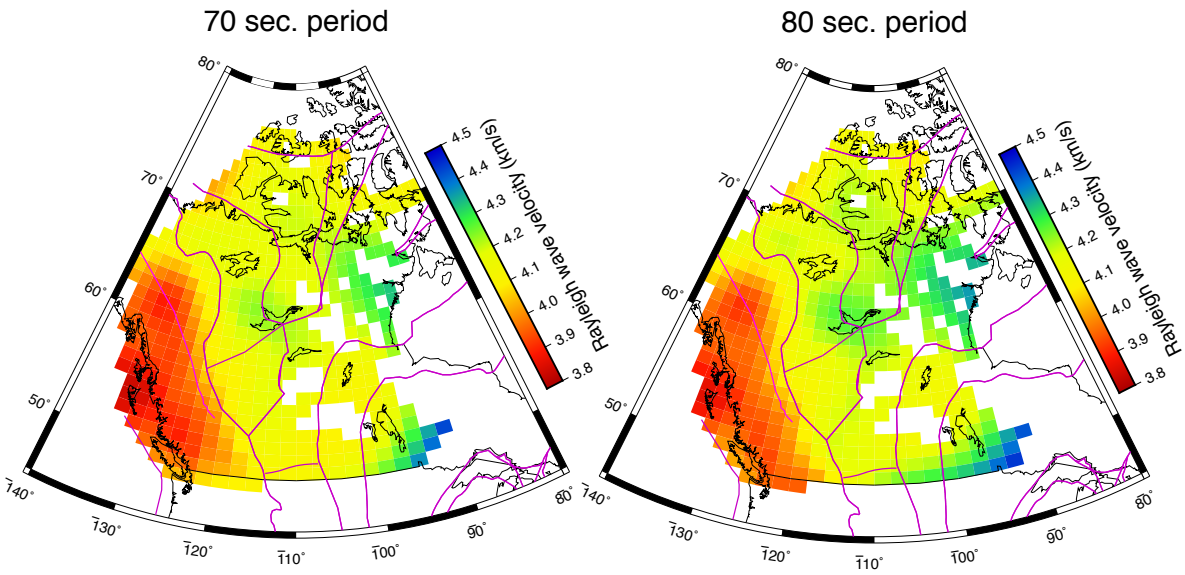

Figure 7.11: Tomographic image of western Canada at periods of 70 and 80 seconds.

increases in area with a velocity of 4.1 km/s. Cratonic velocities remain approximately the same as at 90 seconds at 4.2 km/s with eastern edge readings remaining at 4.5 km/s. The Great Slave Lake anomaly remains 100 m/s faster than the surrounding continental velocity at 4.4 km/s.

The average velocity of the Cordillera at 110 seconds is 4.1 km/s, which is an increase from the previous period (Figure 7.13). Two large slower areas (centred at 60° and 55°) still remain 100 m/s slower than the rest of the Cordillera. Boundary velocities are the same throughout the Wopmay and Talston and are similar to parts of the Hearne and Trans-Hudson provinces. Cratonic velocities remain near 4.2 km/s which is only slightly faster than the Cordillera. The Great Slave Lake anomaly is sharply contrasted against its surroundings with a velocity of 4.4 km/s which is approximately 200 m/s faster than surrounding areas. A low velocity zone is now present in the Trans-Hudson orogen with a velocity of 4.15 km/s. The Cordillera has a slight increase in average velocity to 4.15 km/s. Low velocities remain across the Wopmay Talston, Hearne, and Trans-Hudson orogens between 50° and 60° latitude

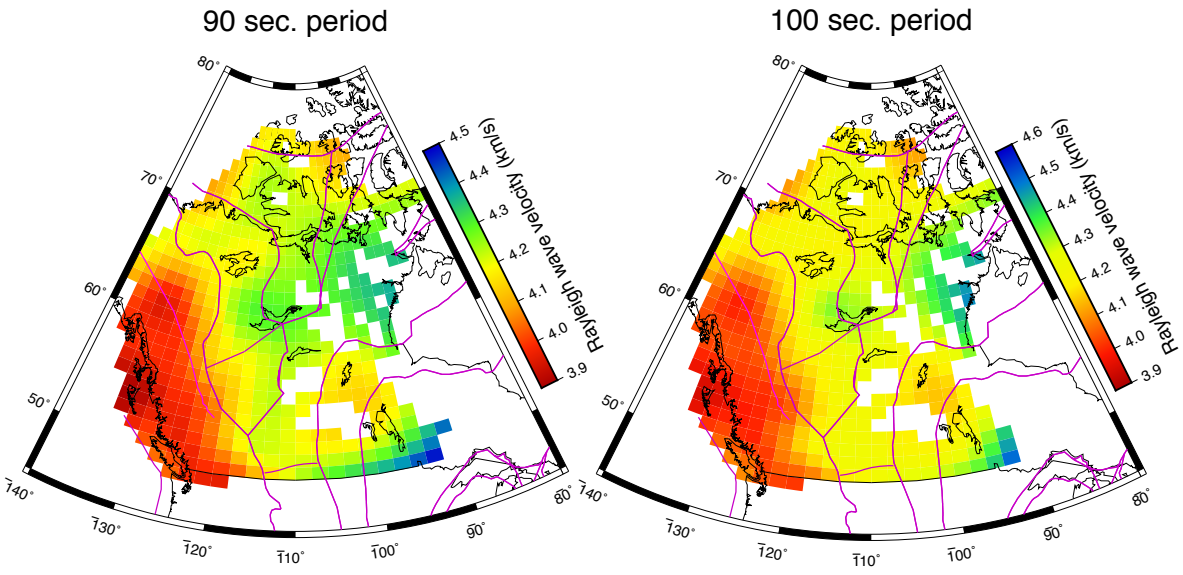

Figure 7.12: Tomographic image of western Canada at periods of 90 and 100 seconds.

with a velocity of 4.2 km/s. Velocities in the Wopmay increase by about 50 m/s to 4.25 km/s, with the change from a period of 110 to 120 seconds. The Great Slave Lake anomaly maintains the same velocity at 4.4 km/s.

The Cordillera and continental (between 50° and 60° latitude) velocities increase by 50 m/s to 4.2 km/s and 4.25 km/s respectively (Figure 7.14) at 130 seconds. Velocities at the margin of the Cordillera are increased compared to the central values of the Cordillera thereby shrinking the area of lower velocity at 130 seconds and and even more at 140 seconds. The lower velocity area throughout the Taltson remains at 4.2 km/s. Velocities in the Wopmay and Slave are 4.35 km/s and 4.4 km/s respectively, which is an increase of 50 m/s in each area. Areas in the eastern Hearne/Rae and Superior provinces maintain the 4.5 km/s velocity observed at 120 seconds period.

At 140 seconds period the increasing velocity at the margins of the Cordillera continues with values increasing another 50 m/s. The shape of the low velocity area (4.2 km/s) does not resemble the boundary of the Cordillera at all as it remains in the Taltson province. Higher-velocity readings appear to the south of the image

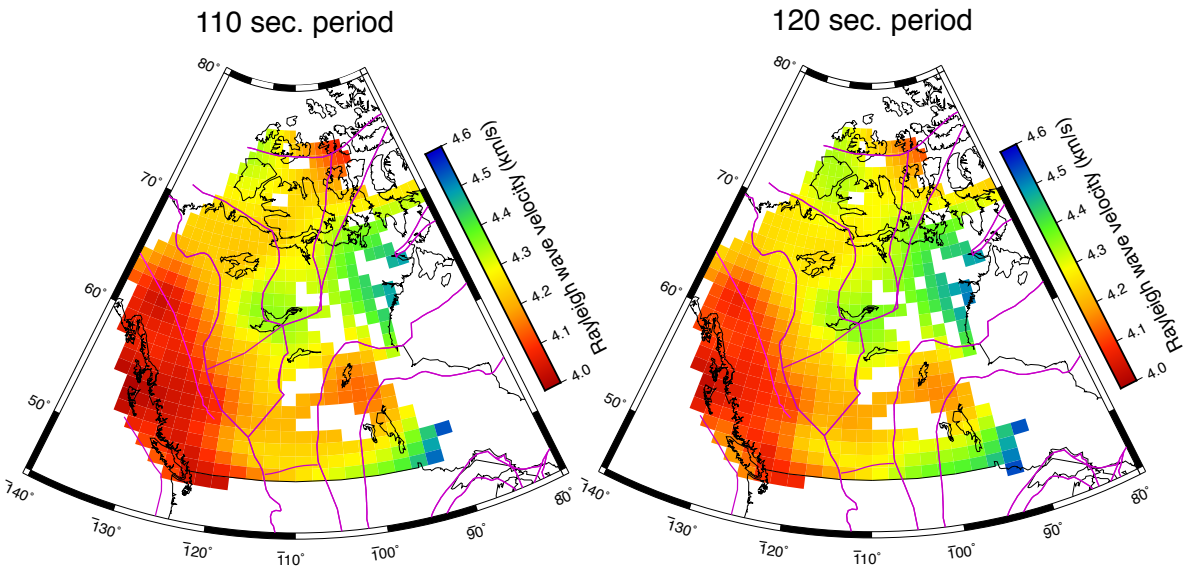

Figure 7.13: Tomographic image of western Canada at periods of 110 and 120 seconds.

across the Superior, Trans-Hudson, Hearne/Rae provinces and into the Cordillera (4.4 km/s). The Great Slave Lake anomaly now extends from the Slave craton and Wopmay orogen into the Rae/Hearne province (4.5 km/s).

Figure 7.15 velocities of 150 and 160 seconds exhibit the same pattern as at 140 seconds. Cordilleran and Taltson velocities range from 4.25 km/s to 4.3 km/s. The Wopmay and southern Slave range from 4.35 km/s to 4.4 km/s. The southern portion of the study area shows velocities of 4.5 km/s with areas reaching 4.6 km/s in places. The Great Slave lake anomaly has a velocity of 4.45 km/s at a period of 150 seconds and 4.55 km/s at 160 seconds and is now centred along the Slave and Rae/Hearne southern boundary. At 150 and especially 160 seconds the centres of the two Cordilleran low velocity zones first noted at 60 seconds period are easily seen, with values 100 m/s slower than the surrounding velocities. At periods longer than 140 seconds the coverage is poor since small features are not all that well resolved and some along-path streaking is now visible.

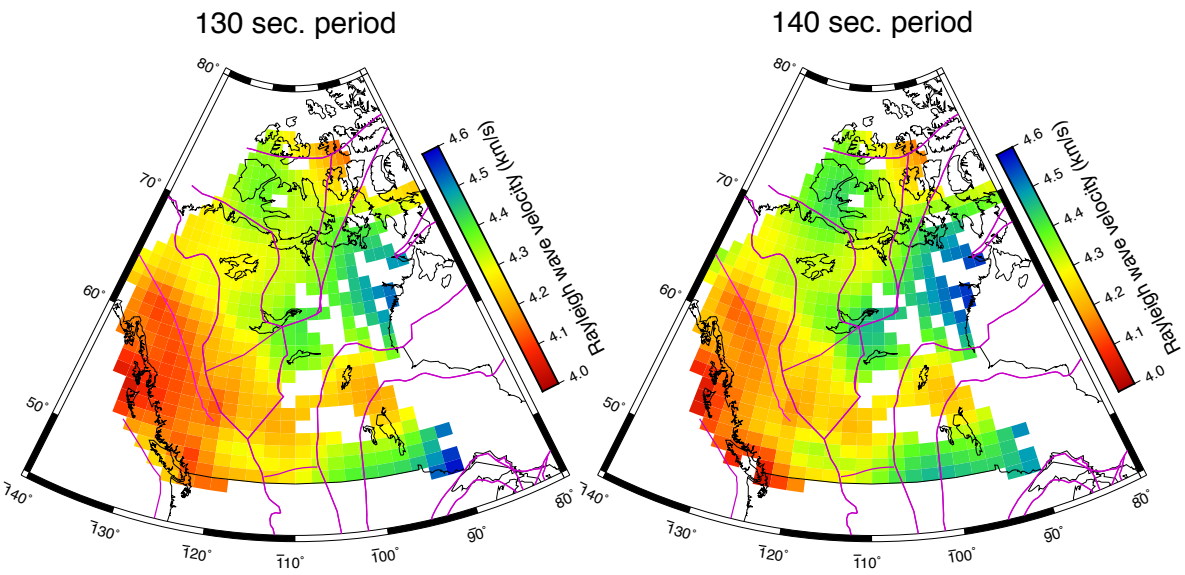

Figure 7.14: Tomographic image of western Canada at periods of 130 and 140 seconds.

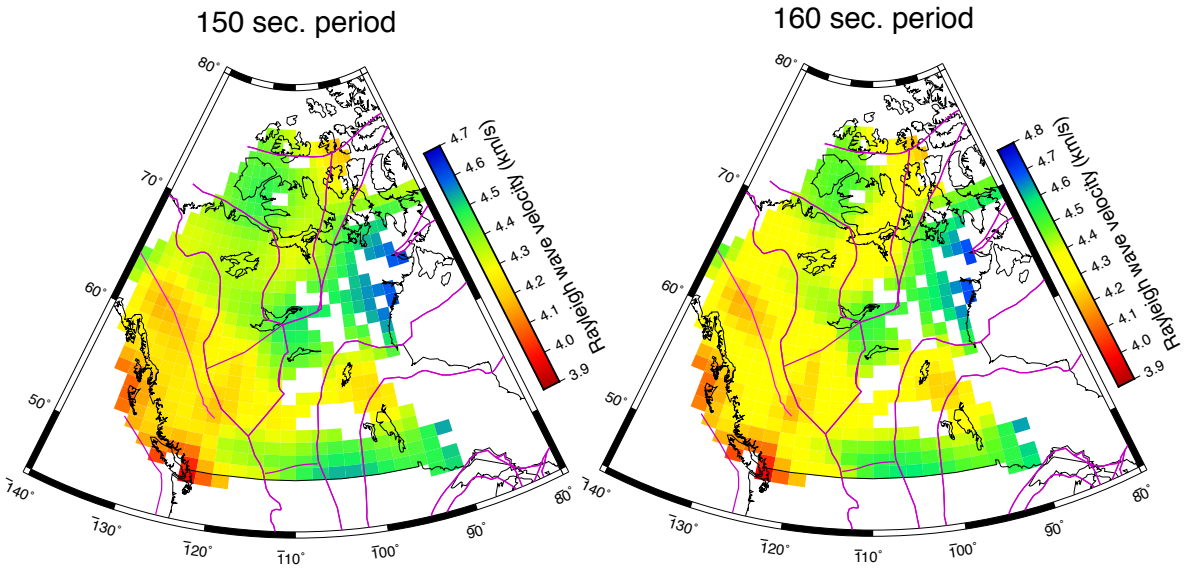

Figure 7.15: Tomographic image of western Canada at periods of 150 and 160 seconds.

7.3 Summary

For most of the periods sampled (30-140 seconds), the Cordillera has a relative velocity 200-300 m/s slower than the craton average. The margin of this slow velocity zone generally matches the Cordillera Deformation Front, but at periods of 110-130 seconds, possibly due to effects of smoothing, the low velocity crosses the Cordillera deformation front into the Taltson. At 150 seconds the velocity difference between Cordillera and craton (not including the Taltson) decreases to 100 m/s, and at 160 seconds the Cordilleran and cratonic velocities become similar.

An anomaly located near Great Slave Lake first appears at a period of 70 seconds and persists until the longest period of 160 seconds. This high velocity zone is located primarily along the Wopmay/Slave boundary but does appear in further into the Slave and Hearne provinces as well at different periods (80-90, 110-160 seconds). The velocity of this anomaly is 50-150 m/s greater than the velocity in the surrounding area.

Chapter 8

Pseudosections and cross-sections

8.1 Procedures

In the previous chapter, tomographic inversion was used to convert path measurements of dispersion curves into 2-D maps of spatial variation of phase velocity. In this chapter, those dispersion maps will be used to examine variation in velocity with depth.

The tomographic images described in the previous chapter were used to create psuedosections. Pseudosections are variations in phase velocity along profiles across the map, plotted with period as a depth proxy. These pseudosections were created along eight profiles. The start and end locations of the profiles are listed in Table 5.1. These profiles are plotted in Figure 5.9 with added political boundaries and coastlines. For each profile a spacing of 50 km was used at which depth inversions were completed to provide a good resolution cross-section for looking at large features in the upper mantle.

Figure 8.1 shows 1-D inversions at 300 km and 1000 km points along profile B, with the left panel being located within the Canadian Cordillera and the right being within the craton/platform. Data from the craton appears noisier, with larger error

bars (determined from the standard deviation of the Cordillera and craton arithmetic dispersion curve averages), compared to the Cordillera. Both sets of inversions shown in Figure 8.1 fit the data well. Since the 22 layer model was parameterized to allow a gradual change of the subsurface velocities, the velocity of a layer (for example 10) may be similar to the velocity of the overlying and underlying layers (layer 9 and 11). Above 258 km depth all velocities are lower than the base model for the Cordillera. The opposite is true for the craton, which has higher inverted velocities down to a depth of 300 km. Below 300 km, the cratonic velocities remain the same as the base model, but the Cordilleran velocities are all greater than the base model. Using this process, numerous 1-D inversions were completed along each profile to create a cross-section of each profile.

Standard errors for all inversions range in value from 0.0781 to 0.6481 km/s. Examples of the degree of model fit can be seen in Figure 8.2 showing poor, intermediate, and good data fit. The wide range of standard error shows that this parameter is helpful but not necessarily an accurate measurement of the fit quality. Across some profiles trends in the misfit are present at short or long periods. Shorter period observed responses are usually higher than the model responses, while longer period observed responses are lower than the model responses. These misfit trends may be due to the fact that the data were obtained from tomographic images. Smoothing of station pair path values could smear unrepresentative velocities to neighbouring areas. This results in smearing of higher (for shorter period) and lower (for longer period) velocity values. These trends are consistent near the edges of coverage, in areas with poor coverage, and near feature transitions.

Figure 8.3 shows the pseudosection for profile A in the top panel, percent variation from the base model in the middle panel, and the absolute velocity in the bottom panel. It is difficult to determine depth and velocity using pseudosections. Inversion of the pseudosection creates cross-sections which provide a sharper image by

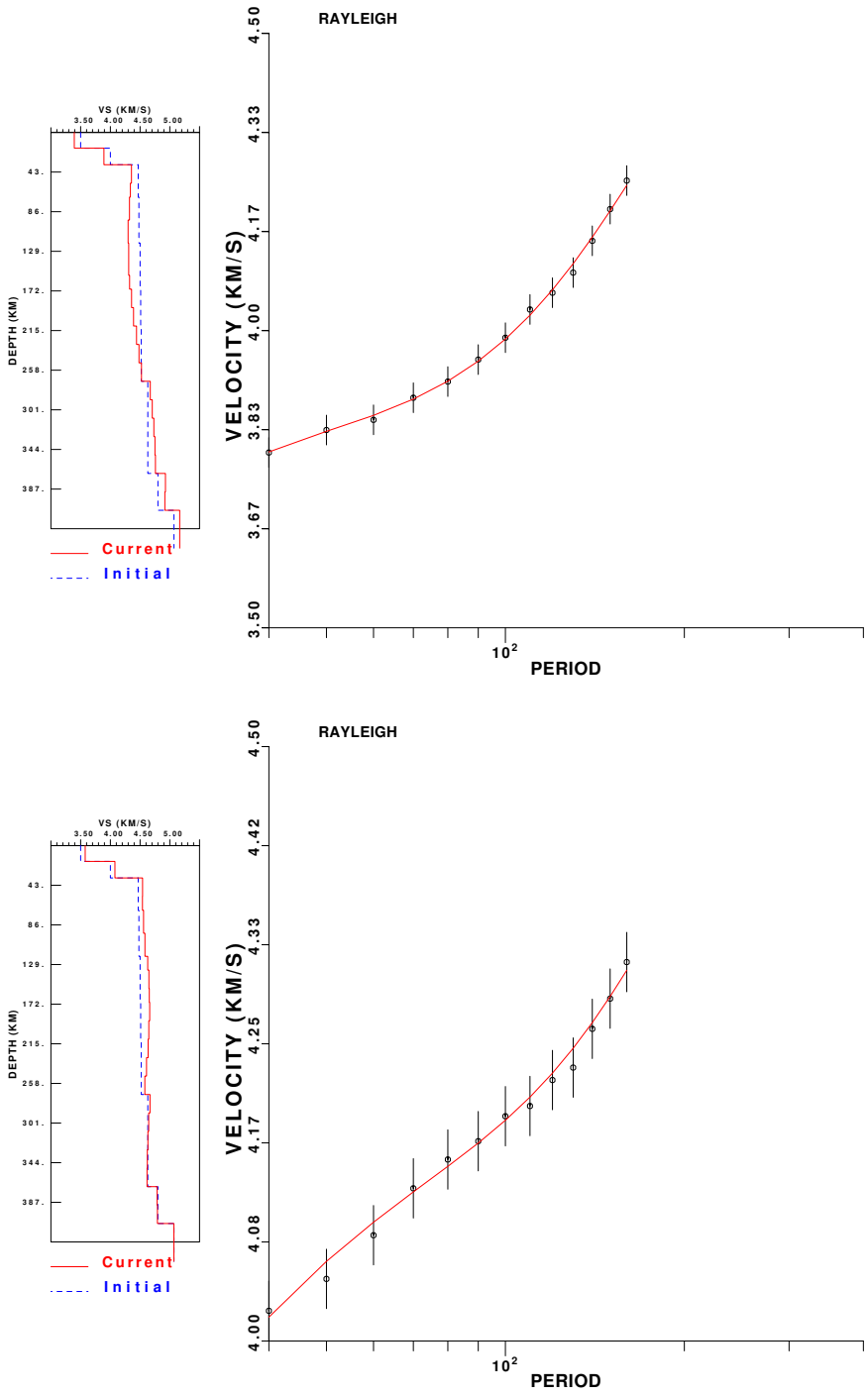

Figure 8.1: Plots of the Cordillera, at 300 km along the profile, (top) and craton, at 1000 km along the profile, (bottom) depth inversions along profile B. The red curve shows the inverted model and the black points and lines correspond to the data points and standard deviation of each measurement, respectively. Error bars are 0.05 km/s which was approximated from the standard deviation of the calculated eastern and western dispersion curves.

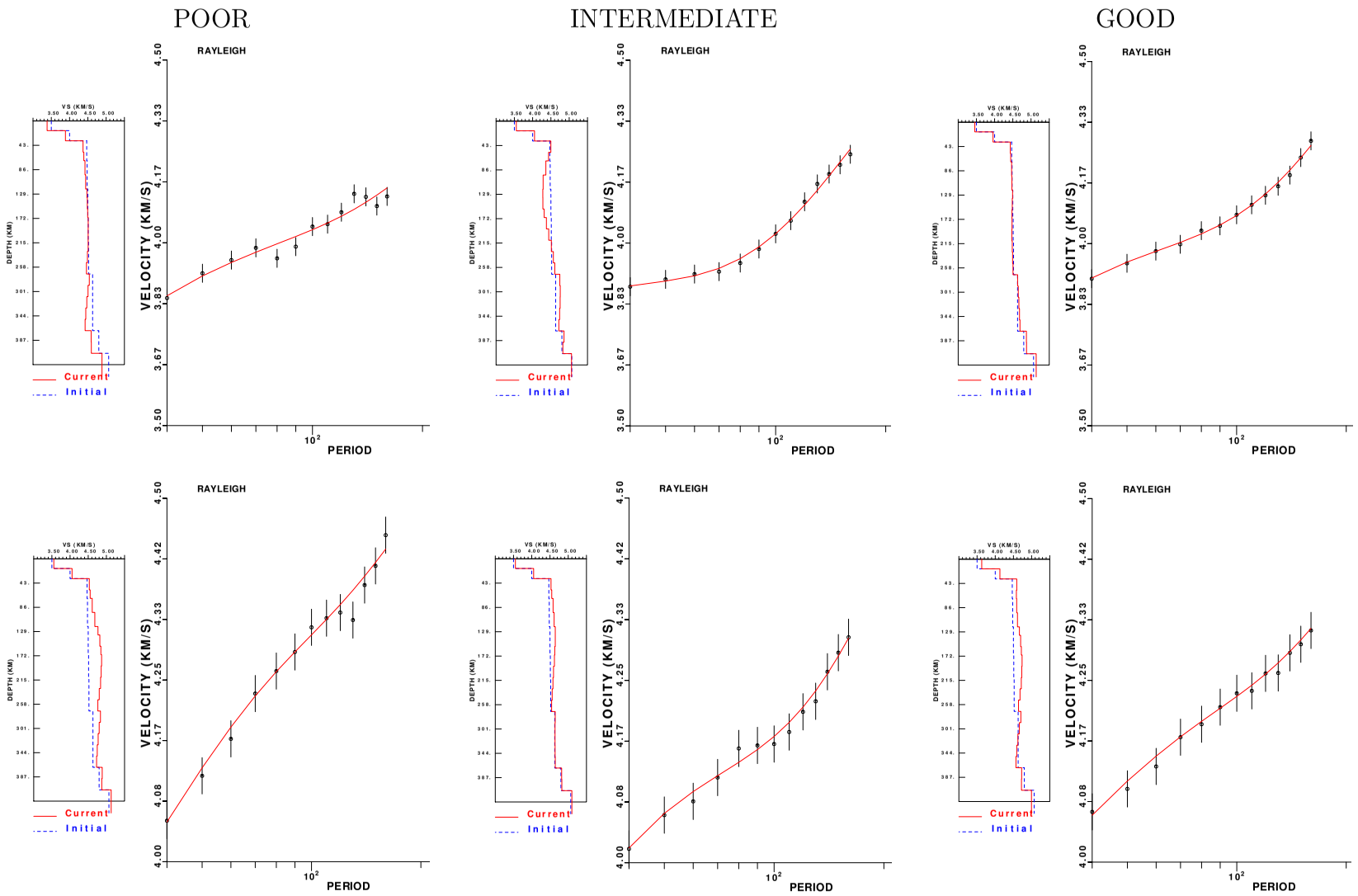

Figure 8.2: Examples of poor (left column), okay (centre column), and good (right column) 1-D inversion data fit for Cordillera (top) and craton (bottom) results. Standard error for each plot, clockwise from the top left, is 0.3317, 0.2068, 0.0974, 0.0887, 0.2387, and 0.5474 with units of km/s.

eliminating this vertical averaging. Similarly, the percent variation, relative to the starting model, will be discussed in more depth due to lateral contrasts being more visible in each figure in comparison to the absolute velocity cross-section. Features of significance were labeled A through H in each pseudosection. These features are labelled consistently across profiles A, B, C, D, L, S, X, and Y.

Profile A shows a slow velocity perturbation (feature labelled "A" in Figure 8.4) relative to the base model extending from 300 km - 800 km, horizontally, with a variation of -3% to -5%. This zone extends from the surface down to a depth of 250 km southwest of the 800 km point along the profile. It appears to dip down to 400 km with increasing distance northeast along the profile with a variation of only -2% (B). More shallow results show slightly faster velocity variation (1%) to a depth of 100 km (C). There are two areas in the image with a fast velocity anomaly. The first (D) is centred on 600 km along the profile at a depth of 375 km and has a variation from 4% to 7%. The second (E) is centred at a depth of 200 km, starts at 1200 km along the profile is and extends to the end of the profile with a velocity variation ranging from 4% to 9%. Between features (E) and (A) (and feature (B) at greater depth) is a distinct transition zone (H). This feature starts at 700 km along the profile at a depth of 100 km and dips to the northeast to a depth of 300 km. Moving northeast from 2200 km along the profile a sharp velocity increase from 1% to 5% (F) occurs less than 100 km depth. As well, the fast velocity area (E) begins to dip down to 400 km gradually.

The absolute velocity plot shows a background velocity of 4.6 km/s. At depths of 50 km to 250 km, a slow lithosphere in the southwest is present with values of 4.3 km/s. Below this (at about 400 km depth) a fast zone is present with velocities reaching 5.2 km/s. Another fast velocity zone is less defined further along the profile at at depths ranging from 100 km to 400 km with velocities of about 4.9 km/s.

Profile B (Figure 8.4) shows a very similar end of profile (NE) since profiles 1 and

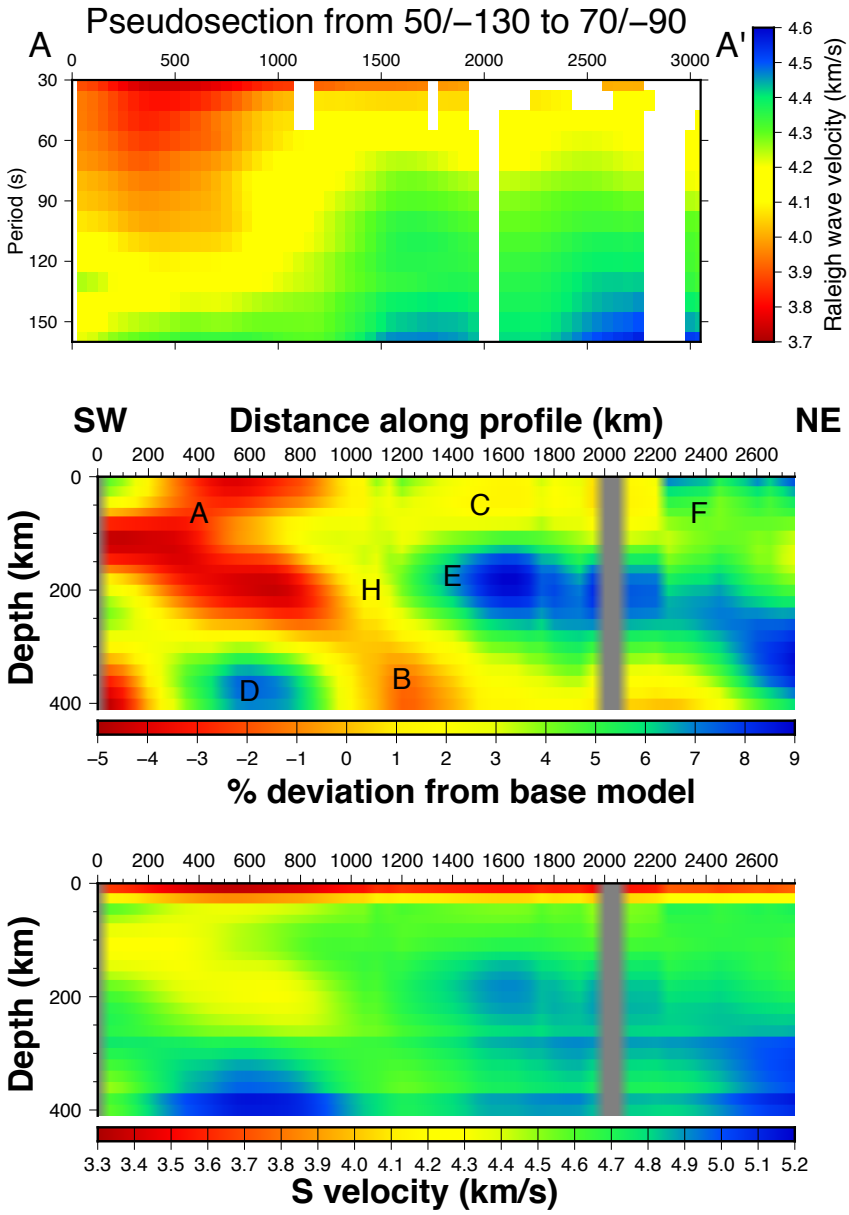

Figure 8.3: Profile A: Pseudosection (top panel) and cross-sections (middle and lower panels) across the southern Cordillera. White cells in the pseudosection indicate no station coverage at that cell. Grey lines in both cross-sections are a result of a lack of sampling in the corresponding dispersion-map cells.

2 are similar in their paths. The start of the profile (53°N, -133°W) shows a slow velocity area from positions 200 km to 800 km extending from the surface down to a depth of 250 km (A). Variations are −3% to −5%. Dipping (B) and shallow (C) zero perturbation velocity zones are visible. The fast velocity area centred on 500 km along the profile at 375 km depth has values of 4% to 7% (D). The fast velocity zone from 900 km to 2700 km, at 200 km depth (E), has a 7% to 10% positive velocity perturbation. A shallow feature (F) has a velocity variation of 5%. The transitional zone (H) between positive and negative velocity perturbations is still evident.

Profile C (Figure 8.5) differs slightly from profiles A and B. A slow velocity zone (A) extends from 0 to 600 km along the profile at depth 140 km with a thickness of 100 km. Starting at 1000 km, at a depth of 100 km, until 2000 km, at an increased depth of 150 km, is a fast velocity area (E) of thickness 125 km and velocity variation of 6% - 7%. Feature (H) is narrower due the closer proximity between features (A) and (E) compared to those in profiles A and B. At 1550 km, along the profile, an odd feature divides feature E into two parts. This feature is believed to be an artefact resulting from a lack of frequencies sampled, as seen in Figure 8.5 (top) at the same spot along the profile. An upward shift in values is also seen on the absolute velocity cross-section (Figure 8.5 bottom). Below feature E is a separate fast velocity area (D) centred at 1700 km along the line, at a depth of 350 km with a width of 800 km and thickness of 150 km. Similar features at this depth are identified centred at 750 and 50 km along the profile.

Figure 8.6 shows the results of the inversion of profile D which is located in the northern Cordillera and ends in the southern Cordillera. Lower percentage velocity variations are seen throughout the figure with two major slow features centred on 600 km, at depth 125 km (A), and at the southeast end of the profile, at 0 - 100 km depth, with variations of −3% to −6% each. Resolution of shallow features is poor (discussed in greater detail later on in chapter 9.1) so the low-velocity area at

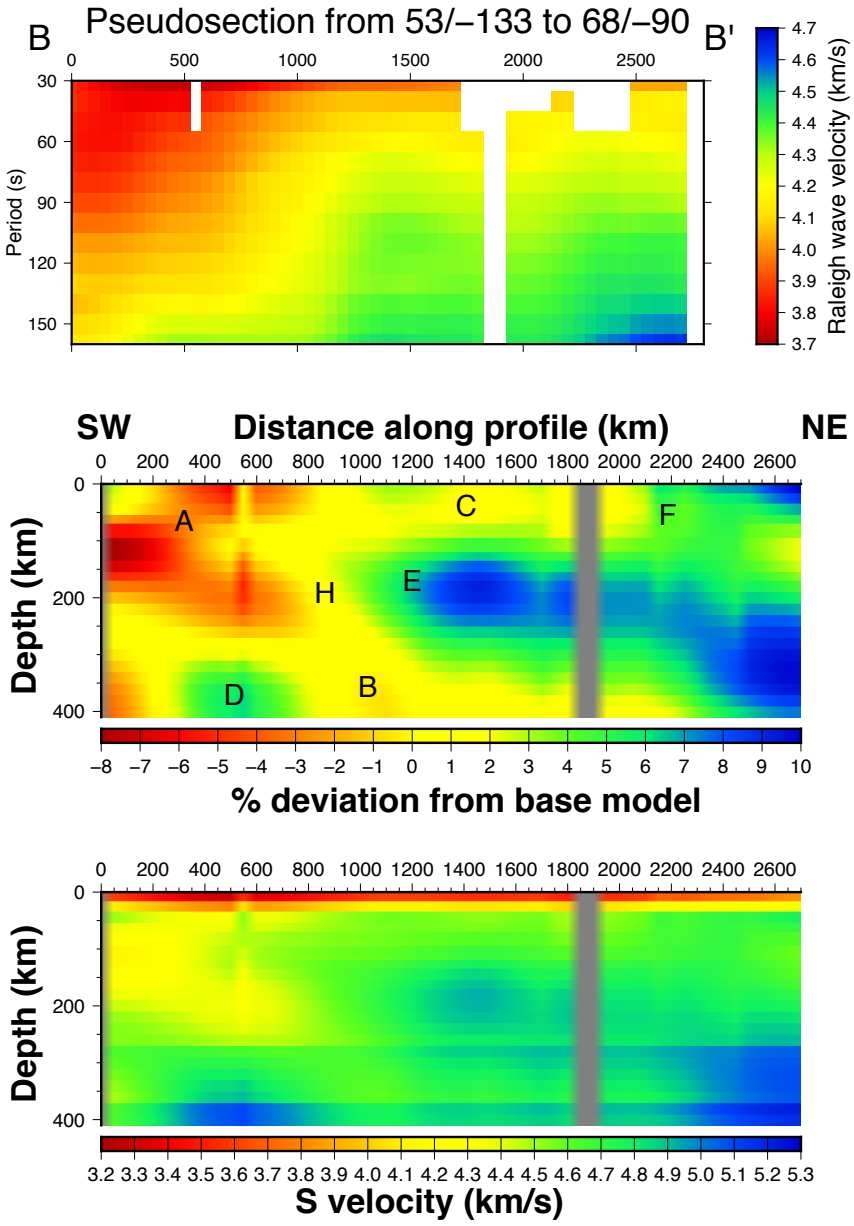

Figure 8.4: Profile B: Pseudosection (top panel) and cross-sections (middle and lower panels) across the mid-Canadian Cordillera

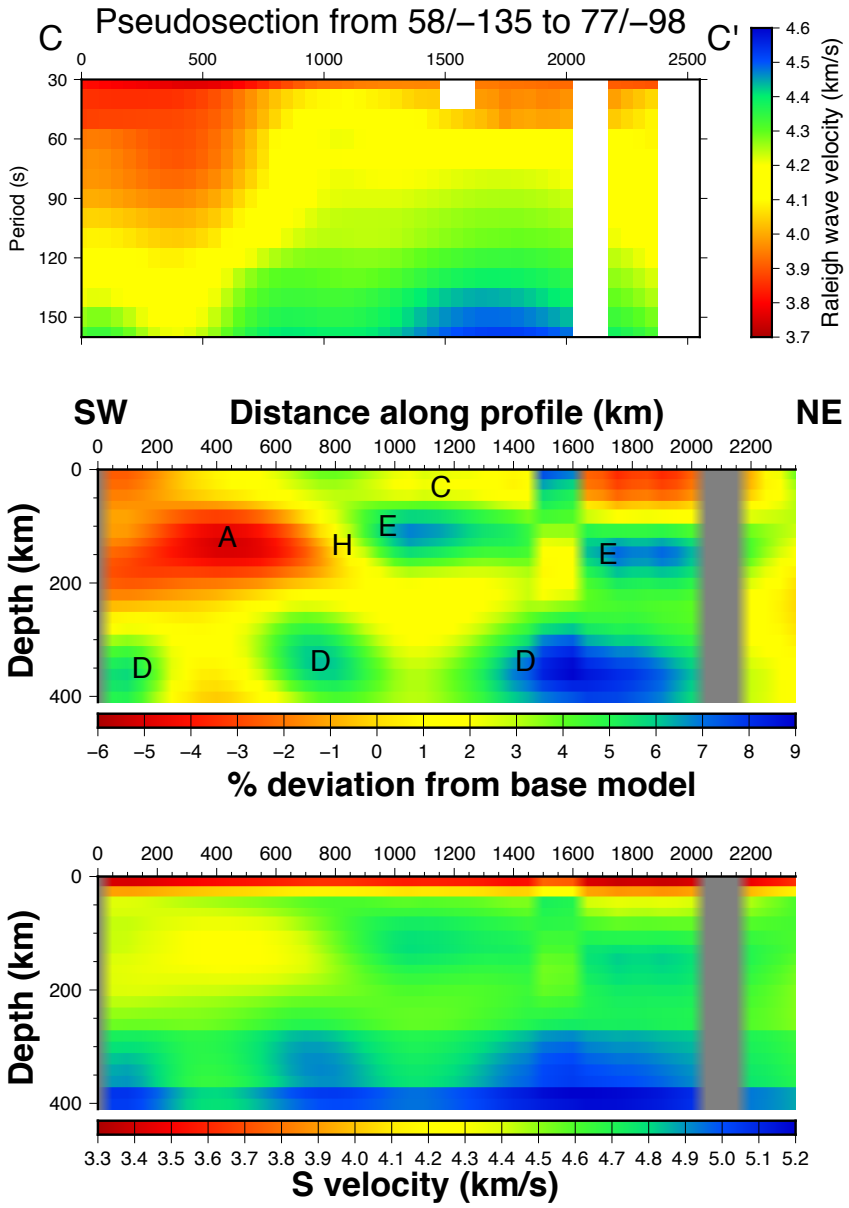

Figure 8.5: Profile C: Pseudosection (top panel) and cross-sections (middle and lower panels) across the northern Canadian Cordillera

the end of the profile will not be interpreted further. A low velocity area, possibly connected with the area centred on 600 km, has a variation of −2% to −4% that arcs and plateaus at 200 km depth and then dips southeast and sharply downward to 410 km centred at 1700 km along the profile (G). A low-velocity anomaly with lower variation (G) dips northwest downward to the 410 km. As seen from the previous profiles, high-velocity perturbations at 350 km (D) occur of 400 km depth.

Profile L (Figure 8.7) shows the absolute velocity (bottom) and velocity variation (top) for an west/east profile bisecting Great Slave Lake. Much of the profile is 3% greater than the IASP91 reference values with a slow velocity anomaly in the west and fast velocity anomaly in the centre and east of the profile. The slow velocity anomaly (A), in the west (0 km), is centred on 50 km at a depth of 150 km with a variation of −3% to −4%. Centred on 725 km at a depth of 175 km is a fast velocity area (E) with a 2% higher than background anomaly from 450 km - 1050 km. The centre of this feature has a 5% - 8% higher velocity variation than background over a 250 km lateral extent.

Figure 8.8 shows the absolute velocity (bottom) and velocity variation (middle) for a north/south profile bisecting Great Slave Lake. The velocity variation shows a bullseye-like feature with a high velocity anomaly of 8-10 % (E) centred at 500 km along the transect at a depth of 175 km. This anomaly has a width of 350 km. Adjacent to this anomaly and above and below it is a slower velocity variation of 6-7% with width of 100 km. A velocity gradient of the anomaly decreases above and below the anomaly. IASP91 reference values are seen in the upper 50 km of the north half of the profile and at depths exceeding 300 km.

Figure 8.9 shows a cross-section XX' along the same profile as one used in Miller and Eaton (2010). Zero perturbation velocities are present from 200 km to 800 km with slower velocities being seen in red dipping southeast towards 0 km to a depth of 150 km (A) with values of −3% to −5%. Higher velocity anomalies form a dome

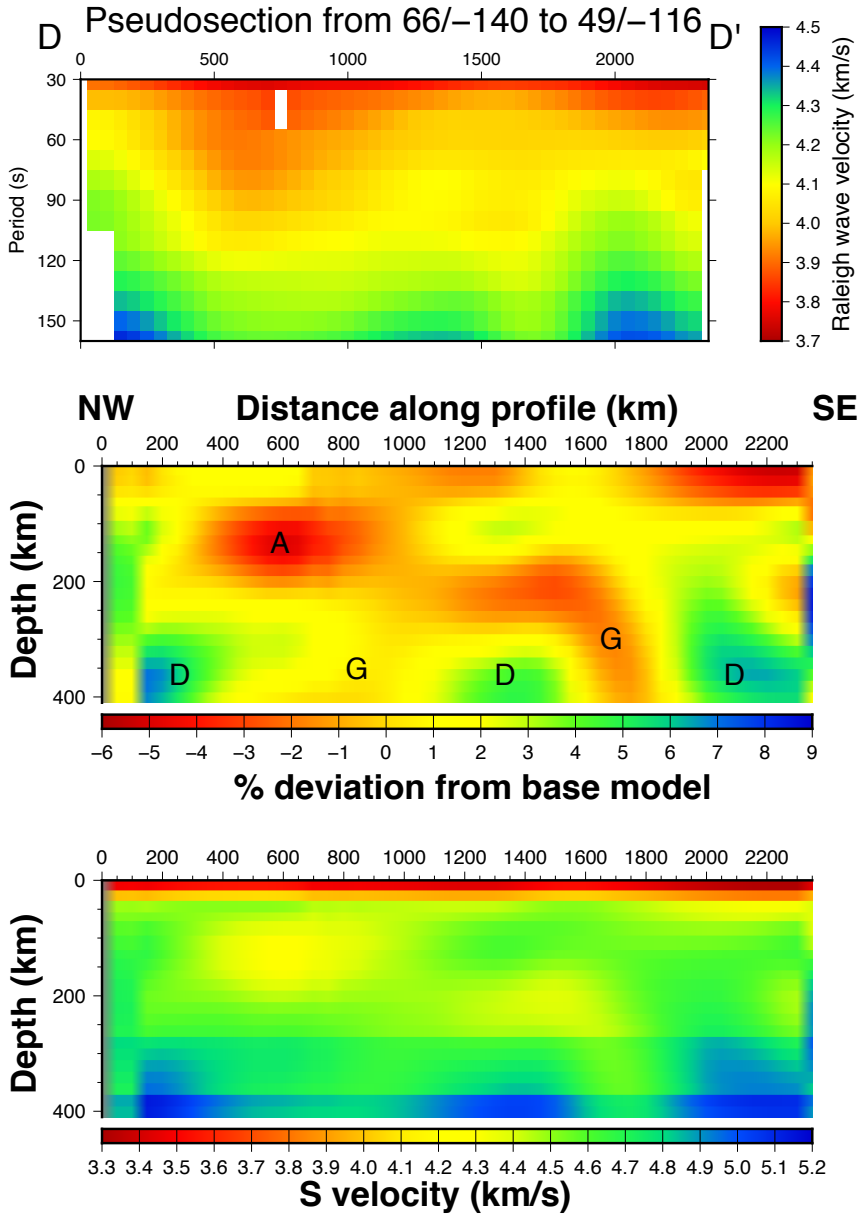

Figure 8.6: Profile D: Pseudosection (top panel) and cross-sections (middle and lower panels) along the Tintina fault.

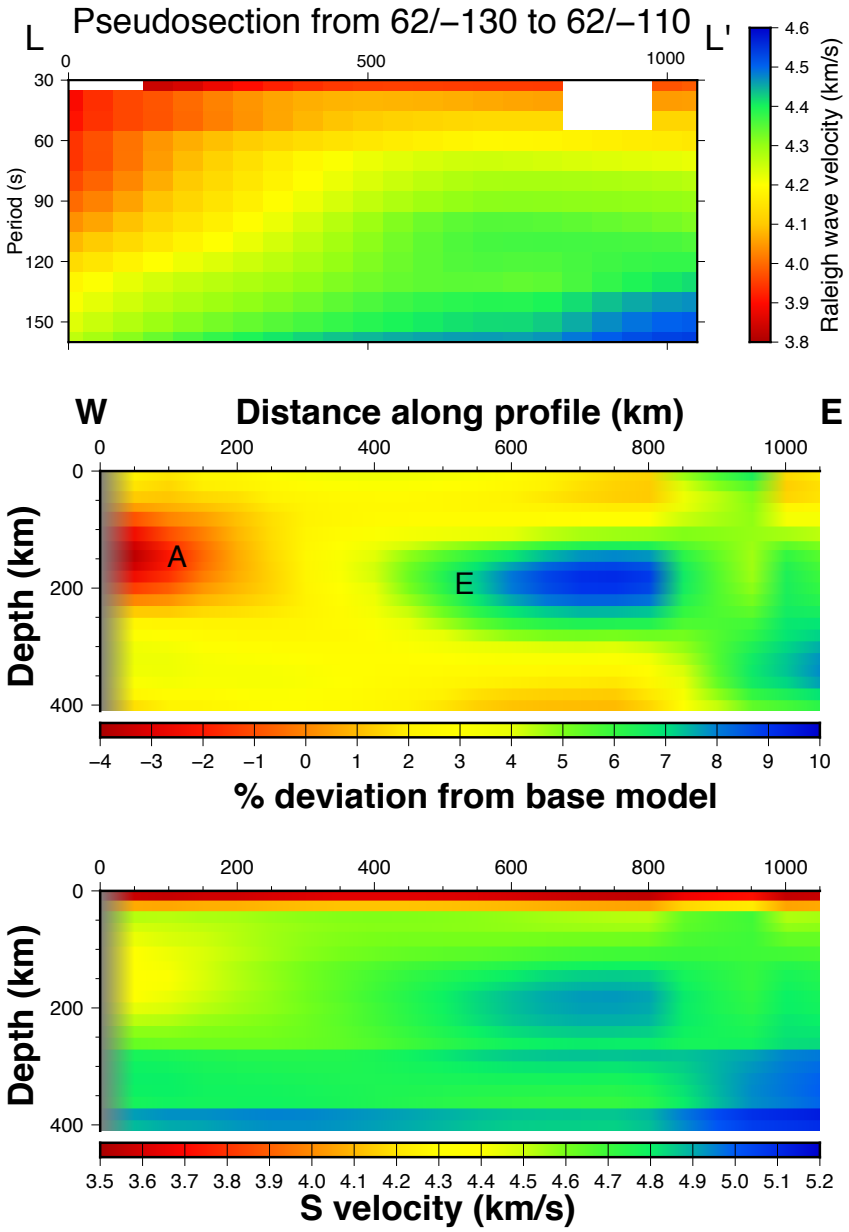

Figure 8.7: Profile L: Pseudosection (top panel) and cross-sections (middle and lower panels) bisecting the Great Slave Lake in the west/east orientation.

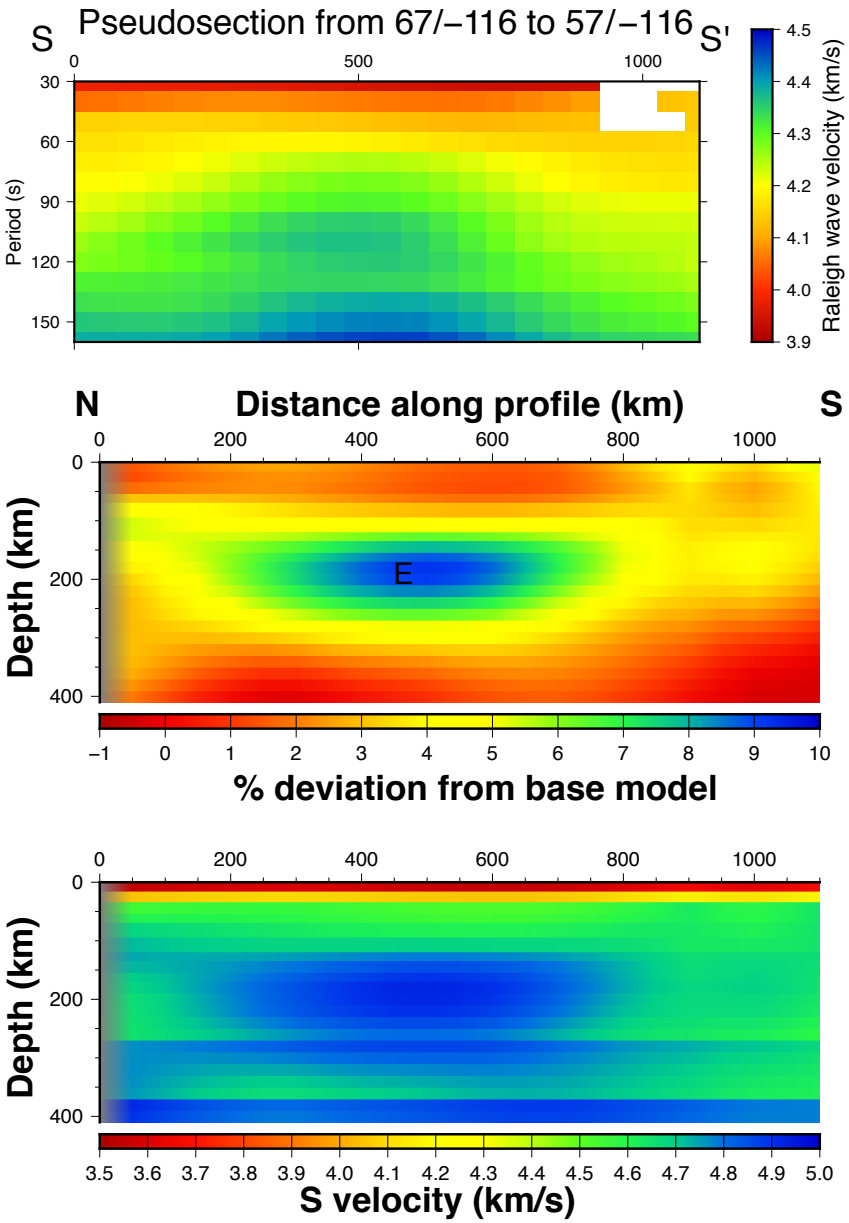

Figure 8.8: Profile S: Pseudosection (top panel) and cross-sections (middle and lower panels) bisecting the Great Slave Lake in the north / south orientation.

shape over a region of background velocity in the centre (B) of the profile at depths below 200 km. High-velocity perturbations (D) dip southwest to depths of 400 km starting 600 km along the profile until 400 km. At 1000 km on the profile, the velocity at depths above 200 km is mainly 3% greater than the base model (features E and F).

Profile Y (Figure 8.10) is based on the transect used by Bao *et al.* (2014) and is located along a portion of the longer Miller and Eaton (2010) profile. It has a horizontal higher velocity layer of 3% at 500 km to 1000 km along the transect (E). The thickness of the layer is 150 km with the top at 75 km. The layer includes a faster inner layer with a velocity variation of 8%, thickness 75 km, and with the top of the layer being at a depth of 100 km. The main high velocity layer (E) dips southwest at 550 km along the transect up until about 200 km where it descends to a depth of 350 km (D). An area of greater velocity variation with values ranging from 5% to 8% is observed at 350 km depth.

Below the horizontal fast layer is an area with velocity perturbations ranging from 0% to −3% with the centre of the slow area centred at 925 km along the profile with a depth of 300 km (B). Within the top 50 km, centred at 300 km along the profile, is a low velocity area ranging from −3% to −6% with a width of 425 km (C). At the southwest end of the profile at a depth of 300 to 400 km is a lower velocity anomaly reaching −8% (A).

8.2 Synthesis

As stated earlier some of Features A through H have been identified across multiple profiles. Table 8.1 provides a summary of each feature, the profiles with which it is present, the range of perturbations calculated, the depth where the feature exists, and any other additional information.

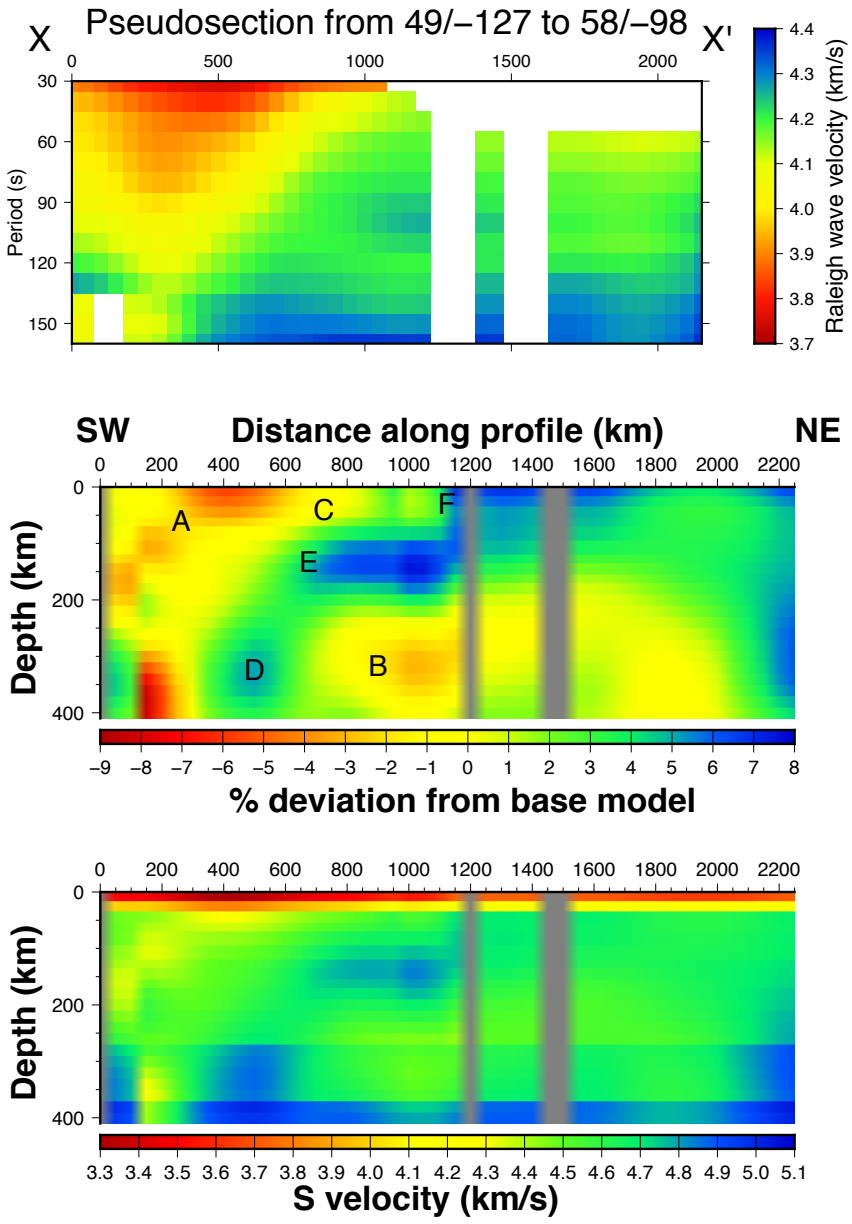

Figure 8.9: Profile X: Pseudosection (top panel) and cross-sections (middle and lower panels) modelled along the same profile as Miller and Eaton, 2010.

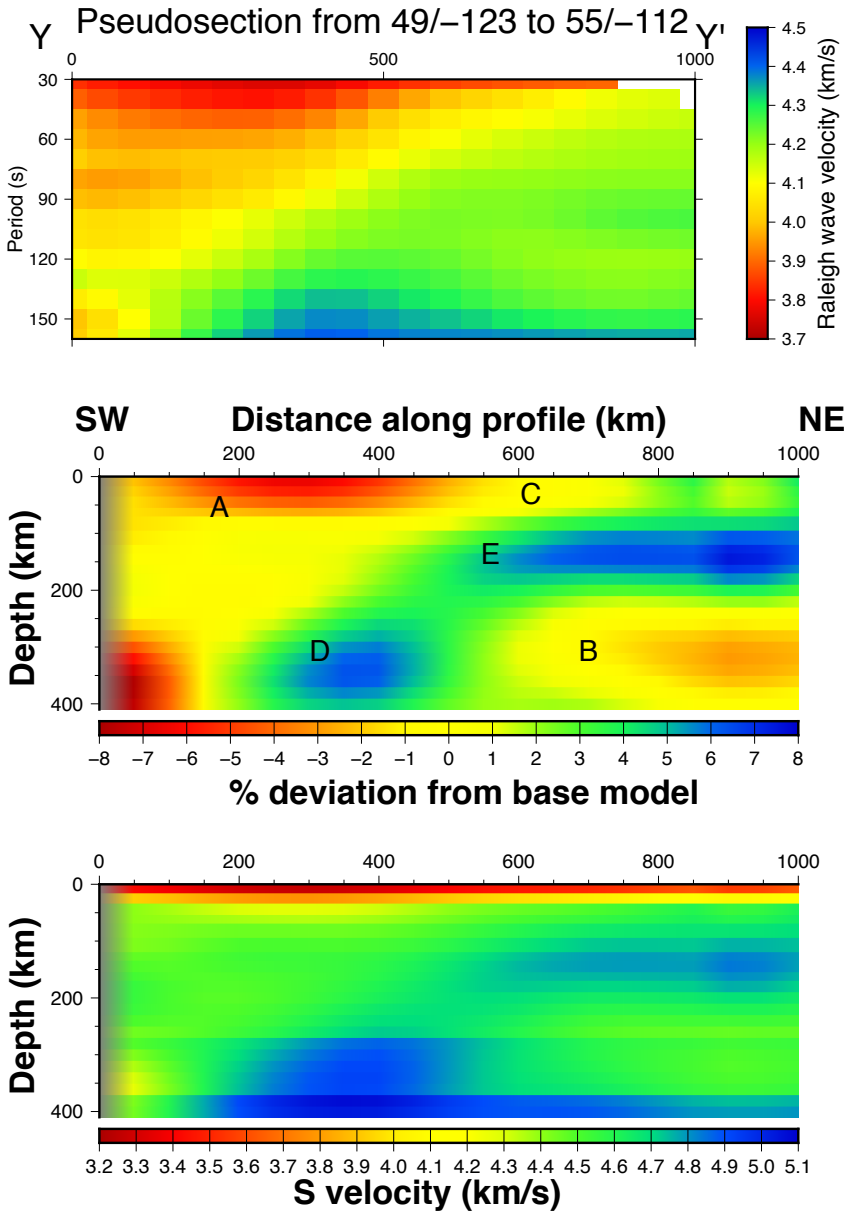

Figure 8.10: Profile Y: Pseudosection (top panel) and cross-sections (middle and lower panels) modelled along the profile as Bao *et al.*, 2014.

Table 8.1: Summary of features

Feature	Profiles	Perturbation (%)	Approximate Depth	Info.
A	A,B,C,D,L,X,Y	-3% − -5%	50 - 200 km	
B	A,B,X,Y	-1% − -2%	250 - 410 km	
C	A,B,C,X,Y	1%	$<$ 60km	Background velocity (IASP91)
D	A,B,C,D,X,Y	4% − 7%	300 - 410 km	
E	A,B,C,L,S,X,Y	4% − 10%	100 - 300 km	
F	A,B,X	5%	$<$ 100km	
G	D	-2% − -4%	200 - 410 km	
H	A,B,C	Boundary		Dip: Northeast from 100 km to 400 km depth

Features A (negative), C(intermediate), E and F (both positive), and H (transition) appear at depths less than 200 km. The large region of negative velocity perturbation (feature A) located in the west and southwest of the study area is seen across profiles A, B, C, D, L, X, and Y with the most negative velocity perturbation centred near profile B. The extension of this negative perturbation extends to shallow depths in the southern profiles but is not seen in the north (near profile C). To the east and northeast of Feature A is a positive velocity perturbation (Feature E) seen along profiles A, B, C, L, S, X, and Y and continues northeastward until the end of profiles A, B, C, and X. Feature C is an intermediate velocity perturbation (0%) lying directly above feature E with a depth less than 60 km. The intermediate velocity perturbation boundary (H) is located between Features A and E.

Below the southwestern most point of Feature E is a negative perturbation velocity (Feature B) seen in profiles A and B. At a similar depth as Feature B is Feature D, which is a positive perturbation velocity seen along profiles A, B, C, D, X, and Y. The primary location of this feature is below Feature A along profiles A, B, C, D, X, and Y, with similar additional features along profiles C and D. Features G are located only along profile D between Features D along the same profile.

Chapter 9

Discussion

9.1 Resolution tests

Resolution tests were done to verify the reliability of the maps and cross-sections derived from the tomographic inversions. These tests were performed to help assess the adequacy of the station pair-path coverage as well as the depth resolution.

9.1.1 Horizontal resolution test

To test the horizontal resolution of the output model, a checkerboard test was performed. This test consists of creating a synthetic model of alternating positive and negative velocity perturbations similar to a checkerboard, with background velocity separating each square. The vertical extent of the velocity perturbations exists at all periods. The area of the checkerboard was set as 49° to 79° latitudinally and -140° to -90° longitudinally. The dimension of the squares for the latitude was 4° and the longitude was 8° with a velocity perturbation of 0.4 m/s. The latitudinal and longitudinal spaces between squares were 2° and 4°, respectively.

The recovered synthetic models, for 60 and 120 second periods respectively, are shown in Figures 9.1 and 9.2. The outskirts of both figures are not well resolved due

to the low coverage for the area, as expected. In the area of the Cordillera/craton boundary, the six squares are well resolved with some smearing of velocity present, indicating decent lateral resolution. This pattern of smearing is seen throughout the inverted models thereby reducing the sharpness of the boundaries, but can still successfully recover features ca. 400 km across at all periods.

9.1.2 Vertical resolution test

The vertical resolution test involves creating synthetic 1-D models containing anomalies superimposed on velocities from IASP91. Eight synthetic 1-D models were created for each combination of positive and negative anomalies, of either 300 m/s or 500 m/s magnitude, at lithospheric and sub-lithospheric depths. Dispersion curves were generated from these models, then inverted to test recovery of structure.

Negative anomalies

Figure 9.3 shows the recovered models resulting from adding a deep, negative 300 m/s (top) and 500 m/s (bottom) anomaly to the IASP91 base model. The depth to the top of the anomaly is 270 km with a thickness of 80 km. The recovered negative anomaly is weaker than the input, showing about 2/3 of the original peak amplitude in the 300 m/s case, and about 1/2 in the 500 m/s case. The anomaly is smoothed and broadened, covering a wider depth range. This results in the removal of sharp edges. The broadening is asymmetrical, being biased toward shallower depths. The entire model is slightly slower, even at very shallow depths.

Figure 9.4 shows recovered models resulting from adding a negative 300 m/s (top) and 500 m/s (bottom) anomaly at a shallower depth than the above example. The depth to the top of the anomaly is 70 km with a thickness of 85 km. The recovered negative anomaly amplitude is nearly equal to that of the input model for both the

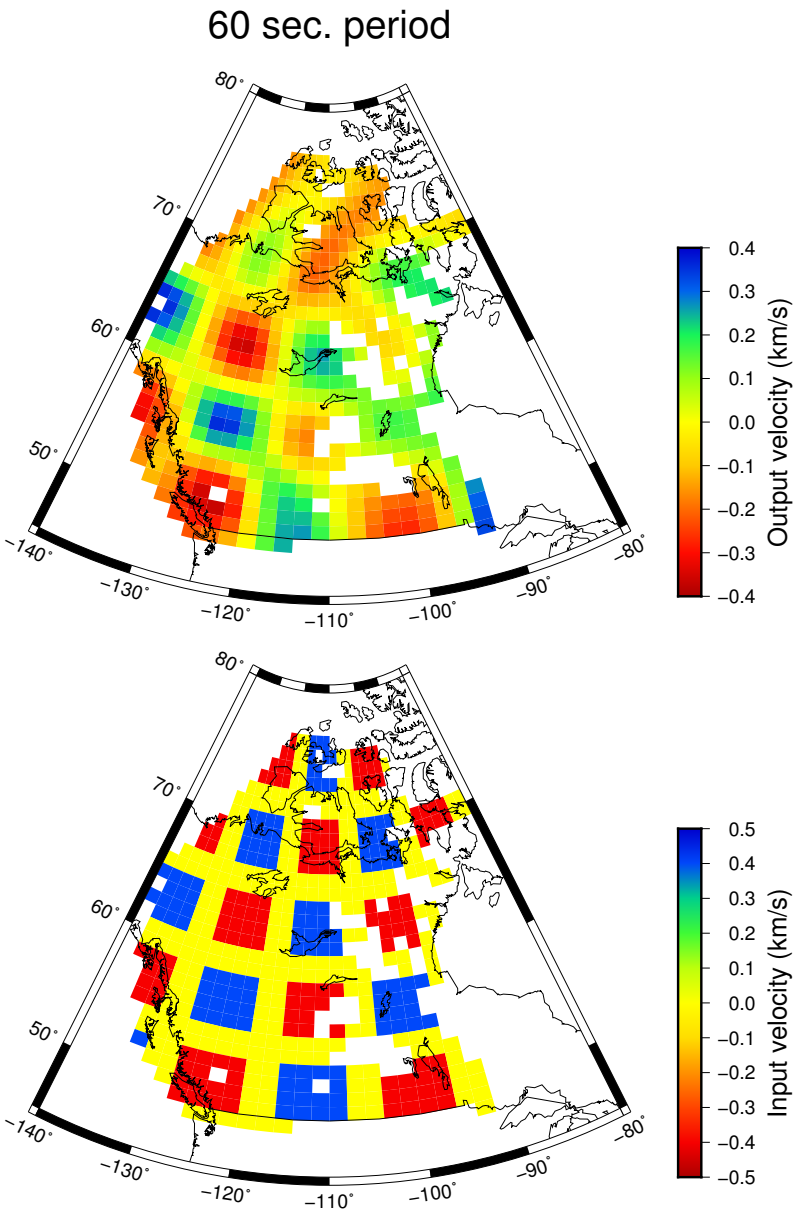

Figure 9.1: Velocity models for a period of 60 seconds: (top) output model and (bottom) input model. Areas of white indicate no station coverage.

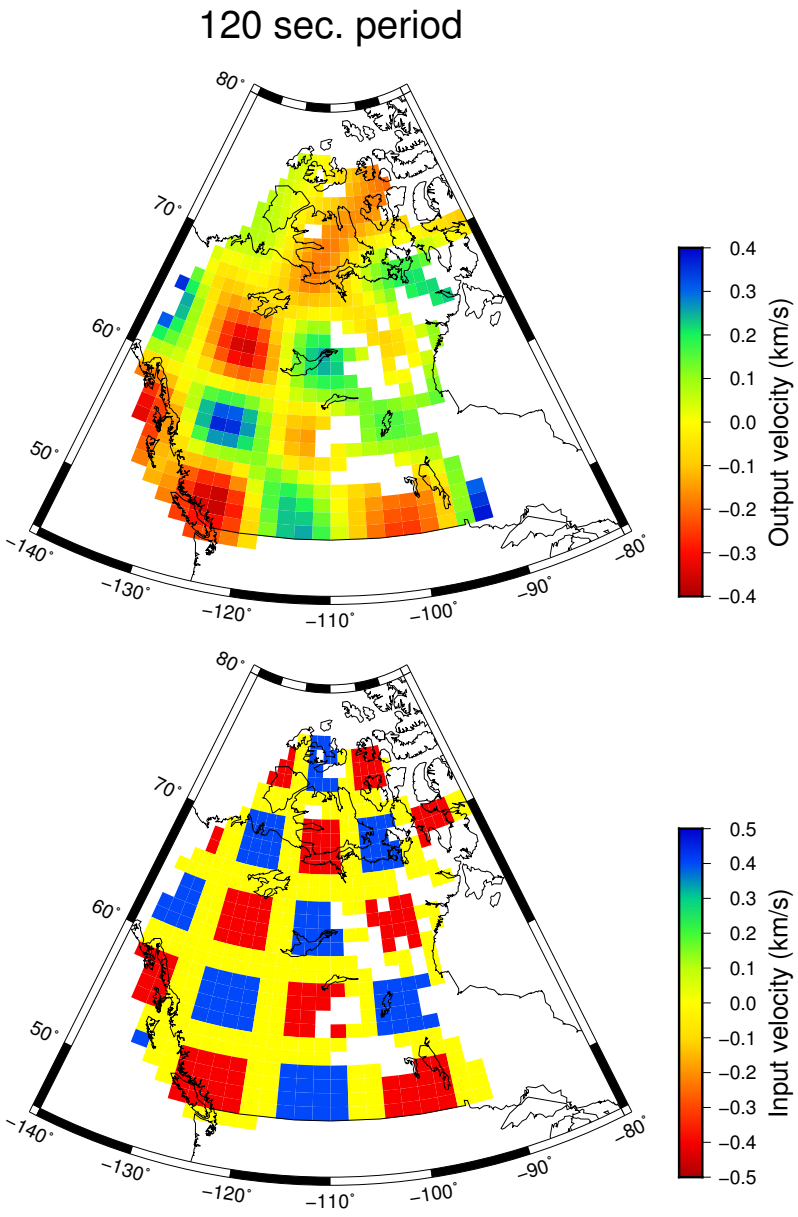

Figure 9.2: Velocity models for a period of 120 seconds: (top) Output model and (bottom) Input model.

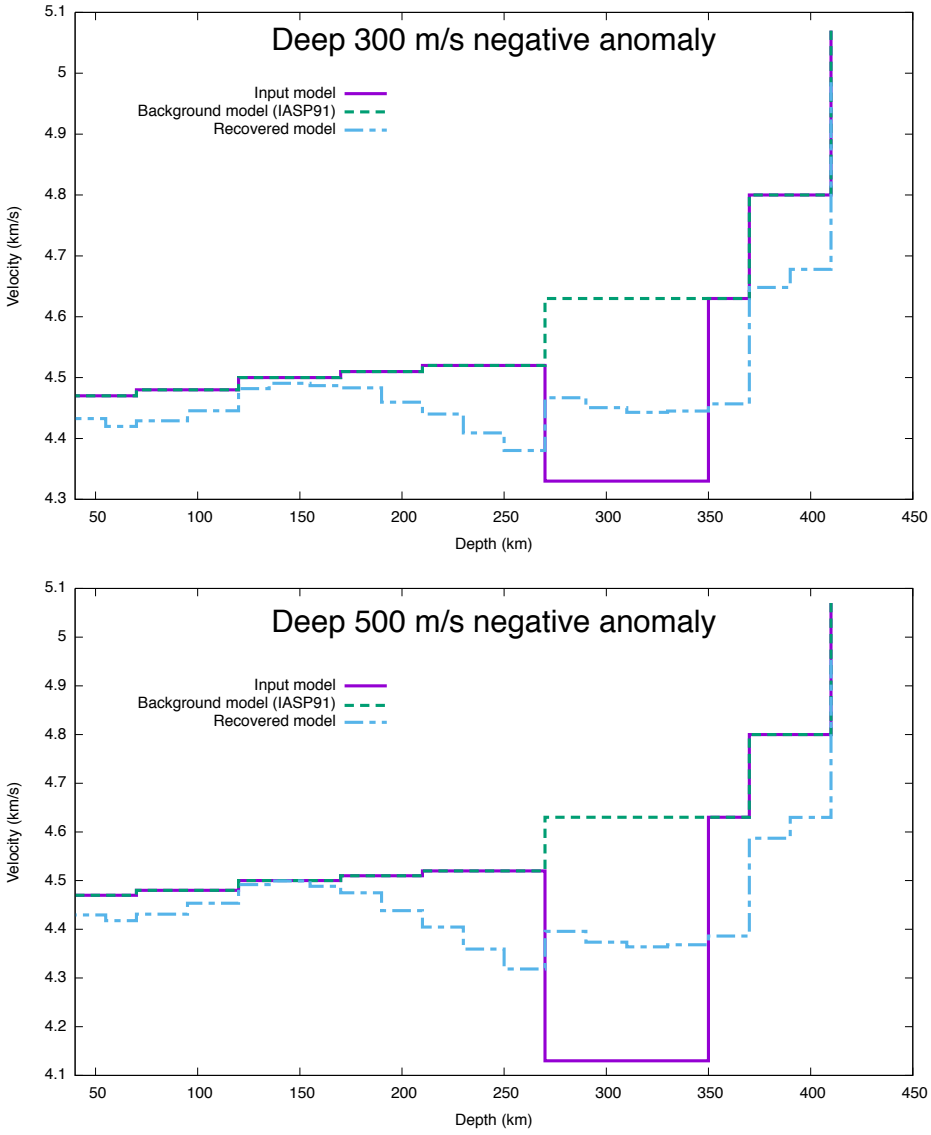

Figure 9.3: Vertical resolution test for deep negative (top) 300 m/s and (bottom) 500 m/s anomalies. The solid purple line corresponds to the model input, light blue dash-dot line corresponds to the recovered model, and the green dashed line corresponds to the IASP91 model.

300 m/s and 500 m/s cases. The pattern is similar to Figure 9.3 but broadening is biased downward rather than upward. Much like the case of the deep negative anomaly, the entire model is slightly slower. As stated previously, the smoothing has also removed sharp edges for this model.

Positive anomalies

Figure 9.5 shows the recovered model resulting from adding a 300 m/s (top) and 500 m/s (bottom) anomaly, similar to what was done with the negative anomalies earlier, at 270 km depth. The recovered positive anomaly is much weaker than the input (about 1/10 peak amplitude in the 300 m/s case, about 1/5 in the 500 m/s case). Much like in the case of the negative anomalies presented above, the anomaly is smoothed and broadened covering a wider depth range with no indication of sharp edges. The broadening is asymmetrical and is biased toward shallower depths. At depths less than 200 km, the recovered model is slightly slower than the input model. At depths greater than 200 km, the recovered model is slightly faster than the input model.

The recovered models for the shallow (top of the anomaly at a depth of 70 km, with a thickness of 85 km) positive anomalies are shown in Figure 9.6. The recovered positive anomaly is weaker than the input (about 2/3 peak amplitude in both the 300 m/s and 500 m/s cases). The anomaly is broadened asymmetrically, being biased downward. Below 225 km depth the recovered model is slightly slower than the input model. The smoothing is also somewhat asymmetric in that upward a much more sharp edge remains in the model compared to downward.

From both the shallow and deep negative anomaly models some conclusions can be drawn. Deep high-velocity anomalies are recovered quite poorly, producing a small spurious low-velocity anomaly at shallow depth. The consequence of this being that deep high-velocity features are underestimated relative to other features. This also

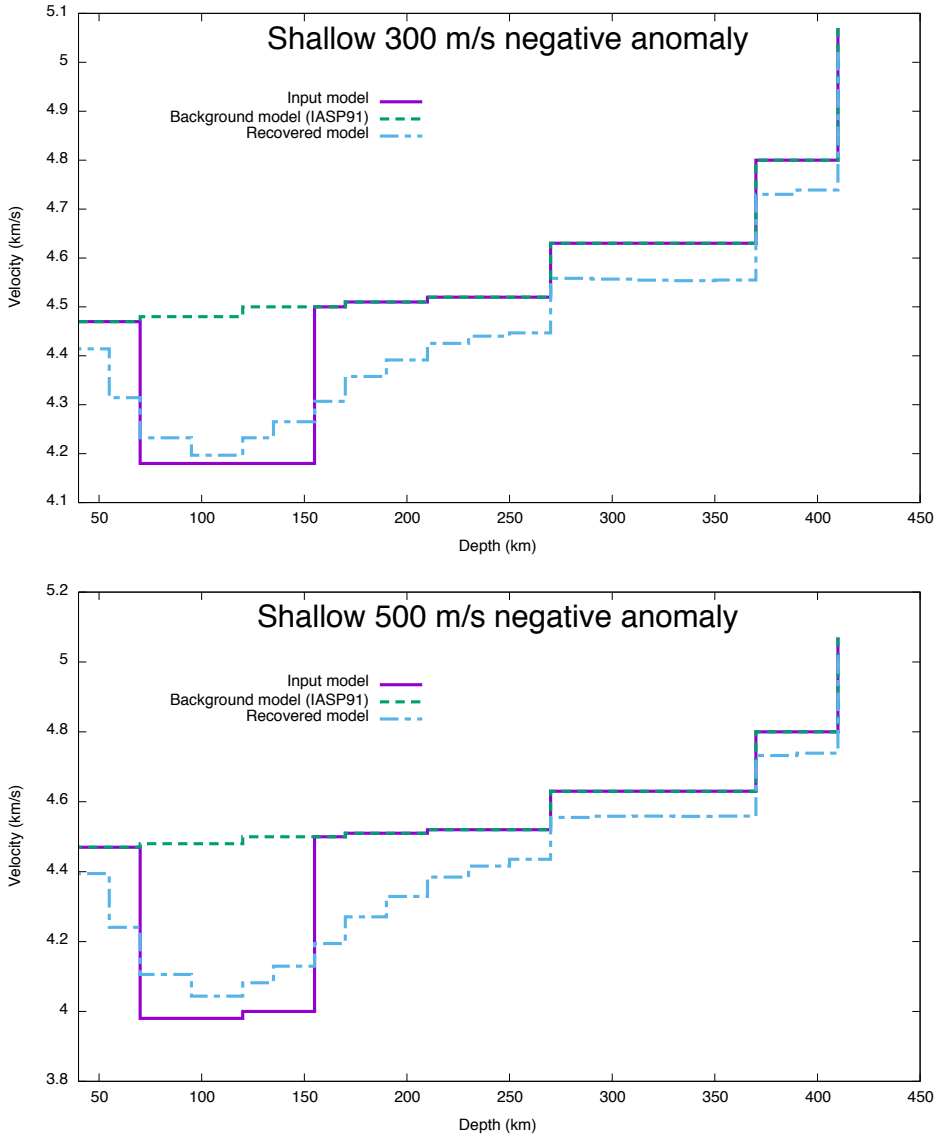

Figure 9.4: Vertical resolution test for shallow negative (top) 300 m/s and (bottom) 500 m/s anomalies.

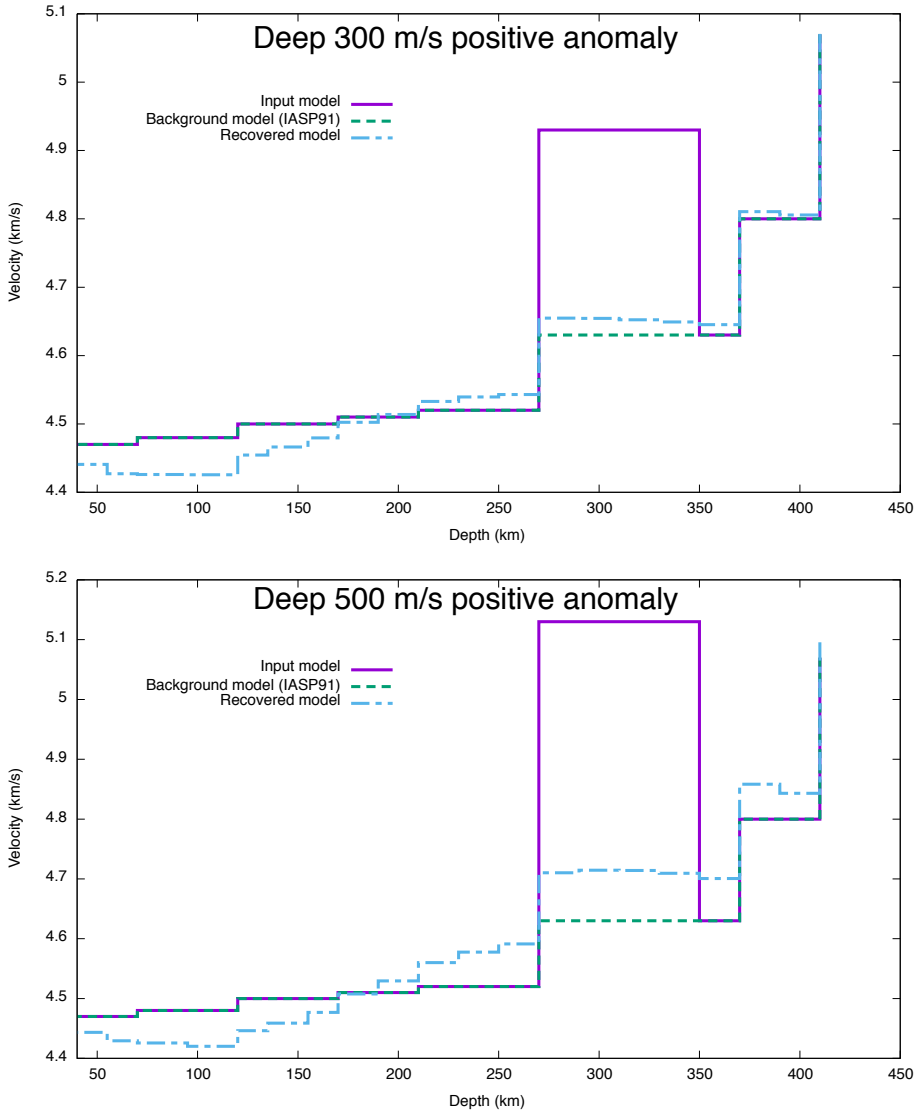

Figure 9.5: Vertical resolution test for deep positive (top) 300 m/s and (bottom) 500 m/s anomalies.

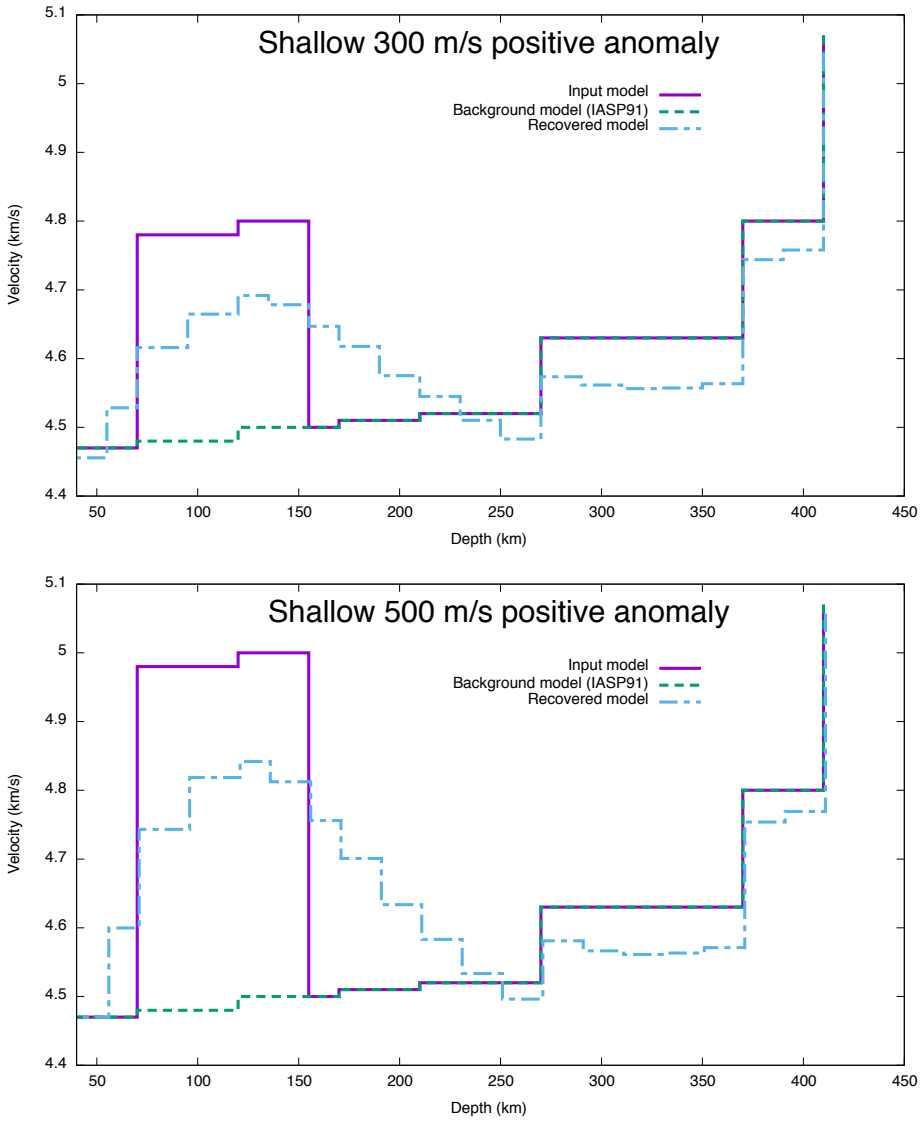

Figure 9.6: Vertical resolution test for shallow positive (top) 300 m/s and (bottom) 500 m/s anomalies.

shows that both deep high and low-velocity anomalies can bias shallow structure. For shallow high and low-velocity anomalies, downward smearing exists such that some features may not extend as deep as they appear.

Resolution test summary

Main observations from the vertical resolution test show that deep features are smeared upwards while shallow features are smeared downwards. Sharp edges, between contrasting layers, are not recovered. Deep high-velocity features are very poorly recovered and can produce shallow low-velocity artifacts while shallower anomalies are recovered more accurately. Deep low-velocity features are broadened but aren't missed.

9.2 Major features

As seen in chapters 7 and 8, the lithosphere of the study area has a number of features of interest. These include large positive (E) and negative (A) velocity perturbations, many small high-velocity anomalies at >300 km depth, and low-velocity anomalies extending downwards to the 410 discontinuity. To the southwest there is a negative velocity perturbation that appears to be split by a positive velocity perturbation wedge from the northeast. Below 300 km depth small regions of positive velocity perturbation are present throughout the Cordillera. Centred around Great Slave Lake, a positive velocity perturbation is present within the already fast velocity craton. Figures 9.7 and 9.8 show these various major features, which will be interpreted in the next sections.

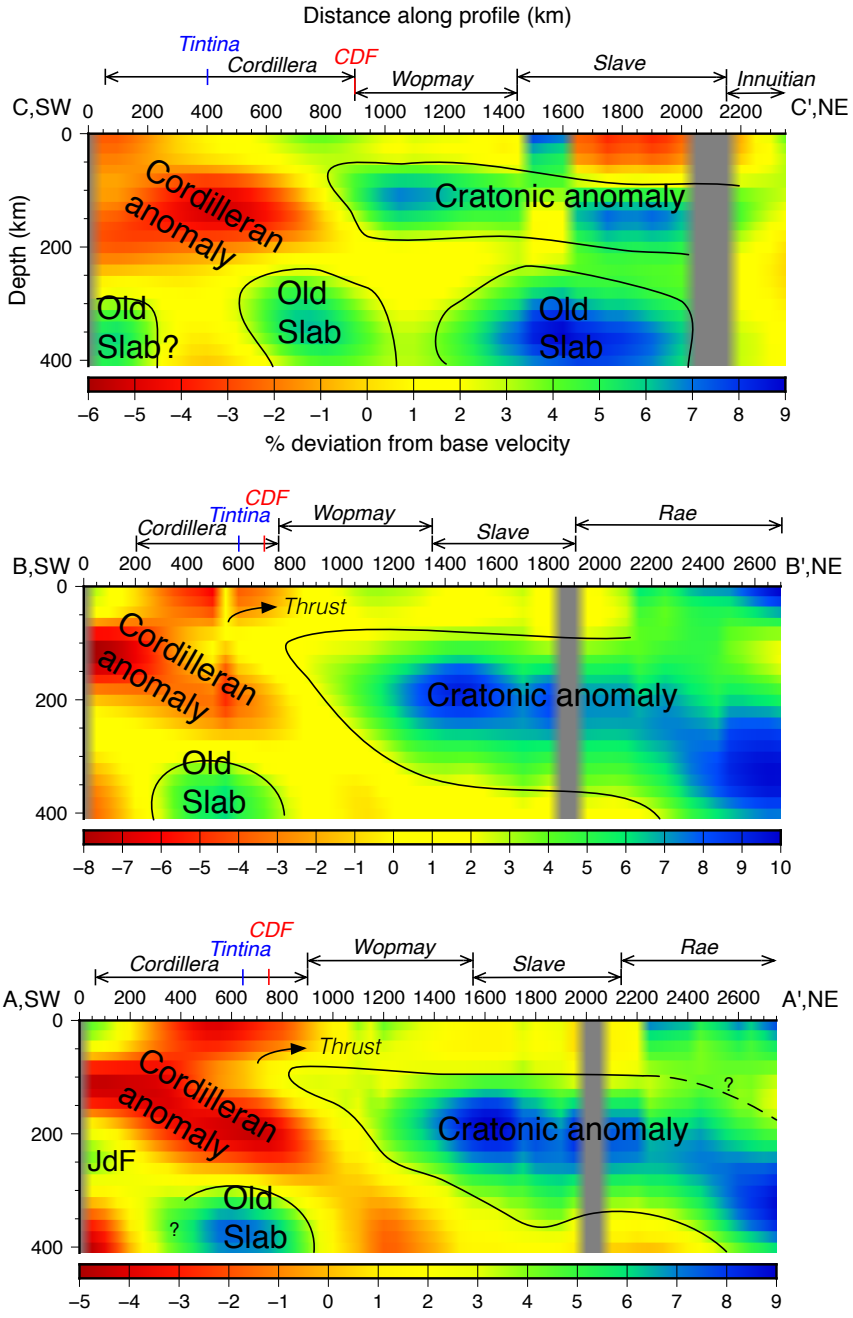

Figure 9.7: Interpreted cross-section along profiles C (top), B (middle), and A (bottom) where solid lines indicate extent of feature and dashed lines indicate extrapolated extent of feature. CDF corresponds to the Cordilleran Deformation Front and Tintina to the Tintina Fault. The profiles are arranged from north to south down the page.

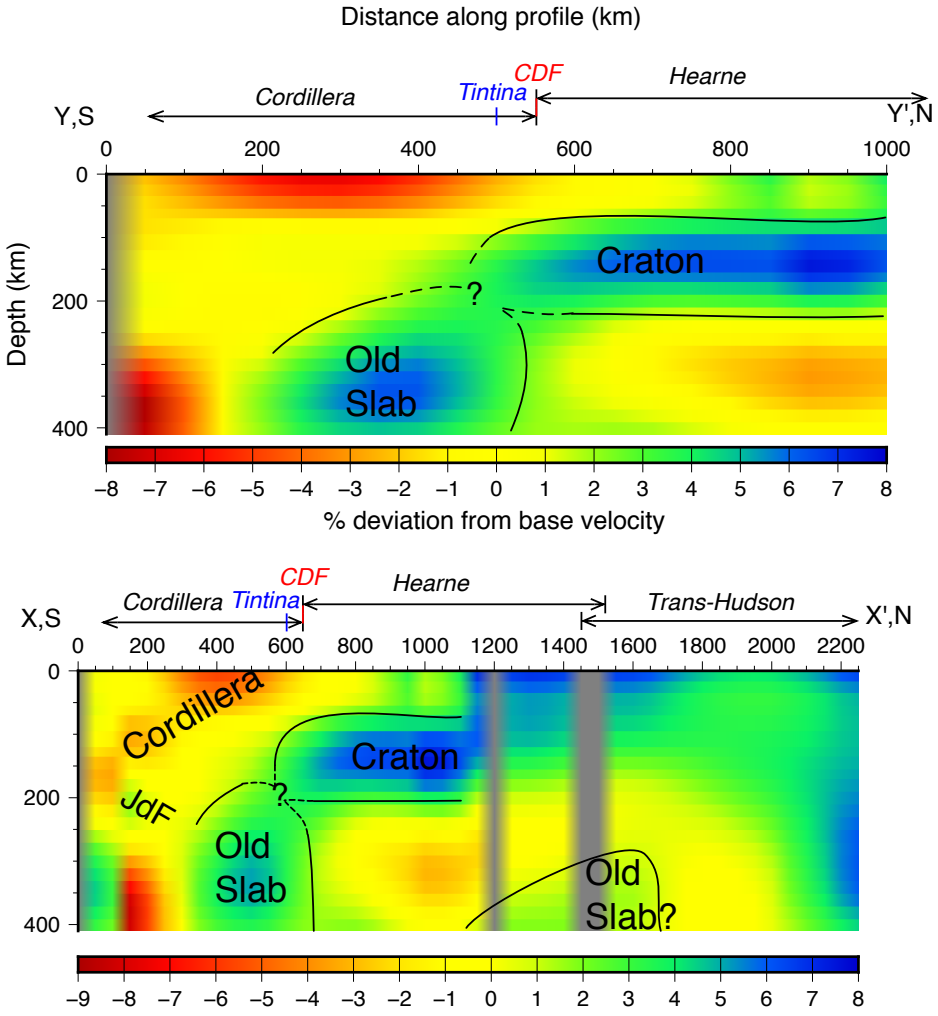

Figure 9.8: Interpreted cross-section along profiles Y (top) and X (bottom).

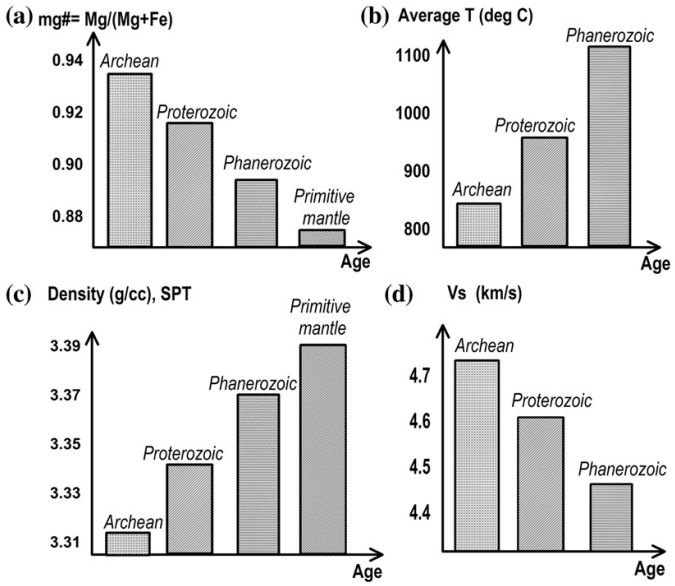

Figure 9.9: Average physical properties of the continental lithospheric mantle as stated by Artemieva (2009) of a) forsterite content, b) average mantle temperature c) density at standard pressure and temperature, and d) S-wave seismic velocity.

9.3 Cratonic high-velocity lithosphere

Given the association between Precambrian shields and high-velocity lithosphere, it is believed that the cratonic lithosphere is as old as the crust above, requiring that the lithosphere be not only cold, but chemically depleted as well (Jordan, 1978). Figure 9.9 shows results from Artemieva (2009) showing a relation between forsterite content, average mantle temperature, density at standard pressure and temperature, and S-wave seismic velocity base on variations in compositional and temperature. As seen in Figure 9.9 the density of older, and thus cooler rocks, decreases which counteracts the buoyancy lost to cooling, in accordance with the isopycnic hypothesis.

In the Canadian craton, a high-velocity perturbation is present down to depths of 175-350 km (Figure 9.7). The outline of the cratonic lithosphere was assigned based on the 3% perturbation contour (green colour), from which these depths were interpreted. To the south, profiles X and Y (Figure 9.8) show an intermediate thickness of 200 km

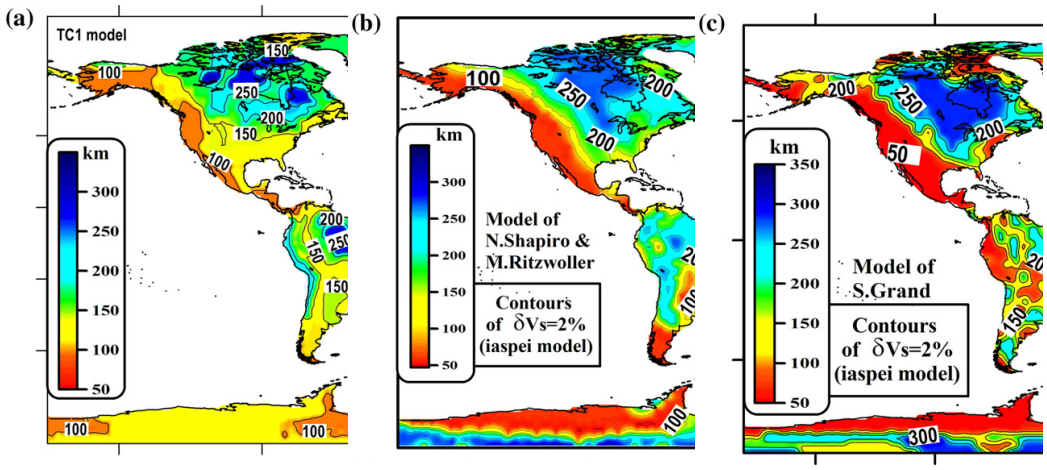

Figure 9.10: Thickness of the lithosphere defined from a) thermal modeling b) surface-wave seismic tomography and c) body-wave seismic tomography (Artemieva, 2009).

for Feature E. Moving northward (profiles A and B), Feature E increases in thickness, to about 350 km, but then appears to become thinner (175 km) in the northernmost profile (C).

Continental lithosphere thickness results from Artemieva (2009) show that the base of the continental lithosphere is 200 - 250 km (from surface-wave and body-wave models) in Figure 9.10. Stacked S-wave receiver function results from Miller and Eaton (2010) (Figure 9.11) show a cratonic lithosphere base of <200 km which is in agreement with the range determined by Artemeiva (2009). More recent results along a profile similar to profile Y, by Bao et al. (2014), show (Figure 9.12) a greater lithospheric thickness (approaching 250 km) near the Miller and Eaton profile, which is deeper than found by both Miller and Eaton (2010) and Artemieva (2009).

An east/west profile (Figure 9.13), within the P velocity model by Mercier et al., (2009), identifies a high-velocity anomaly located east of the Cordilleran deformation front (cross-section along 60.5°N). This feature has a base extending to depths near 300 km with a velocity consistently 2 - 4% faster than background values (Mercier et al., 2009). Note, however that the teleseismic tomography method used by Mercier

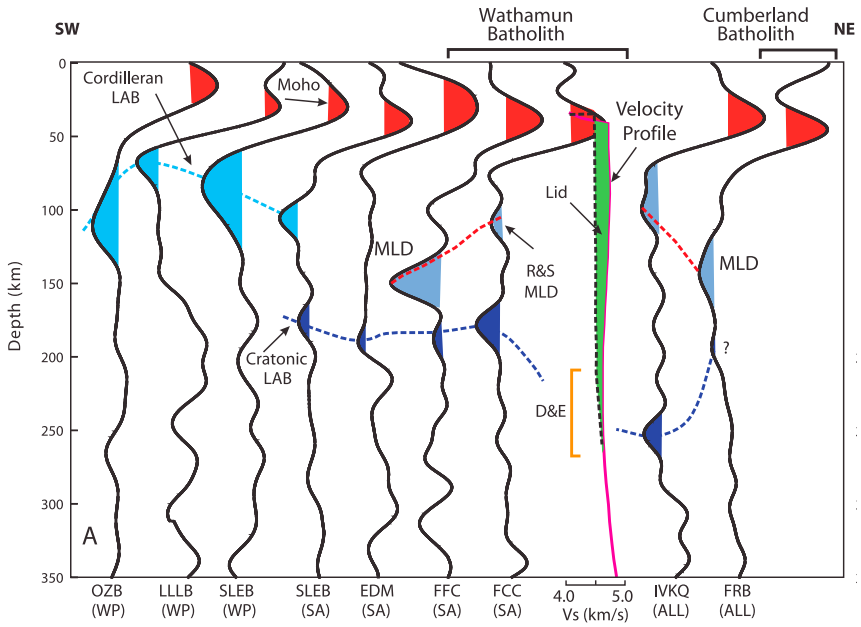

Figure 9.11: Stacked S-wave receiver function profile on which profile X was based (Miller and Eaton, 2010).

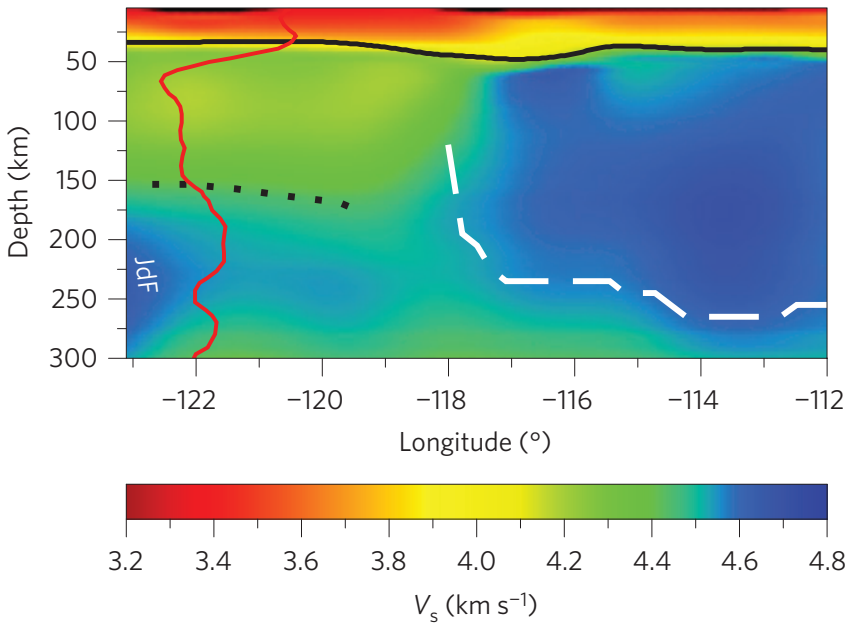

Figure 9.12: Cross-section results of Bao et al. (2014) showing the inferred base of the cratonic lithosphere (dashed white line), high-velocity anomaly (dotted black line indicates the top of the this layer), and the Juan de Fuca slab (JdF). The high-velocity anomaly is interpreted by Bao et al. (2014) as delaminated lithosphere.

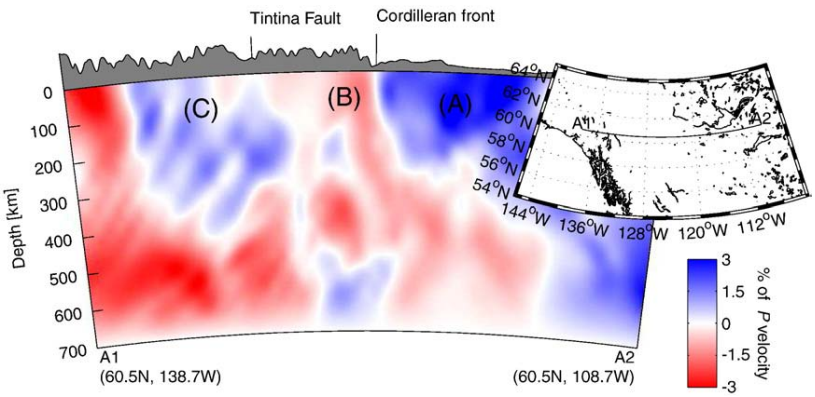

Figure 9.13: P velocity model cross section from Mercier et al. (2009) along an east/west profile along at latitude of 60.5°N. Note the large positive velocity perturbation east of the Cordilleran front (labeled A).

et al. (2009) tends to smear structure vertically down ray paths, thus exaggerating the depth to the base of large features.

Thermal results from Hardebol et al. (2013) show that the base of the thermal lithosphere (defined as the 1300° isotherm) is greater than 200 km depth and results from Artemieva (2009) show lithospheric thickness being >150 km (thermal model). The increased depth of the isotherm shows that the material above this depth is colder, and thus older, than the material to the west. The area to the west will be discussed more in section 9.5.

These studies are in agreement with my results showing that the existence of a faster velocity anomaly perturbation (anywhere from 2-8% faster than background values) is evidence of the cratonic lithosphere with a depth ranging from 150 - 300+ km. From this the cratonic lithosphere anomaly is interpreted to be a chemically depleted, cold layer that is 200 km thick on average. The extent of this cratonic lithosphere anomaly matches the older geological provinces as discussed in Chapter 2.

9.4 Great Slave Lake anomaly

In chapters 7 and 8 a high-velocity anomaly (Feature GSL) was identified beneath Great Slave Lake. Profile L (Figure 9.14) shows the western extent of the Great Slave Lake feature. The craton and Ancestral North American portion of the Cordillera have a background velocity of 3% above the base model, which I have defined as cratonic velocity. It is important to note that these background velocities, for profiles L and S, are in fact significantly higher than on other profiles. Along profile L, from 350 - 1050 km, the GSL fast velocity anomaly feature is present within the craton, more specifically beneath the Wopmay and Slave provinces. Velocities of this anomaly range from 4% to >8% above the base model. The fast anomaly terminates at the lithosphere-asthenosphere boundary at a depth of approximately 300 km.

Profile S (Figure 9.14) shows the north/south extent of the anomaly. This profile, as geologically mapped, cross through the centre of the Great Bear Magmatic Arc in the north, from 0 km to 800 km, and crosses through the Buffalo Head Terrane from 800 km to 1100 km, in the south. The boundary of the anomaly at 800 km corresponds with the location of the Great Slave Lake shear zone (GSLsz). In Figure 9.14 a majority of the craton has a velocity perturbation of 3-4%. Velocity perturbations less than 100 km are equal to IASP91 values until the GSLsz, where they become 3%. The lithosphere-asthenosphere boundary is identified at a depth of 300 km north of the GSLsz, south of which it decreases in depth to 250 km. The GSL anomaly is centred at 200 km depth and includes velocities >5% faster than the IASP91 value.

The western extent of the GSL anomaly matches the boundary between the Wopmay province and Ancestral North America, with ages of Proterozoic and Devonian-early Mississipian, respectively. The southern boundary is the GSLsz. South of this point, the velocity is 3% - 4% above IASP91 which coincides with the Buffalo Head terrane and is consistent with the craton as a whole.

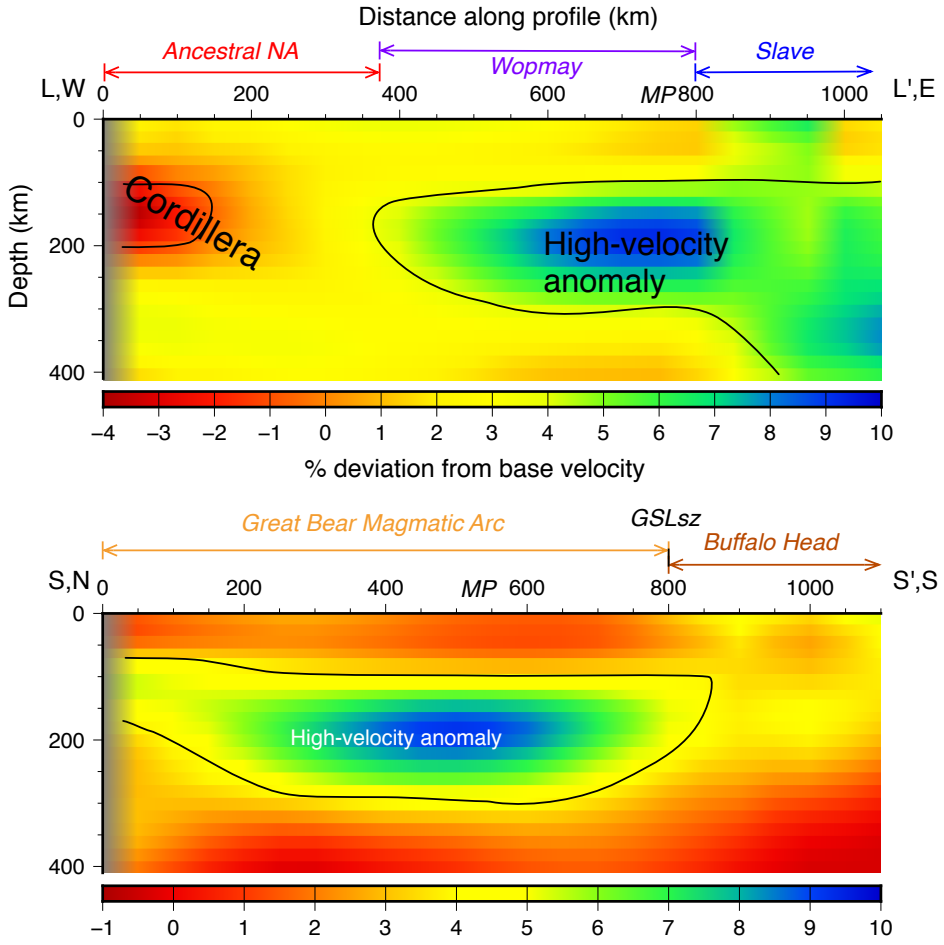

Figure 9.14: Interpreted cross-section along profiles L (top) and S (bottom).

The Great Slave Lake feature is consistent with, although at a greater depth than, results of Fernandez-Viejo and Clowes (2003) (SNORE line 11), and compiled by Clowes et al. (2005), showing an increased uppermost mantle P-wave velocity, down to a depth of 100 km, immediately north and west of the Great Slave Lake with values of 0.4 to 0.6 km/s (5% to 7.5%) greater than the global average (Figure 9.15).

Seismic reflection done by Cook et al. (1998 and 1999) shows a portion of Archean (Slave) mantle extending under the Wopmay orogen with the Hottah mantle underlying the Slave mantle. The Slave mantle is shallow and immediately below the crust.

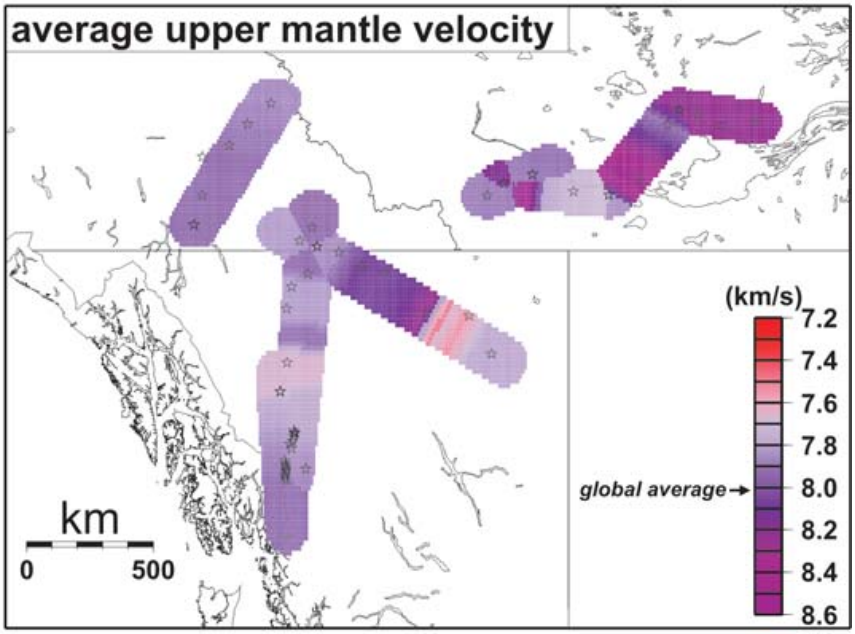

Figure 9.15: Average upper mantle velocity from SNORE'97 refraction line (Clowes et al., 2005) where global average from Christensen and Mooney (1995) is for reference.

Using teleseismic results from Bostock (1998), Cook et al. (1999) correlate the mantle reflector (M2) with remnants of Proterozoic subduction. At greater depth the M2 reflector by Bostock (1998) (Figure 9.16 top) supports this result with the added suggestion of a continuation of the Fort Simpson terrane dipping reflectors, Su1 and Su2, dipping from 170 km in the west to 230 km in the centre of the Slave province. Both reflectors coincide well with upper and lower boundaries of the Great Slave Lake anomaly identified along profile L (Figure 9.16 bottom) with depths of 125 and 225 km.

To obtain the velocity perturbation values of 5% to 7.5%, greater than IASP91, observed in the present study this feature would most likely correspond to a subducted slab as suggested by Cook et al. (1999). The perturbation is larger than observed in the Slave craton (Figure 9.14) and larger than expected for depleted lithosphere (Figure 9.9). In contrast tomographic results by Schmandt and Lin (2014) show a

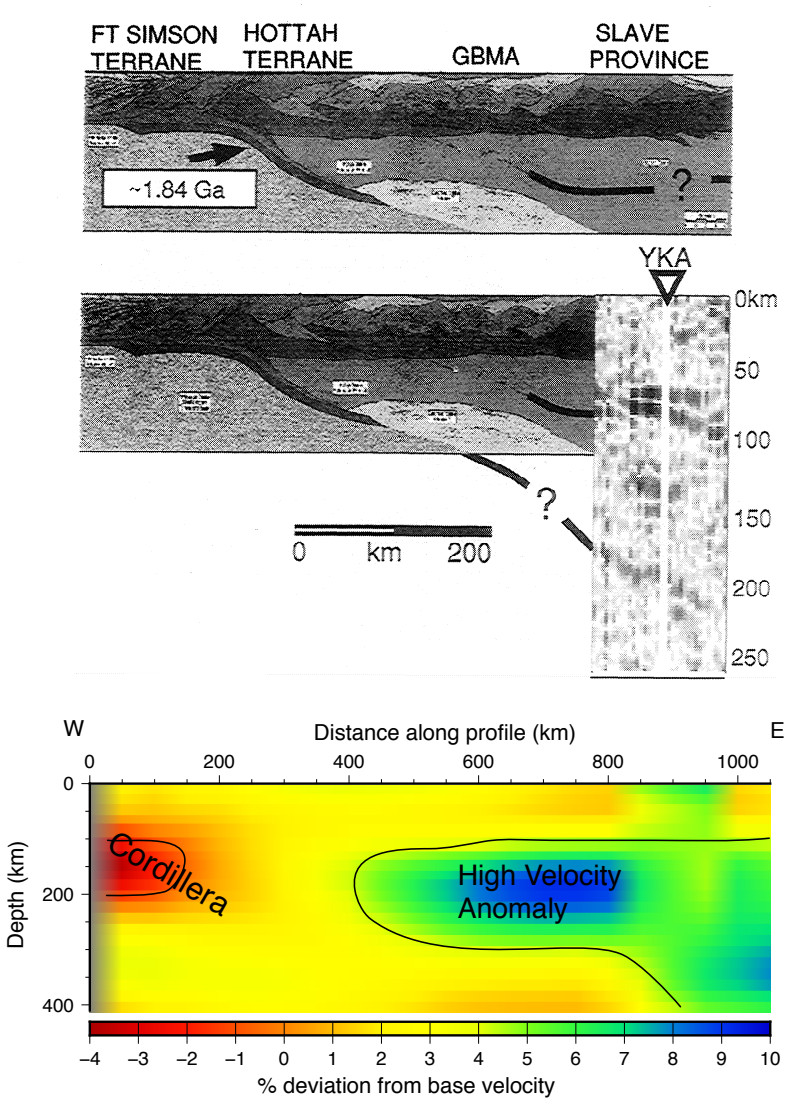

Figure 9.16: Analysis of SNORCLE corridor 1 reflection data juxtaposed with teleseismic data showing the potential for a dipping mantle feature below the Slave province (Bostock, 1998) (top). The result of profile L shows the possible emplacement of a high-velocity lithosphere from under the Slave province into the Wopmay province.

clear distinction between the background and interpreted remnants of Farallon plate subduction, showing the larger velocity perturbation created by subducted plates. The velocity difference between the two is anywhere from 3% to 6%.

Magnetotelluric results along the same east-west corridor as profile L (Jones et al., 1997; Jones et al., 2005) detect a southwest-dipping resistive layer (feature C in Figure 9.17 top) from the Slave into the Proterozoic. This feature flattens out well within the Proterozoic below 100 km depth with a thickness of 100 km, suggesting that this feature is a subduction remnant preserved within the Slave lithosphere. Further magnetotelluric results by Spratt et al. (2009), along a profile running WNW/ESE at approximately 64°, show large high-resistivity features down to depths of 200 km. Results along profile L match the location of these cratonic roots but, due to lower resolution, do not show the separation between cratonic roots seen in Spratt et al. (2009).

Given that the high-velocity feature beneath Great Slave Lake coincides with the dipping features seen in seismic and magnetotelluric studies, and is associated with past subduction events of the area, the Great Slave Lake feature is interpreted as high-velocity material associated with slab remnants. In the already cooler Wopmay lithosphere, this increased velocity anomaly is attributed to a significant compositional change (possibly to eclogite).

9.5 Cordilleran low-velocity anomaly

As stated in Chapter 8, a negative velocity perturbation is located in the southwest portions of profiles A, B, C, X, and Y as well as along profile D. The negative velocity perturbation is -3 − -5% and is located from 50 to 200 km depth. The extent of this anomaly is greater in the middle and northern profiles and it is less evident in the southern profiles. As observed in profiles A and B (Figure 9.7), and to a lesser extent

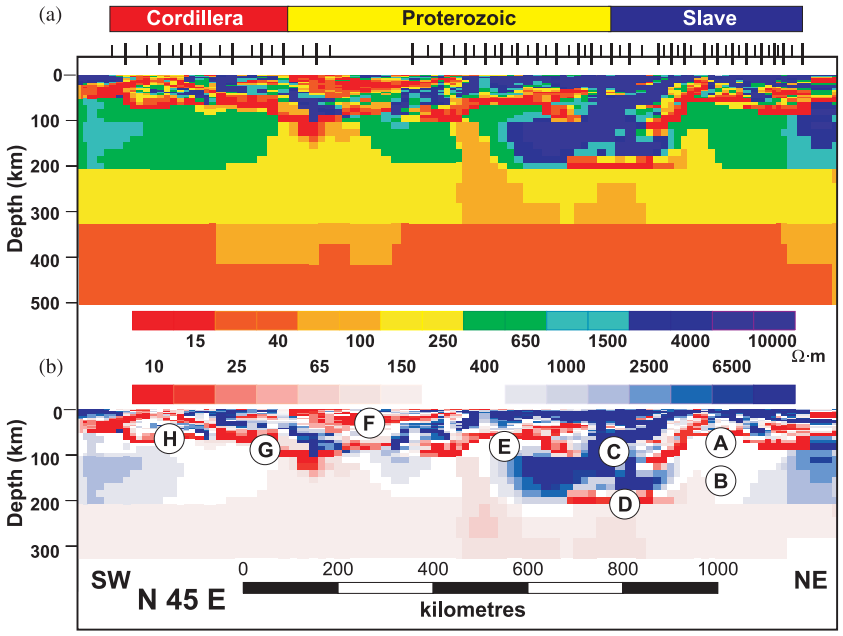

Figure 9.17: Cross-section of the regional magnetotelluric model for the SNORCLE corridors (Jones et al., 2005) where letters correspond to features identified by Jones et al., (2005).

in profile C, Feature A dips to the northeast under the cratonic high-velocity feature. Profiles X and Y do not exhibit this dip.

The surface boundary of the Cordillera is the Cordilleran Deformation Front as illustrated in many figures throughout the thesis. The large negative velocity perturbation region located in the southwest therefore underlies the Cordillera. Profile D (Figure 8.6) lies within the Cordillera and shows regional variation within the Cordilleran lithosphere.

Results from Mercier et al. (2009) (Figure 9.18) show that the mantle west of the Cordilleran Deformation Front (north of 50°N and 52°N latitude for S-wave and P-wave velocity models, respectively) mainly has a -2% velocity perturbation. At greater depths (300 km and 400 km), velocity perturbations become localized resulting in pockets of negative velocity perturbations within a generally positive velocity perturbation area. In the north (primarily above 55°N latitude), the low velocity zone remains intact, as is seen by Gabrielse and Yorath, (1991) and Frederiksen et al., (1998). The Mercier et al. (2009) body-wave model will underestimate large low-velocity or high-velocity regions due to the use of relative travel times. The area of study is therefore most likely to be low-velocity.

Using the stacked S-wave receiver function results shown in Figure 9.11, Miller and Eaton (2010) show that the Cordilleran lithosphere-asthenosphere is present at depths ranging from 60 to 100 km. This range in the boundary matches the thermal, surface-wave and body-wave tomography results by Artemieva (2009) (50 km - 100 km) in Figure 9.10.

Electrical resistivity structure from magnetotelluric measurements completed by Jones et al., (2005) shows a low-resistivity northeast-dipping feature in the Cordillera that is associated with lithospheric subduction during terrane accretion (Jones et al., 2005). The depth of this feature matches that of the top of the deeper low velocity zone of profile B labelled as Feature B in Figure 8.4.

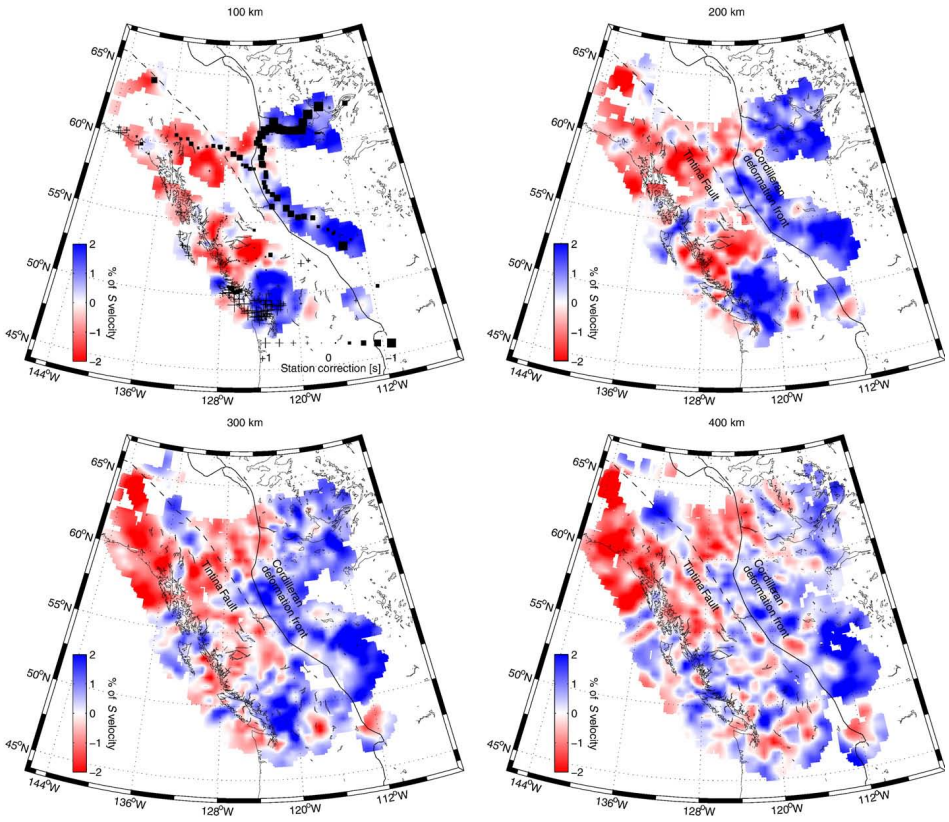

Figure 9.18: Depth slices of the Mercier et al. (2009) survey for depths of 100 km, 200 km, 300 km, and 400 km for the S-wave velocity model (Mercier et al., 2009).

Low velocity features are common in the mantle beneath active orogens. High heat flow, resulting from active orogens, indicates high mantle temperature and thus lower velocities. Another effect on velocity is due to the compositional difference between the Cordilleran and cratonic mantles as explained by the isopycnic hypothesis and analyzed by Artemieva (2009).

9.6 Cordillera/craton boundary

Feature H in the previous chapter corresponds to the Cordillera/craton boundary. The Cordillera/craton boundary is not a sharp boundary since the transition between the slow and fast velocity zones, as seen on multiple profiles, is in some cases 200 kilometres wide. All profiles (A, B, C, X, and Y) appear to show a clear signature ($> +3\%$ anomaly) at depths of 100 to 200 km, that extends eastward and as far west as the Cordilleran Deformation Front (or possibly further west near the Tintina Fault on profiles X and Y). On profiles C, B, and A the southwestern tip of this cratonic feature has a wedge like form with its lower margin dipping to the northeast. On profiles X and Y the form of the southwestern extent of the cratonic lithosphere is obscured by smearing of the response with that of a deeper high-velocity feature. The eastern margin of the very slow (definitively Cordilleran) velocities ($< -3\%$), in the <100 km depth range, coincides approximately with the Cordilleran Deformation Front on profiles B, A, and X, but occurs farther west on profile C.

The contrast in velocity perturbation from negative in the southwest to positive in the northeast is the basis of this identification. Due to the large scale of this project, a larger range of velocity perturbation was observed (-4% $-$ 5%) compared to smaller scale study areas ($\pm 2\%$ in Mercier et al. 2009). This may be as a consequence of previous studies using relative travel time, in that large blocks of uniform velocity get missed leading to an underestimate of the contrast. Surface wave cross-sections,

discussed earlier, show a non-vertical boundary dipping to the northeast. The extent of this deviation from vertical is not precisely defined due to horizontal smearing of surface waves. Near the boundary (of profile A) the contrast is not as sharp as for profiles B and C.

Teleseismic body-wave results by Mercier et al. (2009) show a sharp contrast between low and high-velocity anomalies centred roughly on the Cordillera Deformation Front. The range of velocity perturbation is generally about ±2%. At depths of 100 - 200 km the location of the boundary is similar between the surface wave of this study and body-wave velocity models of Mercier et al. (2009). The inherent vertical smearing of teleseismic travel-time images appears to affect deeper slices, showing a near vertical boundary. To the south of 55°N, beneath ancestral North America, is a large high-velocity anomaly extending eastward at a depth of 300 km. This anomaly is 2-4% faster than background P velocity values. Further north a low-velocity anomaly which extends at 200 km depth beneath the large high-velocity anomaly, and has a P velocity perturbation of -2%.

The location of the boundary resolved in the present study also agrees with stacked S-wave receiver function results from Miller and Eaton (2010) (Figure 9.11). Note that the precision of this method is based on the station spacing, approximately 300 km. The location of the Cordillera/craton boundary was detected by the seismic station SLEB (Sale Mountain, British Columbia). At SLEB, the Cordilleran lithosphere-asthenosphere boundary was recorded at a depth of 100 km, while the depth of the cratonic LAB was located at 175 km. Both these values agree with results obtained along profile X of a more shallow negative-velocity Cordilleran perturbation with a relatively flat cratonic LAB at 200 km.

According to a general model for an advancing subduction boundary (as illustrated in Yonkee and Weil, 2015; Figure 9.19) a wedge-like geometry will occur within the mantle lithosphere and asthenosphere. Two features present in the southwest of the

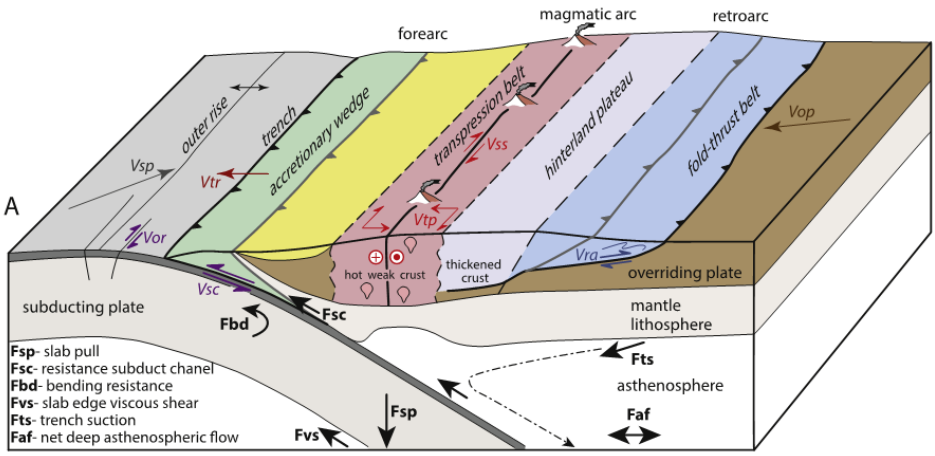

Figure 9.19: General model of an advancing type of subduction boundary (Yonkee and Weil, 2015).

study area are relevant to this wedge model. First is the overriding slow layer above the tip of the cratonic wedge. This part of the profile may coincide with the forearc and magmatic arc of previous subductions (in this case, the Kula plate subduction due to the latitude of profiles A and B) as discussed explicitly for the Cordillera by Monger (1989) based on Hyndman (1972). The second is what might be the remnants of the subduction channel, associated with the Kula plate subduction. This subduction channel force results in mantle lithosphere moving in opposition to the direction of force of the subducting plate (labelled Fsc in Figure 9.19). Profiles A and B show an upward curve of the cratonic lithosphere from depths of up to 400 km. During the previous subduction, cratonic asthenosphere was drawn upwards and westward by edge-driven advection (mostly seen in Figure 9.7 bottom). Mercier et al. (2009) identified a similar low-velocity feature extending beneath a high-velocity feature.

Tectono-thermal continental ages as determined by Artemieva (2009) show that the boundary between Early Proterozoic and Meso-Cenozoic (with a small area for Paleozoic, Late and Middle Proterozoic ages) matches the boundary as determined from my profiles. From Figure 9.20 the gradient style lateral change in age is similar

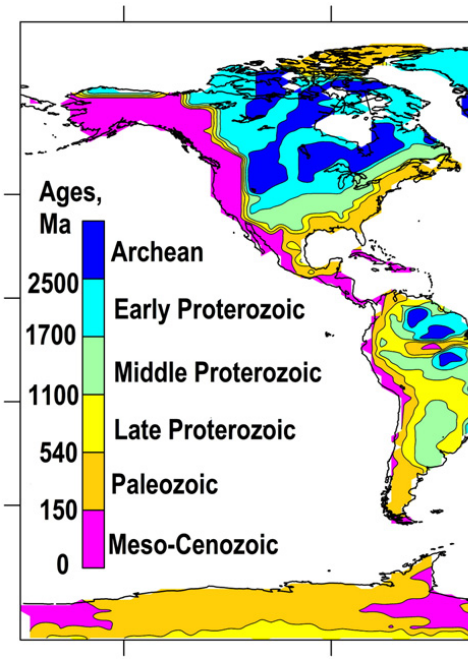

Figure 9.20: Tectono-thermal age of continental lithosphere as determined by Artemieva (2009) with emphasis on western and northern Canada.

to the thermal results of Hardebol et al. (2013). Their 120 km change in the base of the thermal lithosphere occurs laterally over 175 km, corresponding to an average dip of 34°. The Cordillera/craton boundary extends well into the mantle (300 km) dipping to the northeast ranging from 17°, along profile A, down to 39°, along profile C. This result matches thermal data. The possible mechanisms for the angle of the boundary include a flow up the subduction channel and/or erosion by edge-driven convection. The range in Cordillera/craton boundary dip angle may be as a result of edge-driven convection discussed by Hardebol et al. (2012). They claim that the vigorous mantle flow erodes the craton, unless the craton has a distinct high velocity mantle lithosphere.

9.7 Slab-related features

In addition to the low-velocity anomaly associated with the Cordillera in the west and southwest, the high-velocity anomaly associated with the craton in the northeast, and the boundary between both, an additional intermittent high-velocity anomaly is present at greater depth (250+ km). The boundaries of higher velocity perturbation features were outlined using a 4% variation from the IASP91 model. In the west and southwest many small high-velocity perturbations are present which are best imaged along profiles A, B, C, D, X, and Y. In this area Tian and Zhao (2012) were able to clearly image the Juan de Fuca plate through P-wave tomography. Along 49° N latitude (the upper boundary of the Juan de Fuca slab) was estimated to reach to depths of 300 km from 124° W to 118° W. Sigloch et al., (2008) also were able to image a high-velocity perturbation located along 49° N reaching depths of 350 km at 120° W. At these depths the slope of the Juan de Fuca slab subduction is 45° (Tian and Zhao, 2012). Mercier er al., (2009) confirm a sharply dipping high-velocity anomaly which they interpreted to be the Juan de Fuca subducting slab.

The proximity of these cross-sections to profile X shows that the Juan de Fuca slab can be identified as the high-velocity perturbation located along profile A (Figure 9.7 bottom) at 0 km laterally, with a depth of 200 km and a dip to the northeast, which is possibly also visible on profile X (Figure 9.8 bottom). At greater depths it is not possible to distinctly locate the Juan de Fuca slab due to its proximity with the larger fast velocity zone labeled "old slab". Due to the distance from the Juan de Fuca subduction and the subduction angle, these other deep high-velocity features are unlikely to be a direct result of the Juan de Fuca slab. Many studies have shown (Martin-Short et al., (2015) and Nedimovic et al., (2009) for example) that the Juan de Fuca plate is not present north of 50°N, from oceanic crustal observations.

These deep high-velocity features are more likely higher than measured given the

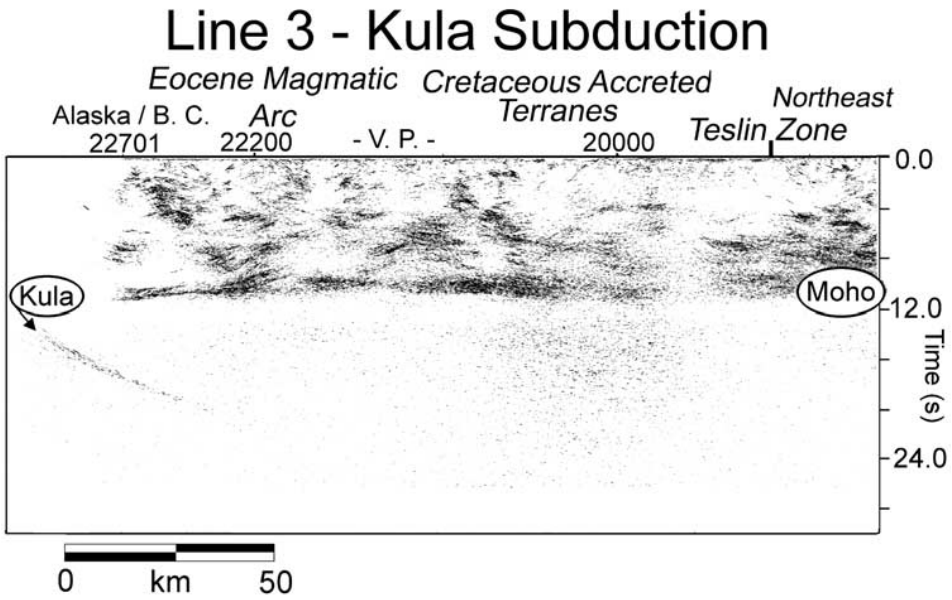

Figure 9.21: Cross-section of Line 3 from Cook et al. (2004) showing the location of the subducted Kula slab. The reflection zone which dips from 45 km eastward to 73 km is interpreted as a relict portion of the Kula plate (Cook et al., 2004).

resolution test results, thereby resulting in velocities found in subduction zones. The location of the Juan de Fuca plate at the western edge of the survey area and primarily south of 50°N makes it unlikely that the Juan de Fuca plate corresponds to the deep high-velocity features observed throughout. Thus, the Kula and Farallon plates are more likely candidates as the origins of these old slabs.

Figure 9.21 shows a cross-section of Line 3 from Cook et al. (2004), which is similarly located to profile C, showing a shallow lithospheric depth of the Kula plate located near 60°N, 135°W. The Kula slab appears to be dipping at an angle of 40°. If this dip is extended down to a depth greater than 300 km, then it is feasible that these old slabs are remnants of the Kula plate as identified in Cook et al. (2004).

Even though there is agreement between profiles A, B, C, X, and Y in relation to the old slab, profiles X and Y show smearing between craton and old slab, which is not seen in profiles A, B, or C. With craton lithosphere depth reaching 200 km

for these profiles it would seem reasonable that deeper cratonic lithosphere would also experience this connection. However, this is not the case. Profiles X and Y however are not able to distinguish the boundaries of the old slab and craton as clearly as the previous profiles. Lateral resolution tests, shown in Figures 9.1 and 9.2, show a trend of smeared high velocity (0.1 km/s) in the recovered model in the area located near this boundary for both periods. For a reference velocity of approximately 4.5 km/s used, a 4% velocity perturbation would result in an increased velocity of 0.18 km/s. A more interesting feature to note is that this smear trends uniformly throughout all periods. Adding to this the result of upward smearing of deep features, due to Feature D, is close in proximity to the high-velocity area. Profiles X and Y are approximately perpendicular to this trend which would result in a near vertical artifact being apparent instead of the southwest dip visible in between Features D and E.

This horizontal and upward smearing may explain the high-velocity area between Features D and E but this area may also be evidence of Cordilleran delamination, a theory proposed by Bao et al. (2014). Delamination occurs when edge-driven convection causes the detachment of the lithosphere from the above crust, and adjacent lithosphere. Figure 9.12 shows the Bao et al. (2014) Vs profile showing a neighbouring high-velocity anomaly connecting the Juan de Fuca slab with the cratonic lithosphere. The connection between the core of the craton and old slab high velocity areas may be the delaminated Cordilleran lithosphere. This feature is only visible along profiles X and Y which are along the profile of Bao et al. (2014). Taking into account the poorer horizontal resolution, the less defined feature is at a similar depth as the Juan de Fuca plate. This matches the observations of Bao et al. (2014). The high-velocity area between the cratonic lithosphere and old slab, of profile X (Figure 9.8 bottom), corresponds well with the interpreted length of the delamination of approximately 450 km and the depth of 200 to 250 km.

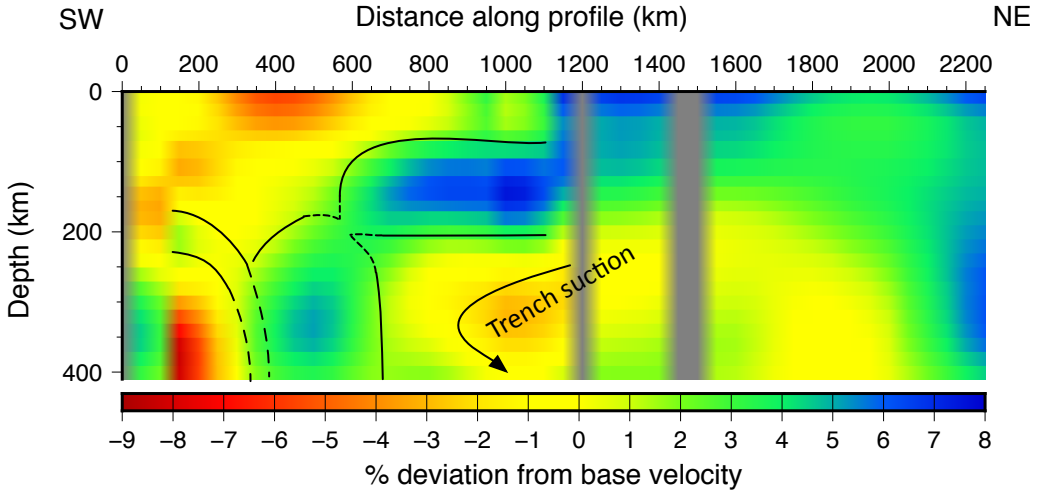

Figure 9.22: Cross-section of profile X showing the pattern of flow expected for trench suction.

Edge-driven convection has been proposed as the engine for Cordilleran delamination (Bao et al., 2014), driving the separation of cratonic lithosphere and Cordilleran lithosphere. Edge-driven convection modeling was applied to the southern Canadian Cordillera by Hardebol et al. (2012) from lateral variations in upper mantle temperature structure. Their results show that the effect of edge-driven convection at the temperature transition, at the base of the lithosphere, is large enough to produce lithosphere deformation. Further more, edge-driven mantle flow at the lateral temperature transition can cause deformation of the overlying lithosphere. Profile X shows a slower feature in the asthenosphere moving around an obstacle in a pattern that is consistent with trench suction (Figure 9.22) and possibly even net deep asthenospheric flow (Yonkee and Weil, 2015).

9.8 Cordilleran slab window

One benefit of profile D is that it offers an along strike view of the Cordillera. In this cross-section, three anomalies associated with old slabs were identified, as explained in section 9.7. Between these old slabs are zones of lower velocity reaching all the way to the 410 km discontinuity (Figure 9.8). These low-velocity perturbation zones are interpreted to represent slab windows of differing age. Slab windows are formed when subducted plates separate, creating a gap. This gap leads to the upflowing of asthenospheric mantle filling the window (Thorkelson and Taylor, 1989).

Thorkelson and Taylor (1989) discuss the the evidence for a Cordilleran slab window existing from the Middle Eocene until the present in the survey area. The difference in motion between the Kula and Farallon plates would allow for plate separation, required for mantle upwelling, while being subducted below the North American plate. In the Middle Eocene, Thorkelson and Taylor (1989) suggest that a slab window appeared under present day British Columbia. Breitsprecher et al. (2003) later confirmed the Kula-Farallon slab window beneath the Pacific Northwest between 50 and 49 Ma. The movement of the Pacific plate would then have pushed the slab window further northward during the Early Miocene.

Slab windows are interpreted along profile D (Figure 9.24) at 900 and 1700 km along the profile due to their lower velocities (-1% and -2%, respectively). The northwestern window (centred at 900 km) does not show a significantly lower-velocity perturbation, compared to the background, which could be due to a thermal equilibrium being reached between mantle upwelling and the surrounding material. The length of time this area was in the slab window, 20 Ma (as calculated from the timeline proposed by Thorkelson and Taylor, 1989), could be enough to reach this near equilibrium.

Moving southeast to 1700 km, a slab window (as indicated by the superimposed

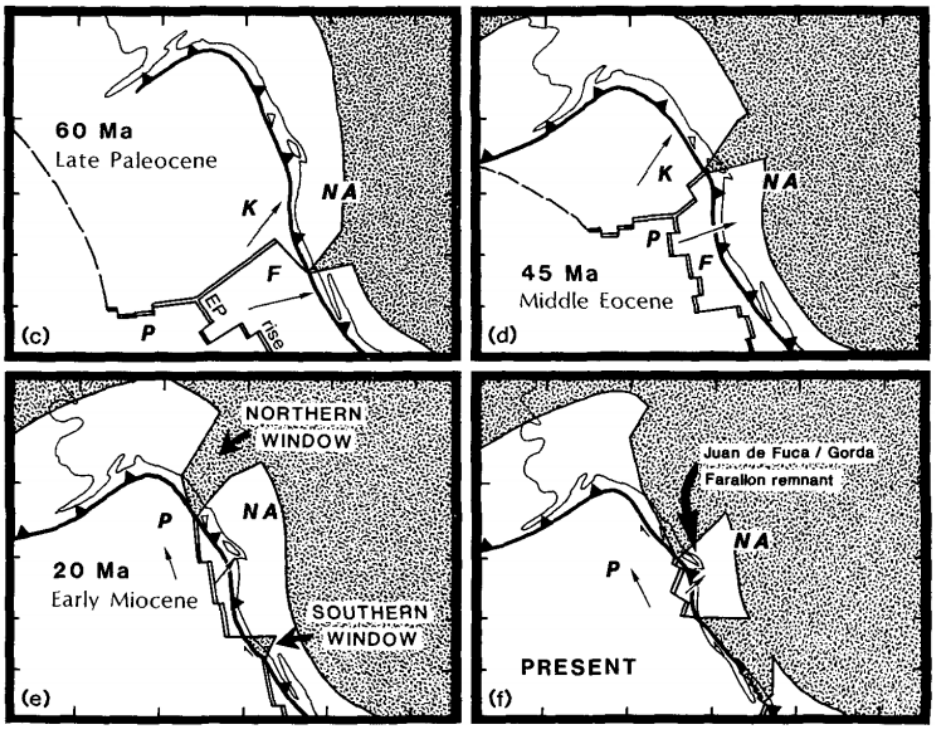

Figure 9.23: Slab windows of the Cordillera created by the difference of plate motion between the Kula and Farallon plates as illustrated in Thorkelson and Taylor (1989). The stippled pattern indicates the asthenosphere beneath the North American plate.

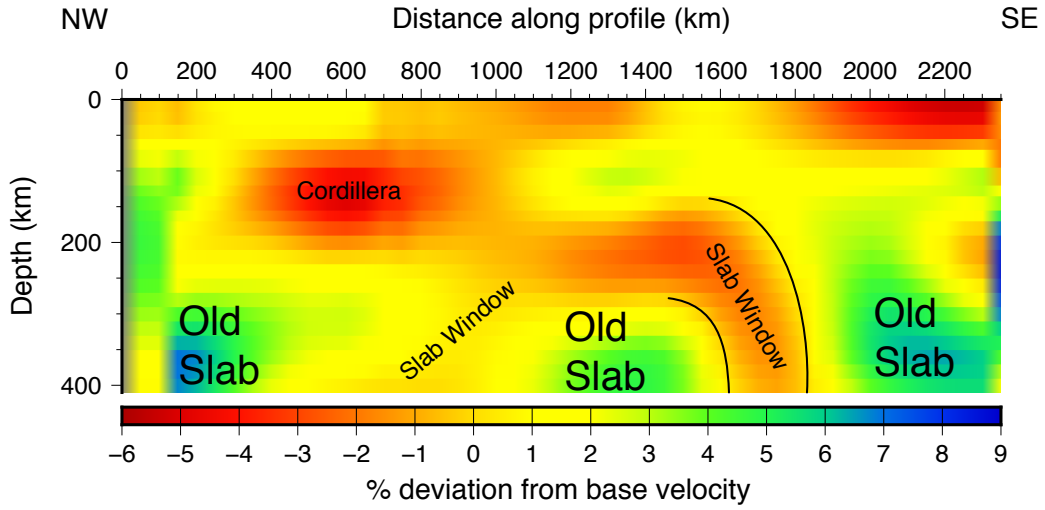

Figure 9.24: Cross-section of profile D showing possible locations of mantle upwelling associated with slab windows in the Cordillera.

lines) suggests upward mantle flow from below 410 km. Due to its proximity to the Juan de Fuca plate, this flow could be caused by plate-edge upwelling driven by the movement of the slab edge through the asthenosphere. Mercier et al. (2009) suggest the same hypothesis of the creation of a slab window in this area causing upwelling from the asthenosphere. The implied horizontal movement of the mantle flow does not appear intuitive as this hot material should continue to rise vertically. A possible explanation for this might be that the old slab centre at 1400 km, along profile D, may have broken off from a larger slab. Tian and Zhao (2012) suggested that a break-off of a slab could result in the slab hole causing magmatism in their study area. The 1400 km old slab may have blocked upper mantle flow as it moved northwestward, while allowing for mantle flow to occur further to the southeast.

9.9 Summary

Horizontal and vertical resolution tests show that the surface wave method is able to recover the starting model fairly well. The horizontal resolution test shows smearing in areas with lower path coverage, as would be expected. For the vertical test, the recovered models primarily underestimate deep high velocity perturbations but are better at recovering shallow velocity perturbations and deep low-velocity perturbations.

The positive velocity perturbation detected to the east of the Cordilleran Deformation Front, represents the cratonic lithosphere. This increased velocity shows that the cratonic lithosphere is generally faster than the averaged IAS91 model velocity. The base of the lithosphere ranges from 175 km to 350 km depth. Within the already faster cratonic lithosphere is a positive velocity perturbation, within the Wopmay Orogen (northwest of the Great Slave Lake), with a greater velocity perturbation. The base of this feature is at 300 km depth. This anomalous perturbation is believed

to be due to a remnant slab left over from a past, frozen, subduction event.

To the east of the Cordilleran Deformation Front is a negative velocity perturbation contrasting with the cratonic lithosphere. This feature corresponds to the Cordilleran lithosphere with its base ranging from 50 km to 200 km depth. The contrasting velocities define the Cordillera/craton boundary, which was imaged to be a feature moderately dipping to the northeast. The transition from Cordillera to craton is not sharp as the boundary is about 200 kilometres wide.

Similar to the higher velocity feature within the Wopmay, 'old slab' features are present throughout most of the survey area. These features are primarily below 300 km depth and interpreted to be evidence of remnant slab fragments, possibly from the subducted Kula or Farallon plates. Only seen along profile D, evidence of a lower velocity aesthenospheric upwelling is present adjacent to old slabs and reaching depths of 200 km. The magnitude of perturbation of these slab windows suggests that the northwestern window is older than the southeastern slab window.

The illustration in Figure 9.25 shows the extent of many of the main features of the Cordillera and craton interpreted from my results. Figure 9.25 (bottom) shows the deeper interpreted slab and slab window related features. The multiple observations of slabs line up fairly well under the Cordillera.

Optimally, an east-west profile located close to the starting points of profiles X and Y, along the Canada/United States border could aid interpretation of the Cordillera/craton interpretation. Such a profile was not possible due to the coverage area provided by the seismic stations in Canada. Use of seismic networks in the United States (specifically Earthscope Transportable Array) would help to expand this interpretation southward.

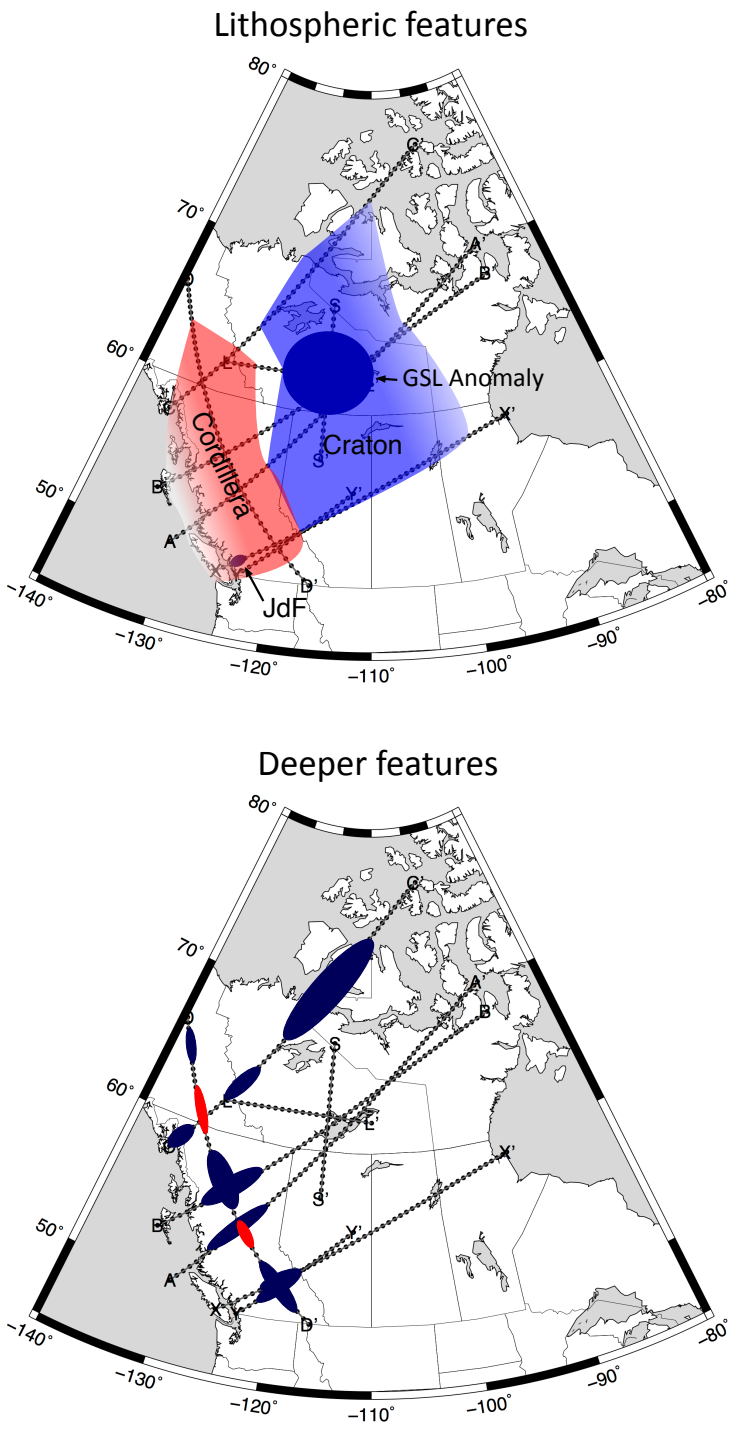

Figure 9.25: Location of cross-sectional profiles overlain with fast (blue) and slow (red) velocity features: (top) general Cordillera (red) and craton (blue) features with the Great Slave Lake anomaly shown as the circular feature within the craton. (bottom) interpreted slabs (dark blue) and slab windows (red).

Chapter 10

Conclusions

The main objective of this project was to image the Cordillera/craton boundary. Rayleigh-wave data from 106 seismic station-pair paths were analyzed throughout western, northern, and central Canada. The stations used were from the CNSN and POLARIS seismic networks. From the data collected, 106 dispersion curves were measured showing the relationship between period and fundamental-mode Rayleigh phase velocity for each station pair path. Inversion of these dispersion curves was done using a 2-D tomographic approach to create velocity maps from which pseudosections and eventually cross-sections were generated through 1-D inversion.

The maps and cross-sections show a low-velocity perturbation located in the Cordilleran lithosphere with values ranging from -2% to -5%, relative to the IASP91 reference model (Kennett and Engdahl, 1991), with a base up to 250 km in depth. A high-velocity perturbation was located under the craton (i.e. east of the Cordilleran deformation front) and interpreted as the cratonic lithosphere with values ranging from 3% to 9%, with the base of the cratonic lithosphere ranging from 175 to 350 km. A high-velocity anomaly was measured under Great Slave Lake and was calculated to be 9% faster than the surrounding area at its maximum. This anomaly, of unusually high velocity, is interpreted as preserved slab material within the cratonic lithosphere.

This boundary between the low-velocity Cordillera and the high-velocity cratonic lithosphere was determined by the 0% perturbation between the two features and was imaged successfully, showing that the lithospheric boundary approximately matches the Cordilleran Deformation Front. The match to the deformation front is best at 200 km depth; the boundary dips to the northeast, with the cratonic lithosphere appearing to be underthrust by Cordilleran material.

Below the low-velocity anomaly of the Cordillera, many cross-sections show small areas of high-velocity perturbation, ranging anywhere from 6-9% faster than the background at depths of 300+ km. I interpret these features as possible remnant fragments of the Kula and Farallon subduction. Along profile D, which runs the length of the Cordillera, evidence of unusually low velocities within the already low-velocity lithosphere was imaged that matches the description of slab window formation suggested by Thorkelson and Taylor (1989). This feature may represent a mantle upwelling from below the 410 km discontinuity in the central Cordillera. Evidence of possible past slab windows is also present along this same profile.

Recommendations

1. Extend the survey area by using stations within the United States' Earthscope Transportable Array.
2. Include more station paths in central Canada to increase the quality of resolution of the craton east of the Cordillera/craton boundary. If not enough events are present for these station-pair paths, if would necessary to install more seismic stations to increase the resolution throughout this region.
3. Using these results, those obtained by Alexey Bryksin, and those published by Darbyshire et al. (2007), a Canada-wide surface-wave tomographic model can be created.

4. Further detailed interpretation of the northwest portion of the survey area.

References

Artemieva, I. M. (2009): The continental lithosphere: Reconciling thermal, seismic, and petrologic data; *Lithos*, vol. 109, pages 23-46.

Ashton, K. E., Hartlub, R. P., Heaman, L. M., Morelli, R. M., Card, C. D., Bethune, K., and Hunter, R. C., (2009): Post-Taltson sedimentary and intrusive history of the southern Rae Province along the northern margin of the Athabasca Basin, Western Canadian Shield; *Precambrian Research*, vol. 175, pages 16-34.

Bao, X. and Eaton, D. W. (2015): Large variations in lithospheric thickness of western Laurentia: Tectonic inheritance or collisional reworking?; *Precambrian Research*, vol. 266, pages 579-586.

Bao, X., Eaton, D. W., and Guest, B. (2014): Plateau uplift in western Canada caused by lithospheric delamination along a craton edge; *Nature Geoscience*, vol. 7, pages 830-833.

Bedle, H. and van der Lee, S. (2009): S velocity variations beneath North America; *Journal of Geophysical Research*, vol. 114, B07308.

Bostock, M. G. (1998): Mantle stratigraphy and evolution of the Slave province; *Journal of Geophysical Research*, vol. 103, pages 21183-21200.

Breitsprecher, K., Thorkelson, D. J., Groome, W. G, and Dostal, J. (2003): Geochemical confirmation of the Kula-Farallon slaw window beneath the Pacific Northwest in Eocene time; *Geology*, vol. 31, No. 4, pages 351-354.

Burianyk, M. J. A., and Kanasewich, E. R. (1997): Upper mantle structure in the

southern Canadian Cordillera; *Geophysical Research Letters*, vol. 24, no. 5, pages 739-742.

Christensen, N. I. and Mooney, W. D. (1995): Seismic velocity structure and composition of the continental crust: A global view; *Journal of Geophysical Research: Solid Earth*, vol. 100, pages 9761-9788.

Clowes, R. M., Hammer, P. T. C., Fernandez-Viejo, G., and Welford, J. K. (2005): Lithospheric structure in northwestern Canada from Lithoprobe seismic refraction and related studies: a synthesis; *Cananadian Journal of Earth Sciences*, vol. 42, pages 1277-1293.

Colpron, M., Logan, J. M., and Mortensen, J. K. (2002): U-Pb zircon age constraint for late Neoproterozoic rifting and initiation of the lower Paleozoic passive margin of western Laurentia; *Cananadian Journal of Earth Sciences*, vol. 39, pages 133-143.

Colpron, M., Nelson, J. L., and Murphy, D. C. (2007): Northern Cordilleran terranes and their interactions through time; *GSA Today*, vol. 17, no. 4/5, pages 4-10.

Conway, K. W., and Johannessen, D. (2007): In Ecosystem overview: Pacific north coast integrated management area (PNCIMA); Edited by Lucas, B. G., Verrin, S., and Brown, R., *Canadian Technical Report of Fishieries and Aquatic Sciences* 2667, pp. 54.

Cook, F. A., van der Velden, A. J., Hall, K. W., and Roberts, B. J. (1998): Tectonic delamination and subcrustal imbrication of the Precambrian lithosphere in northwestern Canada mapped by LITHOPROBE; *Geology*, vol. 26, No. 9, pages 839-842.

Cook, F. A., van der Velden, A. J., Hall, K. W., and Roberts, B. J. (1999): Frozen subduction in Canada's Northwest Territories: Lithoprobe deep lithospheric reflection profiling of the western Canadian Shield; *Tectonics*, vol. 18, no. 1, pages 1-24.

Cook, F. A., Clowes, R. M., Snyder, D. B., van der Velden, A. J., Hall, K. W., Erdmer, P., and Evenchick, C. A. (2004): Precambrian crust beneath the Mesozoic northern Canadian Cordillera discovered by Lithoprobe seismic reflection profiling; *Tectonics*, vol. 23, TC2010.

Cook, F. A., Erdmer, P., and van der Velden, A. J. (2012): The evolving Cordilleran lithosphere; in Tectonics Styles in Canada; the LITHOPROBE Perspective, J. A. Percival, F. A. Cook, and R. M. Clowes, Editors, *Geological Association of Canada, Special Paper* 49, pages 1-39.

Currie, C. A. and Hyndman, R. D. (2006): The thermal structure of subduction zone backarcs; *Journal of Geophysical Research*, vol. 111, B08404, pp. 22.

Darbyshire, F. A., Larsen, T. B., Mosegaard, K., Dahl-Jensen, T., Gudmundsson, O., Bach, T., Gregersen, S., Pedersen, H. A., and Hanka, W. (2004): A first detailed look at the Greenland lithosphere and upper mantle using Rayleigh wave tomography; *Geophysical Journal International*, vol. 158, pages 267-286.

Darbyshire, F. A., Eaton, D. W., Frederiksen, A. W., and Ertolahti, L. (2007): New insights into the lithosphere beneath the Superior Province from Rayleigh wave dispersion and receiver function analysis; *Geophysical Journal International*, vol. 169, pages 1043-1068.

Dover, J. (1994): Geology of part of east-central Alaska; in Plafker, G., and Berg, H. C., eds., The Geology of Alaska: Boulder, Colorado, Geological Society of America, *The Geology of North America*, vol. G-1, pages 153-204.

Fernandez-Viejo, G., and Clowes, R.M. (2003): Lithospheric structure beneath the Archaean Slave Province and Proterozoic Wopmay Orogen, northwestern Canada, from a Lithoprobe refraction wide/angle reflection survey; *Geophysical Journal International*, vol. 153, pages 119.

Frederiksen, A. W., Bostock, M. G., VanDecar, J. C., and Cassidy, J. F. (1998): Seismic structure of the upper mantle beneath the northern Canadian Cordillera

from teleseismic travel-time inversion; *Tectonophysics*, vol. 294, pages 43-55.

Frederiksen, A. W., Bollmann, T., Darbyshire, F., and van der Lee, S. (2013): Modification of continental lithosphere by tectonic processes: A tomographic image of central North America; *Journal of Geophysical Research*, vol. 18, pages 1-16.

Gabrielse, H. (1985): Major dextral transcurrent displacements along the Northern Rocky Mountain Trench and related lineaments in north-central British Columbia; *Geological Society of America Bulletin*, vol. 96, pages 1-14.

Gabrielse, H. and Yorath, C. J. (1991): Tectonic synthesis, Chapter 18 in Geology of the Cordilleran Orogen in Canada, Gabrielse, H. and Yorath, C. J. eds., Geological Survey of Canada, Geology of Canada, no. 4, pages 677-705.

Gabrielse, H., Murphy, D. C., and Mortensen, J. K. (2006): Cretaceous and Cenozoic dextral orogen-parallel displacements, magmatism and paleogeography, north-central Canadian Cordillera; in Paleogeography of the North American Cordillera: Evidence for and Against Large-Scale Displacements, Haggart, J. W., Monger, J. W. H., and Enkin, R. J.,Editors, Geological Association of Canada, Special Papers 46, pages 255-276.

Gomberg, J. S., Priestley, K. F., Masters, T. G., and Brune, J. N. (1988): The structure of the crust and upper mantle of northern Mexico; *Geophysical Journal International*, vol. 94, pages 1-20.

Griffin, W. L., O'Reilly, S. Y., Abe, N., Aulback, S., Davies, R. M., Pearson, N. J., Doyle, B. J., and Kivi, K., (2003): The origin and evolution of Archean lithospheric mantle; *Precambrian Research*, vol. 127, pages 19-41.

Hammer, P. T. C. and Clowes, R. M. (2004):Accreted terranes of northewestern British Columbia, Canada: Lithospheric velocity structure and tectonics; *Journal of Geophysical Research*, vol. 109, B06305.

Hammer, P. T. C., Clowes, R. M., Cook, F. A., ven der Velden, A. J., and Vasudevan,

K. (2010): The Lithoprobe trans-continental lithospheric cross sections: imaging the internal structure of the North American continent; *Canadian Journal of Earth Sciences*, vol. 47, pages 821-857.

Hardebol, N. J., Pysklywec, R. N., and Stephenson, R. (2012): Small-scale convection at a continental back-arc to craton transition: Application to the southern Canadian Cordillera; *Journal of Geophysical Research*, vol. 117, B01408, pp. 18.

Hardebol, N. J., Beekman, F., and Cloetingh, S. A. P. L. (2013): Strong lateral strength contrasts in the mantle lithosphere of continents: A case study from the hot SW Canadian Cordillera; *Tectonophysics*, vol. 602, pages 87-105.

Hayward, N. (2015): Geophysical investigation and reconstruction of lithospheric structure and its control on geology, structure, and mineralization in the Cordillera of northern Canada and eastern Alaska; *Tectonics*, vol. 34, pages 2165-2189.

Herrmann, R. B. (2013) Computer programs in seismology: An evolving tool for instruction and research, *Seismological Research Letters*, vol. 84, pages 1081-1088.

Hoffman, P. S. (1988): United plates of America, the birth of a craton: Early Proterozoic assembly and growth of Laurentia; *Annual Review of Earth and Planetary Sciences*, vol. 16, pages. 543-603.

Hyndman, R. D. (1972): Plate motions relative to the deep mantle and the development of subduction zones; *Nature*, vol. 238, pages 263-265.

Hyndman, R. D., Currie, C. A., Mazzotti, S., and Frederiksen, A. (2009): Temperature control of continental lithosphere elastic thickness, Te vs Vs; *Earth and Planetary Science Letters*, vol. 277, no. 3-4, pages 539-548.

Johnston, S. T. and Gutierrez-Alonso, G. (2010): The North American Cordillera and West European Variscides: Contrasting interpretations of similar mountain systems; *Gondwana Research*, vol. 17, pages 516-525.

Jones, A.G., Ferguson, I.J., Grant, N., Roberts, B. and Farquharson, C. (1997): Results from 1996 MT studies along SNORCLE profiles 1 and 1A; Proceedings

of LITHOPROBE SNORCLE Transect Workshop, Calgary, March 1997, LITHOPROBE Report, 56, pages 42-47.

Jones, A. G., Ferguson, I. J., Chave, A. D., Evans, R. L., and McNeice, G. W. (2001): Electric lithosphere of the Slave craton; *Geology*, vol. 29, no. 5, pages 423-426.

Jones, A. G., Lezaeta, P., Ferguson, I. J., Chave, A. D., Evans, R. L., Garcia, X., and Spratt, J. (2003): The electrical structure of the Slave craton; *Lithos*, vol. 71, pages 505-527.

Jones, A. G., Ledo, J., Ferguson, I. J., Farquharson, C., Garcia, X., Grant, N., McNeice G., Roberts, B., Spratt, J., Wennberg, G., Wolynec, L., and Wu, X. (2005): The electrical resistivity structure of Archean to Tertiary lithosphere along 3200 km of SNORCLE profiles, northwestern Canada; *Canadian Journal of Earth Sciences*, vol. 42, pages 1257-1275.

Jordan, T. H. (1978): Composition and development of the continental tectosphere; *Nature*, Vol. 274, pages 544-548.

Jordan, T. H. (1988): Structure and formation of the continental tectosphere; *Journal of Petrology*, Special Lithosphere Issue, pages 11-37.

Kennett, B. L. N. and Engdahl, E. R. (1991): Traveltimes for global earthquake location and phase indentification; *Geophysical Journal International*, vol. 105, pages 429-465.

Ledo, J., Jones, A. G., and Ferguson, I. J. (2002): Electromagnetic images of a strike-slip fault: The Tintina fault - Northern Canadian; *Geophysical Research Letters*, vol. 29, no. 8, 1225.

MacKenzie, J. M. and Canil, D. (1999): Composition and thermal evolution of cratonic mantle beneath the central Archean Slave Province, NWT, Canada; *Contributions to Mineralogy Petrology*, vol. 134, pages 313-324.

McMechan, M. E. (2000): Walker Creek fault zone, central Rocky Mountains, British Columbia-southern continuation of the Norther Rocky Mountain Trench fault

zone; *Canadian Journal of Earth Sciences*, vol. 37, pages 1259-1273.

Martin-Short, R., Allen, R. M., Bastow, I. D., Totten, E., and Richards, M. A. (2015): Mantle flow geometry from ridge to trench beneath the Gorda-Juan de Fuca plate system; *Nature Geoscience*, vol. 8, pages 965-969.

Meier, T., Dietrich, K., Stockhert, B., and Harjes, H.-P. (2004): One-dimensional models of shear wave velocity for the eastern Mediterranean obtained from the inversion of Rayleigh wave phase velocities and tectonic implications; *Geophysical Journal International*, vol. 156, pages 45-58.

Mercier, J. P., Bostock, M. G., Cassidy, J. F. Dueker, K., Gaherty, J. B. Garnero, E. J., Revenaugh, J., and Zandt, G. (2009): Body-wave tomography of western Canada, *Tectonophysics*, vol. 475, iss. 3-4, pages 480-492.

Miller, M. S. and Eaton, D. W. (2010): Formation of cratonic mantle keels by arc accretion: Evidence from S receiver functions; *Geophysical Research Letters*, vol. 37, L18305.

Monger, J. W. H., Price, R. A. and Tempelman-Kluit, D. J. (1982): Tectonic accretion and the origin of the two major metamorphic and tectonic welts in the Canadian Cordillera; *Geology*, vol. 10, pages 70-75.

Monger, J. W. H. (1989): Overview of Cordilleran geology. In Western Canada Sedimentary Basin: A Case History; Ed. Ricketts, B. D., Canadian Society of Petroleum Geologists.

Nedimovic, M. R., Bohnenstiehl, D. R., Carbotte, S. M., Canales, J. P., and Dziak, R. P. (2009): Faulting and hydration of the Juan de Fuca plate system; *Earth and Planetary Science Letters*, 284, pages 94-102.

Nelson, J. and Colpron, M. (2007): Tectonics and metallogeny of the British Columbia, Yukon and Alaskan Cordillera, 1.8 Ga to the present; in Goodfellow, W. D., ed., Mineral Deposits of Canada: A Synthesis of Major Deposit-Types, District Metallogeny, the Evolution of Geological Provinces, and Exploration Methods:

Geological Association of Canada, Mineral Deposits Division, Special Publication No. 5, pages 755-791.

Nolet, G. (1990): Partitioned waveform inversion and two-dimensional structure under the network of autonomously recording seismographs; *Journal of Geophysical Research*, vol. 95, no. B6, pages 8499-8512.

Powell, C. McA., Li, Z. X., McElhinny, M. W., Meert, J G., and Park, J. K. (1993): Palemagnetic constraints on timing of the Neoproterozoic breakup of Rodinia and the Cambrian formation of Gondwana; *Geology*, vol. 21, no. 10, pages 889-892.

Rippe, D., Unsworth, M. J., and Currie, C. A. (2013): Magnetotelluric constraints on the fluid content in the upper mantle beneath the southern Canadian Cordillera: Implications for rheology; *Journal of Geophysical Research: Solid Earth*, vol. 118(10), pages 5601-5624.

Roddick, J. A. (1967): Tintina trench; *The Journal of Geology*, pages 23-33.

Ross, G. M. (1991): Tectonic setting of the Windermere Supergroup revisited; *Geology*, vol. 19, no. 11, pages 1125-1128.

Saltus, R. W. (2007): Matching magnetic trends and Patterns across the Tintina fault, Alaska and Canada - evidence for offset of about 490 kilometers; in Recent U.S. Geological Survey studies in the Tintina gold province, Alaska, United States, and Yukon, Canada - results of a 5-year project, Gough, L. P. and Day, W. C., Editors, U.S. Geological Survey Scientific Investigations Report 2007-5289-C, pages C1-C7.

Saruwatari, K., Ji, S., Long, C., and Salisbury, M. H. (2001): Seismic anisotropy of mantle xenoliths and constraints on upper mantle structure beneath the southern Canadian Cordillera; *Tectonophysics*, vol. 339, pages 403-426.

Saunders, P., Priestley, K., and Taymaz, T. (1998): Variations in the crustal structure beneath western Turkey; *Geophysical Journal International*, vol. 134, pages 373-389.

Schaeffer, A. J. and Lebedev, S. (2014): Imaging the North American continent using waveform inversion of global and USArray data; *Earth and Planetary Science Letters*, 402, pages 26-41.

Schmandt, B. and Lin F. -C., (2014): P and S wave tomography of the mantle beneath the United States; *Geophysical Research Letters*, vol. 41, pages 6342-6349.

Sears, J. W. and Price, R. A. (2003): Tightening the Siberian connection to western Laurentia; *GSA Bulletin*, vol. 115, no. 8, pages 943-953.

Sears, J. W. and Price, R. A. (2000): New look at the Siberian connection: No SWEAT; *Geology*, vol. 28, no. 5, pages 423-426.

Shapiro, N. M., Campillo, M., Paul, A., Singh, S. K., Jongmans, D., and Sanchez-Sesma, F. J., (1997): Surface-wave propagation across the Mexican Volcanic Belt and the origin of the long-period seismic-wave amplification in the Valley of Mexico; *Geophysical Journal International*, vol. 128, pages 151-166.

Sigloch, K., McQuarrie, N., and Nolet, G. (2008): Two-stage subduction history under North America inferred from multiple-frequency tomography; *Nature*, vol. 1, pages 458-462.

Soyer, W. and Unsworth, M. J. (2006): Deep electrical structure of the northern Cascadia (British Columbia, Canada) subduction zone: Implications for the distribution of fluids; *Geology*, vol. 34(1), pages 53-56.

Spratt, J. E, Jones, A. G., Jackson, V. A., Collins, L., and Avdeeva, A. (2009): Lithospheric geometry of the Wopmay orogen from a Slave craton to Bear Province magnetotelluric transect; *Journal of Geophysical Research*, vol. 114, B01101, pp. 18.

Stein, S. and Wysession, M. (2003): An introduction to seismology, earthquakes, and earth structure; Blackwell Publishing, Malden, pp. 498.

Tempelman-Kluit, D. J. (1979): Transported cataclasite, ophiolite and gradodiorite in Yukon: Evidence of arc-continent collision; Geological Survey of Canada, paper

79-14, p. 27.

Thorkelson, D. J. and Taylor, R. P. (1989): Cordilleran slab windows; *Geology*, vol, 17, pages 833-836.

Tian, Y. and Zhao, D. (2012): P-wave tomography of the western United States: Insight into the Yellowstone hotspot and the Juan de Fuca slab; *Physics of the Earth and Planetary Interiors*, vol. 200-201, pages 72-84.

Van der Lee, S. and Frederiksen, A. (2005): Surface wave tomography applied to the North American upper mantle; *Geophysical Monograph Series* vol. 157, pages 67-80.

Wessel, P., Smith, W. H. F., Scharroo, R., Luis, J., and Wobbe, F. (2013): Generic Mapping Tools: Improved Version Released, *Eos*, vol. 94, pages 409-410.

Whitmeyer, S. J. and Karlstrom, K. E. (2007): Tectonic model for the Proterozoic growth of North America; *Geosphere*, vol. 3, no. 4, pages 220-259.

Wingate, M. T. D. and Giddings, J. W. (2000): Age and paleomagnetism of the Mundine Well dyke swarm, Western Australia: implications fro an Australia-Laurentia connection at 755 Ma; *Precambrian Research*, vol. 100, pages 335-357.

Yonkee, W. A. and Weil, A. B. (2015): Tectonic evolution of the Sevier and Laramide belts with in the North American Cordillera orogenic system; *Earth-Science Reviews*, vol. 150, pages 531-593.

Zaporozan, T, Bryksin, A, Frederiksen, A. W., and Darbyshire, F. A. (2014): A tomographic model of the Canadian lithosphere via two-station surface-wave analysis; AGU Fall Meeting abstract #T23B-4650.

Appendix

Station pairs and number of events

Table 10.1: List of station pairs and the number of events.

First Station	Second Station	Number of Events
BBB	MBC	3
BMBC	BBB	41
BMBC	DLBC	165
BMBC	EDM	284
BMBC	FNBB	25
BMBC	PNT	19
BMBC	RES	7
BMBC	WALA	13
BVCY	RES	6
DAWY	GBLN	2
DAWY	GDLN	8
DAWY	INK	6
DAWY	JERN	20
DAWY	RES	55

Continued on next page

Table 10.1 – continued from previous page

First Station	Second Station	Number of Events
DIB	BBB	27
DIB	BMBC	17
DIB	DAWY	14
DIB	DLBC	4
DIB	EDB	47
DIB	EDM	15
DIB	FCC	23
DIB	FSMA	5
DIB	INK	3
DIB	MEDA	5
DIB	PLBC	9
DIB	PNT	93
DIB	RES	12
DIB	ULM	17
DIB	VGZ	39
DIB	WALA	53
DIB	WHY	6
DLBC	DAWY	29
DLBC	FNBB	116
DLBC	PLBC	40
DLBC	RUBB	5
DLBC	WHY	55
EDM	MBC	13

Continued on next page

Table 10.1 – continued from previous page

First Station	Second Station	Number of Events
FCC	MBC	8
FNBB	FSMA	3
FSMA	BVCY	5
FSMA	DAWY	15
FSMA	INK	4
HILA	DHRN	6
ILKN	RES	4
INK	AP3N	7
INK	ARVN	15
INK	ATKO	31
INK	BBB	19
INK	BMBC	14
INK	EDM	37
INK	GIFN	17
INK	HILA	9
INK	KUGN	6
INK	LAIN	6
INK	MBC	3
INK	MEDA	2
INK	RES	35
INK	RUBB	9
INK	SMPN	7
INK	STLN	16

Continued on next page

Table 10.1 – continued from previous page

First Station	Second Station	Number of Events
INK	ULM	46
INK	WAGN	6
INK	WHY	7
INK	YBKN	6
INK	YRTN	8
KUKN	EDM	3
MBC	PNT	5
MBC	RES	8
MBC	ULM	8
PHC	MBMC	10
PHC	DAWY	23
PHC	DHRN	2
PHC	DLBC	30
PHC	FNBB	7
PHC	FNBC	2
PHC	RES	16
PLBC	DHRN	8
PLBC	FNBB	31
PLBC	FSMA	3
PLBC	MEDA	4
PNT	DAWY	37
PNT	EDM	47
PNT	INK	32

Continued on next page

Table 10.1 – continued from previous page

First Station	Second Station	Number of Events
PNT	MEDA	5
PNT	PLBC	18
PNT	RES	15
PNT	RUBB	78
PNT	VGZ	13
PNT	WALA	50
PNT	WAPA	2
RES	KUKN	2
ROMN	RES	3
RUBB	DAWY	11
SMPN	DHRN	28
VGZ	ATKO	14
VGZ	BMBC	4
VGZ	EPLO	14
VGZ	FCC	20
VGZ	INK	7
VGZ	PKLO	9
VGZ	RES	3
VGZ	WALA	30
WALA	WAPA	10
WAPA	EDM	29
WHY	MBC	5

Dispersion curves

Dispersion curves for all station pair paths are viewable in the supplemental file all_curves.pdf.

Standard error for each profile

Table 10.2: Standard error of inversions at each location.

Distance	**Profile X**	**Profile Y**	**Profile A**	**Profile B**	**Profile C**
	(km/s)				
0	0.2211	0.4376	0.5785	0.2863	0.2143
50	0.5443	0.5474	0.2355	0.1524	0.1893
100	0.5458	0.2883	0.1816	0.1618	0.1877
150	0.5565	0.2275	0.1316	0.1798	0.1855
200	0.5563	0.2026	0.1025	0.1967	0.1907
250	0.344	0.1767	0.1251	0.2177	0.1965
300	0.3287	0.1497	0.1221	0.2455	0.2025
350	0.3086	0.1286	0.1328	0.2762	0.2123
400	0.2882	0.1242	0.1567	0.304	0.2287
450	0.593	0.645	0.1939	0.3224	0.249
500	0.2701	0.1575	0.2387	0.3326	0.2758
550	0.2649	0.2166	0.466	0.2132	0.1773
600	0.2623	0.2776	0.281	0.3274	0.2318
650	0.2576	0.3347	0.3149	0.3	0.2428
700	0.2435	0.3837	0.3337	0.2657	0.2491

Continued on next page

Table 10.2 – continued from previous page

Distance	Profile X	Profile Y	Profile A	Profile B	Profile C
750	0.2257	0.4283	0.3314	0.2391	0.3695
800	0.207	0.4733	0.3091	0.2181	0.4259
850	0.1897	0.5158	0.2994	0.1708	0.4878
900	0.1833	0.5357	0.2473	0.1563	0.4334
950	0.4262	0.5286	0.2237	0.1137	0.4204
1000	0.1835		0.2068	0.1483	0.4265
1050	0.1905		0.157	0.1081	0.4067
1100	0.21		0.3357	0.0991	0.1398
1150	0.2443		0.1	0.0897	0.3724
1200	0.2893		0.0974	0.1082	0.1812
1250	0.3166		0.0959	0.0852	0.161
1300	0.2789		0.1665	0.0909	0.1521
1350	0.1913		0.1412	0.1148	0.1662
1400	0.1677		0.1158	0.1506	0.1206
1450			0.0984	0.1734	0.135
1500			0.0955	0.1978	0.1554
1550	0.1571		0.2294	0.1153	0.1702
1600	0.1401		0.1076	0.266	0.1747
1650	0.2531		0.1221	0.3181	0.2314
1700	0.1201		0.1327	0.3741	0.1705
1750	0.1057		0.1501	0.4307	0.1701
1800	0.1208		0.1659	0.4436	0.1698
1850	0.1741		0.1954		0.1732

Continued on next page

Table 10.2 – continued from previous page

Distance	Profile X	Profile Y	Profile A	Profile B	Profile C
1900	0.2384		0.1664		0.1813
1950	0.2983		0.1617	0.1279	0.1885
2000	0.3554			0.1722	0.1927
2050	0.4078			0.2183	
2100	0.4573		0.1841	0.254	
2150	0.5087		0.2088	0.3538	
2200			0.6481	0.2778	0.1921
2250			0.2293	0.2825	0.1916
2300			0.2454	0.2835	0.1913
2350			0.2631	0.2677	
2400			0.2873	0.2441	
2450			0.3119	0.2194	
2500			0.3271	0.198	
2550			0.332	0.1855	
2600			0.3243	0.1711	
2650			0.3067	0.157	
2700			0.2786		

Table 10.3: Standard error of inversions at each location.

Distance	**Profile L**	**Profile D**	**Profile S**
	(km/s)		
0	0.1771	0.2275	0.1892
50	0.2352	0.1193	0.1304
100	0.2266	0.1348	0.1583
150	0.2074	0.1648	0.1878
200	0.2239	0.2069	0.2043
250	0.2326	0.254	0.2174
300	0.2478	0.2939	0.2286
350	0.2598	0.3188	0.2435
400	0.2677	0.3226	0.2638
450	0.2685	0.3087	0.2898
500	0.1917	0.2895	0.3163
550	0.2724	0.3401	0.1752
600	0.2801	0.2642	0.3317
650	0.2934	0.2271	0.3309
700	0.311	0.1868	0.3152
750	0.3249	0.1532	0.2817
800	0.3362	0.1277	0.2356
850	0.3305	0.1078	0.1873
900	0.327	0.0866	0.1385
950	0.2855	0.0781	0.1076
1000	0.242	0.0887	0.0964
Continued on next page			

Table 10.3 – continued from previous page

Distance	Profile L	Profile D	Profile S
1050		0.1091	0.1095
1100		0.2914	
1150		0.1298	
1200		0.1421	
1250		0.1522	
1300		0.1701	
1350		0.2145	
1400		0.2827	
1450		0.3375	
1500		0.1119	
1550		0.2495	
1600		0.2068	
1650		0.1725	
1700		0.15	
1750		0.1378	
1800		0.2439	
1850		0.1382	
1900		0.1536	
1950		0.173	
2000		0.1848	
2050		0.1948	
2100		0.1979	
2150		0.1728	

Continued on next page

Table 10.3 – continued from previous page

Distance	Profile L	Profile D	Profile S
2200		0.149	
2250		0.1321	
2300		0.1207	
2350			
2400			
2450			
2500			
2550			
2600			
2650			
2700			